Declaration

I hereby declare that the work reported in this thesis is entirely original. This thesis has been composed by me at Raman Research Institute under the supervision of Dr. S. A. Rangwala. I further declare that, to my best knowledge, the matter presented in this thesis has not formed the basis for the award of any degree, diploma, membership, associateship, fellowship or any other similar title of any university or institution.

Seunghyun Lee

Countersigned:

Dr. S. A. Rangwala

Light and Matter Physics Group

Raman Research Institute

Bangalore-560 080

Certification

This is to certify that the thesis titled **"Study of trapped ion collisions with cold atoms and cold molecules"** submitted by Seunghyun Lee for the award of the degree of Doctor of Philosophy of Jawaharlal Nehru University is a bona-fide work. This has not been submitted to any other university for any other degree, diploma or title.

<div align="right">

Dr. S. A. Rangwala

(Thesis Supervisor)

Light and Matter Physics Group

Raman Research Institute

Bangalore-560 080

</div>

Prof. Ravi Subrahmanyan

Director

Raman Research Institute

Bangalore-560 080

Acknowledgments

I wish to thank Dr. Sadiq Rangwala for giving me the opportunity to work in an exciting research field, and also for his guidance and constant supervision of my thesis work. It would not have been completed without his support and contribution towards this work.

I would like to extend my sincere thanks to Prof. G. Werth, Institut für Phyzik, Mainz, Germany for the active collaboration with our group. It was always a pleasure to have him around, sharing his expertise on ion trap physics and interesting stories in his life.

I wish to thank Dr. Andal Narayanan and Dr. Pramod Pullarkat for the annual review and assessment of my thesis work.

My thank the director and the administrative department of Raman Research Institute (RRI) for facilitating the scientific environment. Special thanks to Krishna and Marisa for helping me in my VISA and annual registration work.

I gratefully acknowledge the technical support of all members of the general and precision workshops for all my work orders.

My sincere thank to Mrs. Sujatha from the Radio Astronomy Laboratory for her support in handling many of the electronic components used in the experiments. She has been extremely patient in unceasing debugging and testing the home-built electronic instruments.

I sincerely thank Ravi for sharing experimental skills and knowledge, and also for useful discussions.

Having Tridib and Jyothi around was a great experience academically as well as personally. Special thanks to Jyothi for her significant role in the photoassociation calculations and related discussions which undoubtedly helped us in understanding results from the experiments.

I enjoy the presence of all the past and present members of the students' room in the Light and Matter Physics (LAMP) group. I also wish to show my gratitude to Savitha, Harini, Shiva and Manju for their help and cooperation in the group.

I thank the entire staff of RRI who contributed in one way or the other in the accomplishment of the present work.

My stay in India now meets its end. I cherish each and every moment and would never forget.

Finally, I am indebted to my mom and dad for their tremendous support and appreciation towards my thesis work.

Synopsis

Trapping and cooling of ions is a very well-established area in physics ever since various ion traps were invented. These have been used to explore diverse areas such as elastic and inelastic collision processes, few-body problems, precision measurements, mass spectroscopy and quantum information and processing. Independently, the trapping and cooling of neutral atoms are extensively developed to create trapped ensembles of atoms at the low temperatures of ≈ 100 μK, ideal for spectroscopic studies and at the lower temperatures, interactions between constituent species in an ensemble. These ultracold atoms are used as a tool to study quantum collisions such as photoassociation, Bose-Einstein condensates and ultracold Fermi gases, and also can be used in quantum information. In recent times, mixtures of trapped ions and atoms in hybrid traps are produced to investigate interactions between them. This emerging area of physics shows a way to study cold chemistry and many body problems.

The main motivation of my research is to experimentally investigate interactions between trapped ions and cold neutrals like atoms and molecules. These interactions include elastic and charge exchange collisions and inelastic collision of trapped ions with photoassociated molecules. The role of trapped ions in the ion-atom-molecule mixed system has been the primary interest in the study. The main challenge has been the *in situ* detection of the optically dark ions without disturbing the system. To overcome this, we have developed a new method to determine the collision rate coefficients for the ion-cold atom mixtures from atomic fluorescence. This study has also led to observe and understand the dissociation of photoassociated molecules in the presence of trapped ion-atom mixtures. In the present work, we systematically address these interesting problems with an emphasis on the intrinsic stability of the ion-atom system and ion-atom-molecule system.

A novel ion trap design

An initial part of my thesis work was purely numerical in nature. We design an ion trap configuration that is three-dimensionally symmetric by its geometry, creating fre-

v

quency degenerate trapping field. The trap consists of three parallel pairs of cylindrical electrodes along the Cartesian axes. This basic trap has an ability to be extended to form a lattice of ion traps (LIT) where an individual lattice site can be operated as an independent ion trap. Each trap can be considered as a symmetric harmonic oscillator in a 3-dimension for a single ion. The basic trap and a LIT are numerically characterized for different locations in the lattice and compared, illustrating the robustness of the LIT concept. Practical implementations and some of possible applications of the LIT are discussed.

Ion trap characterization

The experimental research is carried out on a combined trap for atoms and ions. The combined trap comprises of a magneto-optical trap (MOT) for ^{85}Rb atoms and a modified linear Paul trap for ^{85}Rb$^+$ ions, with spatial overlap that enables the study of interactions between the trapped ions and cold atoms. In MOT, we characterize loading and loss rates of the trap, atom density in the MOT and temperature of the atom cloud. Independently the ion trap is characterized mainly on the measurement of motional resonances of the trapped ions and stability of ions in several operating parameters of the ion trap. As Rb$^+$ ions are inaccessible for optical detection, they are destructively detected. To understand the dynamics of ions in the trapping potential, we develop multi-particle ion simulation using molecular dynamics algorithm. This enables us to estimate the temperature of ions by matching simulated and measured time of flight values. Described below are two problems on this system that form a major part of my thesis.

Trapped Rb$^+$ ions and cold atoms

A neutral atom and an ion interact via a long range attractive potential of the form, $-1/r^4$. For an ion species colliding with its parent atom species, the dominant two-body collision channels are the elastic and resonant charge exchange collisions. Due to the nature of the ion speed distribution in our system, the collision rate coefficient

is the most relevant quantity to measure rather than the collision cross-section. In the traditional trapped ion collision experiments, ion-neutral collision rate coefficients are measured from the loss of ions from the trap. The combined trap enables us to observe both trapped ions and MOT atoms. This becomes advantageous to measure the MOT atom fluorescence for optically dark ions, where the detection *in situ* becomes challenging without disturbing the system. The ion-atom system achieves its steady state when operating simultaneously. This allows us to use rate equation models balancing a loading rate and various loss rates of atoms in the MOT. The optically dark Rb^+ ions are created by photoionization of atoms in the excited state, and accumulated at the center of the ion trap, which overlaps with the MOT. Since ion velocities are large and the MOT capture velocity for the atoms are much smaller, ion-atom collisions cause atoms to eject atoms from the MOT. The consequent drop in MOT fluorescence is utilized to develop the framework for the measurement of the ion-atom collision rate coefficient. We characterize various loss rates due to collision with background atoms, photoionization and ion-atom interaction in the system. Making reasonable approximations, an analytical expression is derived for the rate of atom loss due to ion-atom interactions, and hence the ion-atom collision rate coefficient. Finally we measure the collision coefficient between laser-cooled Rb atoms and optically dark Rb^+ ions as $k_{ia} = 1.23 \times 10^{-13}$ m^3/s, which compares well with the corresponding theoretically estimated value, $k_{ia} = 1.12 \times 10^{-13}$ m^3/s.

Trapped Rb^+ ions, cold atoms and cold Rb_2 molecules

Ion-cold atom collisions studies are further extended to ion-cold molecule studies. When two colliding atoms absorbs a resonant photon between the ground asymptote state and a particle vibration level in the excited state, these atoms photoassociate to create a long range molecule in the excited molecular state. Photoassociation (PA) of Rb atoms creates Rb2 molecules in high vibrational levels in 0_g^-, 0_u^+ and 1_g the excited states (labeled for Hund's case c), giving additional loss to the MOT atoms. We experimentally measure a loss rate of atoms $\tilde{\gamma}_0$ in the MOT due to PA at a PA laser energy,

$\epsilon_p = 12814.59$ cm^{-1} (≈ 60 GHz red-detuned from the dissociation limit). ϵ_p corresponds to $v = 50$ in 0_g^- and $v = 200$ in 1_g. To study ion-cold molecule interaction, we create photoassociated Rb$_2$ molecules at ϵ_p in the presence of trapped Rb$^+$ ions. Under this condition, there is a fractional increase in number of atoms in the presence of trapped ions, compared to the PA case. From this experiment, we measure the loss rate of MOT atoms due to PA in the presence of trapped ions $\tilde{\gamma}_0^I$, and observe that $\tilde{\gamma}_0^I < \tilde{\gamma}_0$. This suggests that trapped ions collisionally induce dissociation of vibrational excited molecules into free atoms and those free atoms are captured back to the MOT. Using experimentally obtained values of $\tilde{\gamma}_0^I$ and $\tilde{\gamma}_0$, dissociation rate coefficient of PA Rb$_2$ molecule due to a trapped ion within MOT recapture energy is measured as $k_{im}^r = 9.17 \times 10^{-15}$ m^3/s. To understand this experimental observation, we consider a molecule as a harmonic oscillator in the presence of an external field due to an ion approaching to the oscillator. The vibrational energy ΔE_{vib} transfer to the oscillator is calculated as a function of ion velocity and separation between an ion and a molecule. When 60 GHz $< \Delta E_{vib} < 252$ GHz (energy corresponding to MOT recapture velocity for two atoms), then the molecule gets dissociated into two free atoms, which are captured back to the MOT. The simulation result supports the dissociation of molecules by the collision with trapped ions. From this calculation, we extract $k_{im}^r = 5.69 \times 10^{-15}$ m^3/s. As the calculation is based on a classical harmonic oscillator, one cannot take this value literally but this surely helps in deeper understanding of the mechanism.

In summary, this work establishes an experimental method to study interactions in a mixed system of trapped ions, cold atoms and cold molecules, using cold atoms as a probe. We use this method to measure trapped ion collision rate coefficients with cold atom and cold molecules. The system has the intrinsic stabilization of ions, atoms and molecules via their interactions. This enables us to employ rate equation models of trapped atoms in the MOT. The interactions result in loss of trapped atoms. From the loss rates of atoms in the MOT, we estimate trapped ion collision rate coefficients with cold atoms and cold molecules. This work sets the platform for studying trapped ion collisions related experiments in cold chemistry and many body physics.

Introduction

1.1   Overview

In recent years, there has been tremendous attention and progress in the experimental studies of low-energy interactions between the constituents of dilute cold and ulta cold gases due to extensive development in laser-cooling and trapping of atoms and ions.

The cooling with trapping reduces the spread in position and momentum phase space. The trapping of ions and atoms employ different experimental techniques, resulting in difference in their energies at the bottom of their respective traps, but similarities in the physics they address. Independently, cold atom physics as well as cold ion physics have enabled tremendous progress in some of the most interesting physics problems of our time, such as precisions spectroscopy, many particle physics, quantum simulation, quantum computation and quantum chemistry. Furthermore, a new emerging line of research has started to study interactions between trapped ions and cold atoms. The trapping ions and cold atoms simultaneously with spatial overlap was originally demonstrated by W. W. Smith *et. al* [1] to investigate ion-atom interactions. At present, there are variations of such combined ion-atom traps in a handful of groups, designed to investigate specific goals and interests. The number of such experiments is growing rapidly as the rich possibilities with these systems are demonstrated.

The mixtures of trapped ions and cold/ultracold atoms enable us to investigate exciting physics ranging from a single trapped ion inside a Bose-Einstein Condensate (BEC) [2, 3] and Magneto-Optical Trap (MOT) atoms superimposed with laser cooled ions [4, 5, 6, 7], to mixtures where the ions are only cooled in collision with the atoms [8, 9, 10]. Elastic and charge exchange processes in these mixed, trapped system have been demonstrated and measured [4, 10, 11]. As an extension, recently work has begun on

trapped ion-dipole systems [12].

1.2 Motivations and strategies

Cold chemistry is an emerging field, traditionally pursued by the chemical physics and astrophysics communities, and now by ultracold atomic and molecular physics communities. Alkali atoms in the first column of the periodic table share similar chemical properties of a hydrogen atom, which is spectroscopically and fundamentally an important species. A mixture of alkali atoms and ionic atoms is an experimentally unique system to study ion-assisted cold chemistry. We have a system of Rb^+ ions + cold Rb atoms + cold Rb_2 molecules in a combined trap which consists of a magneto-optical trap (MOT) for ^{85}Rb atoms and a modified linear Paul trap for $^{85}Rb^+$ ions, with the common spatial overlap. The combined trap enables us to investigate trapped ion collisions/interactions with neutrals.

A Rb atom and a Rb^+ ion interact via a long range attractive potential of the form, $-1/r^4$. These interactions include elastic and resonant charge exchange collisions. In the experiments related to trapped ion collisions, ion signal is measured to understand the interactions. For optically dark ions like Rb^+ ion, *in situ* detection without disturbing the system is challenging. To be more flexible to study various species of charged particles, it is crucial to overcome this. The combined trap has an ability to measure the interactions between ions-cold atoms from the atomic fluorescence from the MOT. Dynamics of trapped atoms in the presence of trapped ions is a key to *in situ* measurement of optically dark ions indirectly. This can also be extended to interactions between ions and cold molecules. Cold molecules can be produced in various ways. We choose to produce them by photoassociation of cold atoms in the MOT. The signature of molecular formation is obtained from trap loss spectra of atomic fluorescence from the MOT. Again, the dynamics of atoms in the MOT changes with the formation of molecules as a loss channel. Therefore, we expect trapped ion collisions with photoassociated molecules can also be comprehended by the dynamics of atoms in the

MOT.

The role of trapped ions in the ion-atom-molecule mixed system has been the primary interest in these studies. The richness of high-resolution spectral signatures in cold atoms and photoassociative molecules permits access to a specific state to study collisions and chemically reactive dynamics by trapped ions, thus offering important insights and intuitions into association and dissociation process. These processes can be related to collisions and the consequences in outer space and atmosphere.

1.3   Goals and results

Present thesis aims to experimentally investigate trapped ion-cold atom interactions. To understand the experimental result, numerical simulations and rate equation model are formulated. This work is extended to study trapped ion-cold molecule interactions. The main objectives in the thesis are as follows:

- To design reliable ion trap simulations for design and interpretation of experiments.

- To use the above simulation in the design of a 3-dimensionally symmetric ion trap by its geometry and characterization of the trap in a simple isolated cubic and extended array structures.

- To develop a molecular dynamics simulation to study dynamics of interacting charged particles.

- To estimate the temperature of ions from the experimental observations using molecular dynamics simulations and Virial theorem.

- To develop a technique to measure a collision rate coefficient of cold atom-ion interaction using atomic fluorescence as a probe.

- To construct an experimental setup for photoassociation of cold Rb atoms using an external cavity diode laser (ECDL) and a tapered amplifier (TA).

- To study and identify the photoassociation spectra of cold Rb atoms near to the dissociation energy.

- To experimentally demonstrate collision-induced dissociation of cold Rb molecules by ions in the combined trap.

- To understand theoretically collision-induced dissociation of molecules by ions.

1.4   Organization of the thesis

The second chapter proposes a design of an ion trap which is 3-dimensionally symmetric by its geometry and has great geometric scalability. The basic trap configuration and extended array of $3 \times 3 \times 3$ basic traps are characterized for different locations in the lattice. Possible applications such as precision spectroscopy, quantum information processing and few-particle interacting system are discussed.

The third chapter describes in detail the experimental arrangement and operation of the combined trap as an instrument to study ion-atom interactions. The vacuum system, the different components of the magneto optical trap and the linear Paul trap, the detection of the ions and atoms and the characterization of each trap are discussed. The additional setup constructed for photoassociation is described.

Molecular dynamics simulations employ a direct particle-particle method for the charged particle dynamics. The motion of N particles in the ion trap potential with coulomb potential is numerically integrated. The fourth chapter describes algorithm and implementation of such molecular dynamics simulations. Finally, we discuss how the simulation is used in estimating the temperature of ions from the experimental observation using Virial theorem.

We measure collision rate coefficient between laser-cooled atoms in the magneto-optical trap and ions in the linear Paul trap. Chapter five gives a new method developed by us, to measure the collision rate coefficient from atomic fluorescence using a simple rate equation model. It becomes advantageous for dark ions when *in situ* detection is challenging without disturbing the system.

In the sixth chapter, photoassociation of cold Rb atoms is demonstrated to form cold Rb molecules. We extend this work to study collision-induced dissociation of cold Rb molecules by Rb^+ ions and explain such phenomena with a classical calculation of vibrational energy transfer in a collision between an ion and a non-rotating diatomic molecule.

The thesis concludes with summary of the results and an outlook on the future directions of research using such ion-atom-molecule system.

A novel ion trap design

Trapping and cooling of charged particles has contributed to important investigations motivated by a range of physics; precision spectroscopy in mass and frequency [13, 14, 15, 16], ion clocks [17], storage of highly charged ions and antiparticles [18] and quantum information and processing [19], due to its ability to control on the single quantum level. Ion trap experiments most typically focus on the ability to trap (a) a single cold ion for extended interrogation, (b) a collection of ions in the form of a spatially extended cloud [20], or (c) an ordered crystal of ions [21, 22]. Multi-species ions are trapped and sympathetically cooled [23]. Recently experiments have been performed to communicate between trapped ions in remote experiments [24]. Various configurations of ion traps have been developed to meet specific requirements and interests, starting from conventional 3-dimensional (3-D) traps with hyperbolic electrodes [14] to cylindrical traps [25], linear traps [26] and planar traps [27, 28, 29, 30]. Designs with 3-D scalability [31, 32] and ion transport [33] have also been explored.

We propose an ion trap configuration which is three-dimensionally symmetric by its geometry. It resembles the configuration which Wuerker *et al.* used in 1959 [34]. The proposed trap is suited to construct several compact, stacked and identically independent ion traps with a reasonably good optical access in the same apparatus. This chapter describes the discussion on geometry, operating scheme of the trap and determination of parameters for the isolated fundamental trap and the stacked traps.

2.1 Geometry and operation

In this section, the basic structure of the proposed trap and its operating scheme are discussed. The basic structure is a building block for the lattice of iontrap. The lattice of ion traps is an extended array of the basic trap and consists of $l \times m \times n$ number of
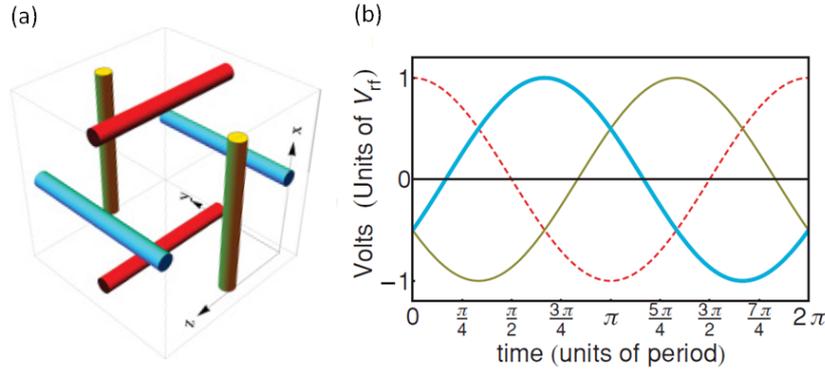
Figure 2.1: Basic electrode configuration: (a) Basic electrode configuration of the ion trap: three pairs of parallel electrodes are arranged along the Cartesian axes and are electrically contacted. (b) The relative phase difference of $2\pi/3$ between the orthogonal electrode sets, where RF voltage applied along $\hat{x}$, $\hat{y}$ and $\hat{z}$ are represented by thin, thick, and dashed lines, respectively.

equivalent traps. $3 \times 3 \times 3$ version of the lattice of ion traps is illustrated [35].

2.1.1 Basic trap

The basic trap is constructed with three parallel pairs of cylindrical electrodes along the Cartesian axes, illustrated in Fig. 2.1 (a). Equipotential is applied to the parallel electrodes to create 3-D time-varying potentials. The $2\pi/3$ phase difference of the applied radio-frequency (RF) field among parallel electrodes along $\hat{x}$, $\hat{y}$ and $\hat{z}$ is shown in Fig. 2.1 (b). The field configuration creates the rotating saddle potential which traps the ions in a 3-D symmetric configuration over one full cycle.

2.1.2 Lattice of ion traps (LIT)

The symmetry of the trap gives an advantage to form the lattice of iontraps with any number of equivalent traps. $3 \times 3 \times 3$ version of the lattice of ion trap is illustrated in the Fig 2.2 (a). This particular combination is the lowest-order cubic arrangement that provides lattice sites with four distinct locations of ion traps; body centre (BC), face centre (FC), edge centre (EC), and corner (C), shown in Fig. 2.2 (b). Its operation
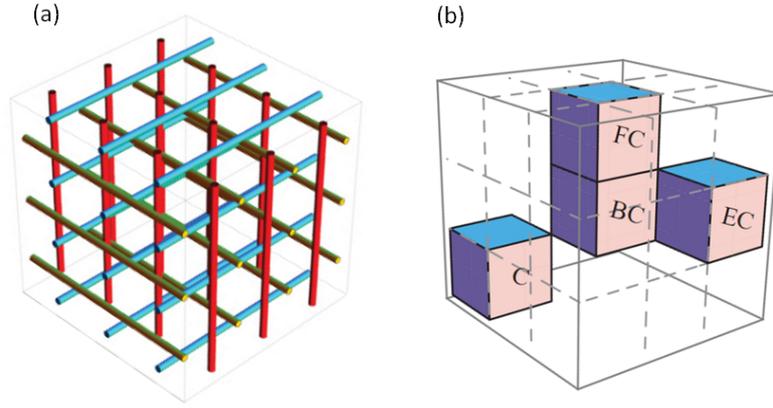
Figure 2.2: 3 × 3 × 3 lattice of ion traps: (a) illustrates the extension of the trap in 2.1 (a) to 27 LIT in a simple cubic arrangement. (b) Four distinct types of coordination symmetries for traps at different locations: Representative cells of different coordinations are identified as BC(6), FC(5), EC(4), and C(3), where the number of location-dependent nearest-neighbor cells is given in parentheses.

remains the same. Equipotential of radio frequency with the $\frac{2\pi}{3}$ phase shift relation creates 3-D symmetric potential over one cycle in each lattice site. The site-specific effects on the trapped ions in BC, FC, EC and C are insignificant. The detailed characterization is discussed in the section, 2.4.2.

2.2 Design of the potential

For three dimensional confinement of charged particles, the force corresponding to the trap potential is directed toward the energy minimum point in space and can have any arbitrary form in coordinate. For convenience, a harmonic potential is favoured. Thus we take a potential energy, U of a quadratic form in the Cartesian coordinates x, y, z, as follows:

$$U(x, y, z) = \gamma(Ax^2 + By^2 + Cz^2), \tag{2.1}$$

where γ is a constant and A, B, C can be a time dependent function. So the electrostatic field Ψ acting on an ion of charge Q gives $U = Q\Psi$, where Ψ is given as

$$\Psi(x,y,z) = \frac{\Psi_0}{2R_0^2}(Ax^2 + By^2 + Cz^2) \tag{2.2}$$

To find appropriate values for A, B and C, Laplace's equation should be satisfied,

$$\Delta\Psi = 0 \tag{2.3}$$

This leads to $A + B + C = 0$. In this study, we are particularly interested in an ion trap, in which equipotential of radio frequency is applied with the $\frac{2\pi}{3}$ phase shift relation creating 3-D symmetric potential over one cycle.

$$
\begin{aligned}
A(t) &= \cos\left(2\pi\nu_{rf}t + \frac{4\pi}{3}\right) \\
B(t) &= \cos\left(2\pi\nu_{rf}t + \frac{2\pi}{3}\right) \\
C(t) &= \cos\left(2\pi\nu_{rf}t\right)
\end{aligned}
\tag{2.4}
$$

where ν_{rf} is the driving micromotion frequency of the trap. One can check, at time $t = 0$, $A = B = -\frac{1}{2}$ and $C = 1$, so $A + B + C = 0$. It holds true for all t. Therefore, by substituting Eq. 2.4 in Eq. 2.2, the trapping potential with amplitude of radio-frequency, V_{rf} is

$$\Psi(x,y,z,t) = \frac{V_{rf}}{2R_0^2}\left(x^2\cos\left(\Omega t + \frac{4\pi}{3}\right) + y^2\cos\left(\Omega t + \frac{2\pi}{3}\right) + z^2\cos\left(\Omega t\right)\right)$$

where R_0 is the distance of the electrode from the trap centre and $\Omega = 2\pi\nu_{rf}$.

2.3 Numerical simulation

2.3.1 Potential

To validate the trapping of Ca^+ ions in the basic trap and 27 LIT, we simulated the motion of a single ion in the trapping potential. Electrodes along $\hat{x}$, $\hat{y}$ and $\hat{z}$ are biased as shown Fig. 2.1 (b). Ions are dynamically trapped in the time varying potential. The ion motion in $\hat{x}$, $\hat{y}$ and $\hat{z}$ consists of average macromotion of frequency, ν_m and trapping field frequency driven micromotion of ν_{rf}.

The potential of the basic trap and 27 LIT are calculated using SIMION 7 [36]. In SIMION 7, the geometry of the electrodes with the voltages applied is defined in a geometry file (.gem file). From the geometry file, SIMION 7 then generates a potential array which is a three-dimensional array of the entire trapping region. The potential array is imported to MATHEMATICA 7 for solving the equations of motion of a single ion numerically.

2.4   Trap characterization: Stability and power spectrum

Stability diagram of an ion trap is obtained using Mathieu's equation. It shows the stable trapping parameters, which can be derived by solving the equation of motion. We will first go through the stability diagram for an ideal linear Paul trap.

2.4.1   Stability for a linear Paul trap

A linear Paul trap typically consists of four cylindrical rods parallelly arranged in quadrupole configuration. RF voltage is applied between diagonally connected pairs of the four electrodes and a DC electric field is superimposed. An oscillating electric potentials ϕ in the radial direction is [37]

$$\phi(x, y, t) = (U_{dc} + V_{rf} \cos \Omega t) \frac{x^2 - y^2}{2R^2},$$
(2.5)

where R is the radial distance from the centre of the trap to the quadrupolar electrode, V_{rf} is the amplitude of the radio frequency(rf) voltage, RF frequency applied and U_{dc} is a DC offset for the radio-frequency voltage in the quadrupole rods. The equations of motion of an ion of mass M and charge Q in this potential is expressed as follows,

$$\begin{aligned}
\frac{d^2 x}{dt^2} &= -\frac{Q}{M} \left(\frac{U_{dc} + V_{rf} \cos \Omega t}{R^2} \right) x, \\
\frac{d^2 y}{dt^2} &= -\frac{Q}{M} \left(\frac{-U_{dc} - V_{rf} \cos \Omega t}{R^2} \right) y.
\end{aligned}$$
(2.6)
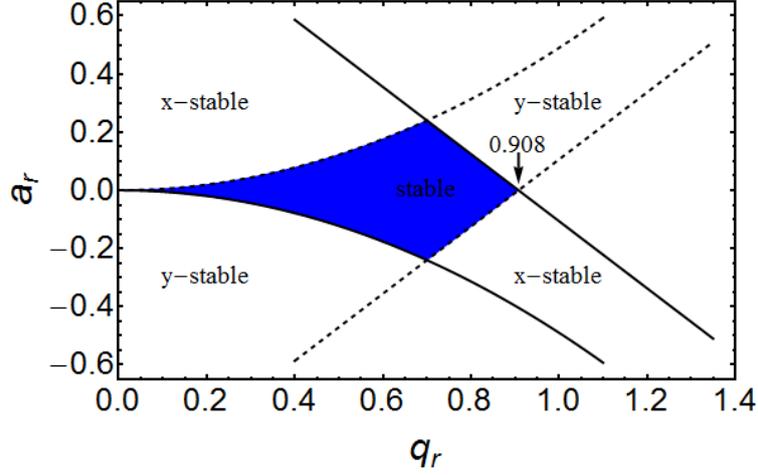
Figure 2.3: : The first stability region in the radial direction for a linear Paul trap. q ranges from 0 to 0.908 for $a = 0$.

The equations of motion can be arranged in the homogeneous Mathieu equation of the form,

$$\frac{d^2 u(\tau)}{d\tau^2} + (a_u - 2q_u \cos 2\tau)u(\tau) = 0, \tag{2.7}$$

where $u = x, y$ and $\tau = \frac{\Omega t}{2}$.

By making the substitutions, we obtain modified stability parameters for the ideal linear Paul trap:

$$a = \frac{4QU_{dc}}{MR^2\Omega^2}, \quad q = -\frac{2QV_{rf}}{M\Omega^2 R^2},$$

where $a = a_x = -a_y$ and $q = q_x = -q_y$. The Mathieu equations give the stability and instability of the solutions, depending on a and q. There are stability regions in x and y directions. The first stability region for the ideal linear Paul trap potential of the form of Eq. 2.5 is the common stability regions in x and y directions, as shown in Fig. 2.3. For $a = 0$ axis, the first region of stability region ranges from $q = 0$ to $q \approx 0.908$.

2.4.2   Stability of the basic trap and LIT

Stability parameters a and q, related to the Mathieu differential equation for the linear Paul trap are not fully relevant, as $a = 0$. However,

$$q = \frac{4QV_{rf}}{M(2\pi\nu_{rf})^2 R_0^2} \tag{2.8}$$

still remains as a stability parameter for trap characterization. To characterize it, typical dimensions of an electrode diameter of 0.5 *mm* and a centre-to-centre separation of 5 *mm* are used. The dimensions can be changed without qualitative change in the trap properties, so that makes $R_0 = 2.5$ mm. The potential of basic trap and 27 LIT is shown in Eq. 2.2. The numerical potential is calculated as described in the section 2.3.1 Potential. The numerical potential from SIMION 7 is interpolated in Mathematica using 'ListInterpolation.' The 'NDSolve' in-built function in Mathematica is used in solving the equations of motion numerically. The equations of motion for a Ca^+ ion in the potential, V_{tot} is given by

$$
\begin{aligned}
M\frac{d^2x}{dt^2} &= -Q\frac{\partial}{\partial x}V_{tot}(x,y,z,t) \\
M\frac{d^2y}{dt^2} &= -Q\frac{\partial}{\partial y}V_{tot}(x,y,z,t) \\
M\frac{d^2z}{dt^2} &= -Q\frac{\partial}{\partial z}V_{tot}(x,y,z,t)
\end{aligned}
\tag{2.9}
$$

The conditions for stable confinement of an ion with mass, M and charge, Q in the 3-D lattice of ion trap can be derived by solving the equations of motion in the time-varying potentials. In general, stability diagram for Mathieu's equation is used for the trap characterization.

In general, stability diagram for Mathieu's equation is used for the trap characterization. However in our case as $a = 0$, the trap is characterized by relating the rf amplitude V_{rf}, the magnitude of the initial velocity of the trapped ions $|\mathbf{v}_0|$, and ν_{rf}, RF applied to the electrodes. We solve the equations of motions with the initial position of the ion at the trap centre and the initial velocity, $\mathbf{v}_0$ of equal components in the three orthogonal directions. In Fig. 2.4 (a), the boundary of the region of stability
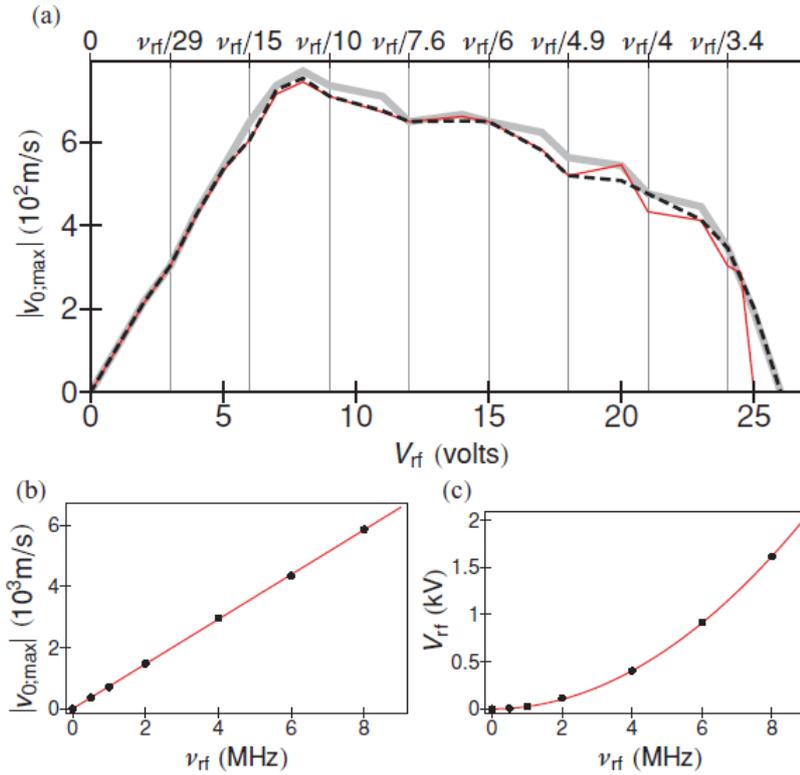
Figure 2.4: Trap characterization: (a) Boundary of stability region is plotted in the $|\mathbf{v}_0|$ vs. V_{rf} plane at $\nu_{rf} = 1$ MHz. The dashed (black), thin (red), and thick (grey) lines are the boundaries of stability region for the basic trap in Fig. 2.1 (a), BC and C cells which are configurationally the most distinct cells in the LIT. The maximum trappable (b) initial velocity $|\mathbf{v}_{0;max}|$ and (c) amplitude of the RF voltage for the $^{40}\text{Ca}^+$ ion are plotted as a function of ν_{rf}. The lines in (b) and (c) are fitted to the points and are linear and quadratic in ν_{rf}.

is plotted in $|\mathbf{v}_0 - V_{rf}|$ plane, where $\nu_{rf} = 1$ MHz, calculated for the single trap, BC and C locations. The difference in trapping potential for single trap, BC and C in 27 LIT causes the small variation in the trapping region. Traps at BC and C locations are susceptible to their immediate neighbourhood. BC has 6 nearest neighbouring cells and C has 3. Fig. 2.4 (a) shows that the differences due to trap location in LIT are minor. Particle motion in the oscillating potential has two components; macromotion and micromotion. The macromotion is a smooth average motion superimposed on a small amplitude fast oscillating micromotion, driven by the rotating potential at frequency, ν_{rf}. The macromotion frequency can be calculated from stability parameters, a and q. It has a following relation;

$$\nu_m = \frac{1}{2}\beta\nu_{rf} \tag{2.10}$$

where $\beta = \sqrt{a + \frac{q^2}{2}} = \frac{q}{\sqrt{2}}$. Therefore, ν_m is expressed as,

$$\nu_m = \frac{1}{2\sqrt{2}}\frac{4QV_{rf}}{M(2\pi\nu_{rf})^2R_0^2}\nu_{rf}. \tag{2.11}$$

ν_m depends on V_{rf} as well as ν_{rf}. The top axis in Fig. 2.4 (a) marks the macromotion frequency ν_m for the basic trap. As V_{rf} increases, the resultant amplitude of ion motion increases rapidly, thus taking the ions to the trap boundary and ejecting them. Therefore, deeper trap potentials do not imply trapping of ions with higher kinetic energies, as illustrated by the fall in stability region, $|\mathbf{v}_{0;\mathbf{max}}|$ beyond $V_{rf} > 8$ V in Fig. 2.4 (a). This also suggests that the suitable operating parameters to trap ions are $V_{rf} \leq 8$ V at $\nu_{rf} = 1$ MHz where $|\mathbf{v}_{0;max}|$ has a linear with V_{rf}. Generating multiple $|\mathbf{v}_0| - V_{rf}$ stability plots for different ν_{rf} and compiling the results provided the data for Fig. 2.4 (b) and (c). Fig. 2.4 (b) illustrates that maximum trappable initial velocity of the ion, $|\mathbf{v}_{0;max}|$ increases linearly with ν_{rf}. Fig. 2.4 (c) demonstrates that the maximum trapping voltage $V_{rf;max}$ scales as ν_{rf}^2 consistent with the behavior for constant q, here $q = 0.908$, which is the end limit of the stability region and barely traps the zero-velocity ion. Thus the bounds for the operation of the present ion trap are well characterized via the scaling functions shown.
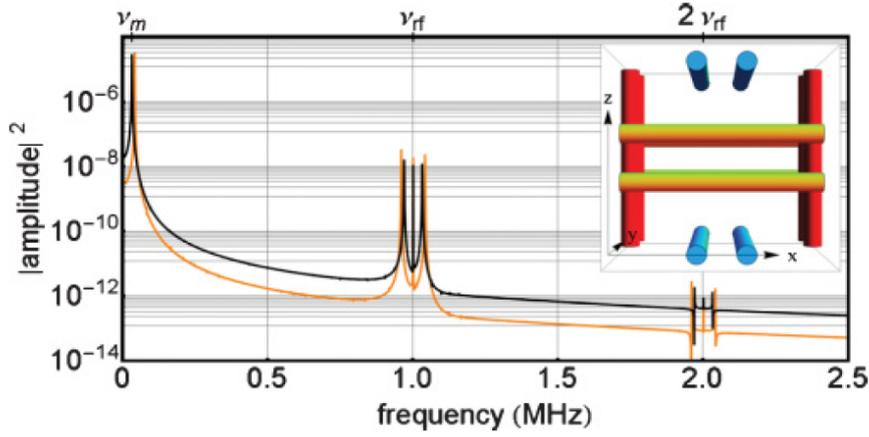
Figure 2.5: Power spectrum of the $\hat{x}$ component of the trajectory for a low $|\mathbf{v}_0|$ ion computed at ν_{rf} = 1 MHz, V_{rf} = 3 V: (i) for the electrode configuration in Fig. 2.1 (a), black curve, and (ii) for the split electrode configuration in the inset, orange trace. For both power spectra, a strong macromotion peak at ν_m and significantly weak peaks at ν_{rf}, $\nu_{rf} \pm \nu_m$, $2\nu_{rf}$ and $2\nu_{rf} \pm \nu_m$ are seen.

2.4.3 Power spectrum

Symmetric operation and geometric structure of the trap give identical macromotion frequencies ν_m in the orthogonal $\hat{x}$, $\hat{y}$ and $\hat{z}$ directions. Eq. 2.11 shows that ν_m depends only on trap parameters and not on initial state of the ion. Therefore, there is no change in ν_m for a large value of $|\mathbf{v}_0|$. To obtain the power spectrum of the ion trajectories, we apply the Fourier transformation to the solution of Eq. 2.9. Fig. 2.5 shows the power spectrum of the $\hat{x}$ component of the ion trajectory, which is free of sidebands, indicating that the trap is harmonic. Since the macromotion of the ion at ν_m is superimposed with the micromotion from RF driving field at ν_{rf}. The power spectrum clearly exhibits two major frequencies and their harmonics. These two frequencies, ν_m and ν_{rf} are identified and marked on the top axis of Fig. 2.5. For small $\mathbf{v}_0$ and low q values, ν_m remains the same across traps with different coordinate numbers. The uncertainty in ν_m determination from the simulation is within $\pm 0.01\nu_{rf}$. Computational convergence limit in solving Laplace equation causes this uncertainty. Basic trap and 27 LIT do not have a face-on view of the ion. Traps can be modified to have a direct access, by

splitting each of the six electrodes into two, as shown in the inset of Fig. 2.5. Power spectrum of such splitted trap show a slight shift in ν_m as compared to that in other traps. Therefore, the split trap has a similar performance to the basic trap.

2.5 Practical implementations

2.5.1 Loading of ions in LIT

To load LIT with the desired number of ions is most efficiently achieved by resonance-enhance two-photon ionization. Briefly, the RF fields can be applied while a vapor of the parent neutral floods that lattice. Applying the two laser frequencies for the ionization, along two distinct directions of easy viewing through the lattice, would create ions only at the beam intersection. Thus an ion(s) can be loaded in a controlled way in each ion trap cell, close to the center of the individual traps. Laser cooling of ions to ultracold temperatures, now well established, is easily done along the easy viewing directions.

2.5.2 Optical Access

The proposed ion trap, due to the sinusoidal, three-phase variation of the solution of the Laplace equations, is tightly constrained by the uniqueness theorems. Alternative configurations of ion traps which yield degenerate frequencies with sinusoidal time variation will be qualitatively identical to the trap above. It is also found that the trap degeneracies are preserved for small trap misalignments, while degeneracies are preserved for small trap misalignments, while a 3% deviation in electrode placement leads to a breakdown of the frequency degeneracy. The optical access (OA) at the centre of the trap in Fig. 2.1 (a) is OA $\approx 0.81 \times (4\pi)$ sr, while the central trap in the LIT has OA $\approx 0.58 \times (4\pi)$ sr. This makes the addressing of ions in the LIT practical.
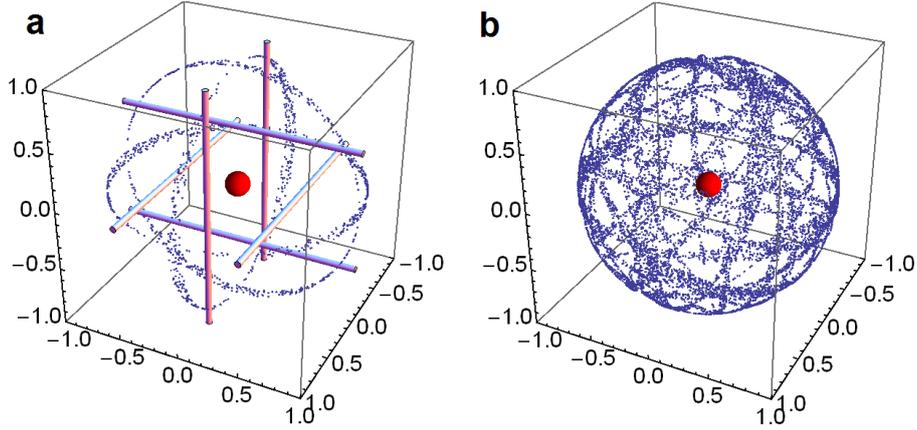
Figure 2.6: Optical access (OA): OA is calculated using Monte Carlo simulations. (a) shows the OA for the basic trap. In the Monte Carlo simulation, particles are allowed to fly radially outwards from positions having the same radii with randomly varying θ and ϕ in the spherical coordinate, i.e. from the surface of the red sphere at the centre. We count particles which are not blocked/hit by the electrodes. Blue dots indicates the particles which are hit by the electrodes. That gives a fraction of optically accessible solid angle to not accessible solid angle. In the similar way, OA is calculated for the central trap in the LIT, as illustrated in (b).

2.6 Applications

The ease of addressing the ions at each lattice site, individually or simultaneously, makes the proposed trap naturally suitable for a number of experiments. Few applications of the trap are discussed in detail.

2.6.1 Spectroscopic measurements

The most precise spectroscopic measurement on a system would be on an isolated, trapped single particles, nearly at rest. However, in the specific case of a single ion confined within an ion trap, a serious constraint is presented by the low flux of the photons and hence the signal-to-noise ratio ($\Re_{S/N}$) in the detection. Adding more than one ion per ion trap leaves the system vulnerable to perturbations that could compromise the precision of the measured transition frequencies. With the experimental setup proposed here, we have the ability to preserve the isolation of the individual ions in

each trap, while increasing the detected fluorescence rate.

Specifically the performance of single-ion optical clocks may be improved when a single ultracold ion is trapped within each cell of the LIT. The stability of clocks is expressed by the Allen variance, which is intended to estimate stability due to noise processes and describes the stability in frequency,

$$\sigma = (\Delta \nu / \nu)(\Re_{S/N})^{-1/2} \times \tau_{int}^{-1/2}, \tag{2.12}$$

where ν is the transition frequency, $\Delta \nu$ is the observed linewidth, and τ_{int} is the integration time. In the arrangement illustrated in Fig. 2.2 (a), 27 such trapped ions can be interrogated simultaneously, increasing the $(\Re_{S/N})$. This results in a decrease in the short-term instability of about a factor of 5.

2.6.2 Quantum information processing

Information processing with ion traps allows the most precise control over qubits thus far. Ion traps suit most of DiVincenzo's criteria. However, one practical limitation faced by most ion trap quantum information experiments is poor scalability as number of qubits increases in the trap and, to an extend, precise individual addressing of the ions trapped in the ground vibrational state of a trap. Also, for low-$\mathbf{v}_0$ and low-q operation, the trap frequency ν_m is coordination number independent. In addition, traps with the same coordination number are, by definition, identical. Thus if one desires to operate with only one qubit per site, this system is ideally suited.

Further, the ground state of the effective harmonic oscillator trap for the 3-D ion trap configuration is non degenerate. However, for the center-of-mass oscillations, the excited states in the symmetric operation mode of the trap exhibit degeneracy. Thus the usual cooling mechanisms (laser and sideband) essential for the population of the ground vibrational state of the trap with the ion(s) are unchanged. In addition, deterministic numbers of ions can be loaded per lattice site in the ground state. In the specific case of two ions per trap cell, the key to entangling them or performing gate operations with existing protocols [38] may depend on the heating rate of the ions from

their ground state in the trap. The heating rate has not been evaluated in the present work. The present ion trap has a point rf node, as opposed to the linear rf node of the more conventional linear Paul trap geometries that are currently in use for quantum information processing. Thus, the feasibility of usable two-/multi-ion entanglement in the proposed configuration bears further investigation. Another difference which arises due to the high symmetry in an overall rotational motion about the center of mass of the trapped ions, which, due to the distance between two ions in the trap ground state (several micrometers), is very slow ($\approx$ 1 Hz) compared with other relevant time constants in such systems. In many-particle entanglement can be proven for this structure, either with present-day technology or with a protocol or system yet to be developed, scaling will naturally follow. The fact that, by asymmetric application of either constant or rf voltage, the trap degeneracy can be lifted for the excited states offers other degrees of freedom for exploitation in the future. Thus the LIT offers a new architecture for quantum information processing with ions [28].

2.6.3 Experimental realization of few body problems

Another rich area of study with the 3-D ion trap is the experimental few-body problem. The present-day ability to load a controlled number of atoms, molecules or ions in the lowest-energy states of traps allows attempts at quantitative studies with these very challenging systems. Linear Paul traps have long supported ion crystals which order in shells about the trap axis [39, 40, 41]. The 3-D ion trap would fill in a three-dimensionally symmetric fashion. Problems such as minimum energy configurations, phon mode excitations and crystal relaxation, rotations, and effect of trap symmetry and its changes can be probed. The symmetry of the present trap can be dramatically altered from a totally symmetric to a completely asymmetric configuration (i.e., $v_{m;x} = v_{m;y} = v_{m;z} \longleftrightarrow v_{m;x} \neq v_{m;y} \neq v_{m;z}$) with small differences in electrode voltages. In the highly asymmetric configuration the system can be driven into chaotic behavior as evident from single, trapped ion trajectory simulations, which exhibit a dense power spectrum. The ability to catch the ion signal in fluorescence makes trapped ions the

natural choice for mapping both the equilibrium configurations and the dynamics of a system of a few, bound particles. Such studies with trapped ions are relevant across disciplines in physics.

2.7 Conclusion

The concept of the ion trap described here is versatile and suitable for many experiments over and above [42] those discussed here. The trap operating parameters determined here are easily scaled for difference Q/M and trap dimensions. Its primary strengths lie in the ease with which multiple, identical ion traps can be realized and the ability to adapt the trap symmetry to a specific problem without additional experimental complexity.

Experimental arrangement and details

Now we turn our attention back to the ion−atom experimental set up. In this chapter, we shall describe in detail an experimental set up to confine ions and atoms with spatial overlap, its operation and characterization which would be the main basis for ion-atom and ion-molecule experiments discussed in the later chapters. We begin with brief discussion on optical molasses for a two level system and magneto optical trapping using a quadrupole magnetic field. Implementation and diagnosis of magneto optical trap (MOT) are described. The second major discussion is on ion trapping. To combine MOT and ion trap, we choose a modified linear Paul trap for our experiment. We will concentrate mostly on characterization of the ion trap since design of the ion trap has been already covered in the thesis work by Ravi Krishnamurthy [43]. Finally, an additional set up constructed for ion-molecule collisions is discussed.

3.1 Magneto Optical Trap

Magneto-optical trap (MOT) is the most widely used technique for neutral atoms, employing both optical molasses technique and quadrupole magnetic field. The principle and experimental set up of the MOT are illustrated in the following sections.

3.1.1 Background

Optical molasses for a two level system

For a two level atom with atomic resonance frequency, ω_0, in a pair of counter-propagating laser beams of frequency ω_L, the magnitude of the scattering force, $F_\pm$ equals the rate at which the absorbed photons impart momentum, $\pm\hbar k$ to the atom. The photon absorption rate is $\Gamma\rho_{ee}$, where ρ_{ee} is the fraction of the population in the excited state, $|e\rangle$.
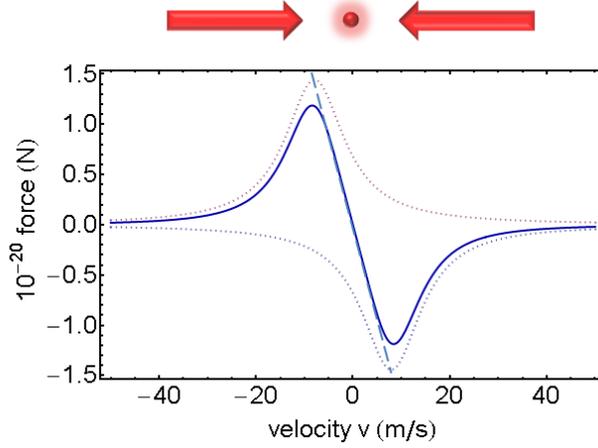
Figure 3.1: Velocity-dependent force for an one-dimensional optical molasses: Figure illustrates the scattering force as a function of velocity (solid lines) for a ^{85}Rb atom in optical molasses where $I = 3.5$ mW/cm^2 per beam, $\delta = 15$ MHz (below the resonance). The forces produced by each counter propagating laser beams are plotted as dotted lines.

The scattering force [44] is expressed as,

$$\mathbf{F}_{\pm}(v) = \pm\hbar\mathbf{k}\left(\frac{\Gamma}{2}\right)\frac{I/I_{sat}}{1 + I/I_{sat} + 4(\delta \mp \mathbf{k}\cdot\mathbf{v})^2/\Gamma^2} \tag{3.1}$$

where v is the velocity of the atom, $\hbar\mathbf{k}$ is the photon momentum, $\delta = \omega_L - \omega_0$ is the detuning of laser frequency from the atomic resonance, Γ is the decay rate of the excited state, I is the intensity of the laser beam and I_{sat} is the saturation intensity of the transition. The forces from the two counter-propagating gives

$$\mathbf{F}_{OM} = \mathbf{F}_+ - \mathbf{F}_- \approx \frac{8\hbar k^2 \delta I/I_{sat}}{\Gamma(1 + I/I_{sat} + 4\delta^2/\Gamma^2)}\mathbf{v} = -\beta\mathbf{v}, \tag{3.2}$$

where β is the damping coefficient.

For $\delta < 0$ (red-detuned), optical molasses force, $\mathbf{F}_{OM}$ opposes the velocity ($\propto -\mathbf{v}$) and therefore provides viscous damping for the motion of the atom. The sign of force is negative when $v > 0$ and positive when $v < 0$, and so the force decelerates atoms. Fig. 3.1 shows the velocity dependent scattering force on a ^{85}Rb atom in optical molasses under our experimental parameters.
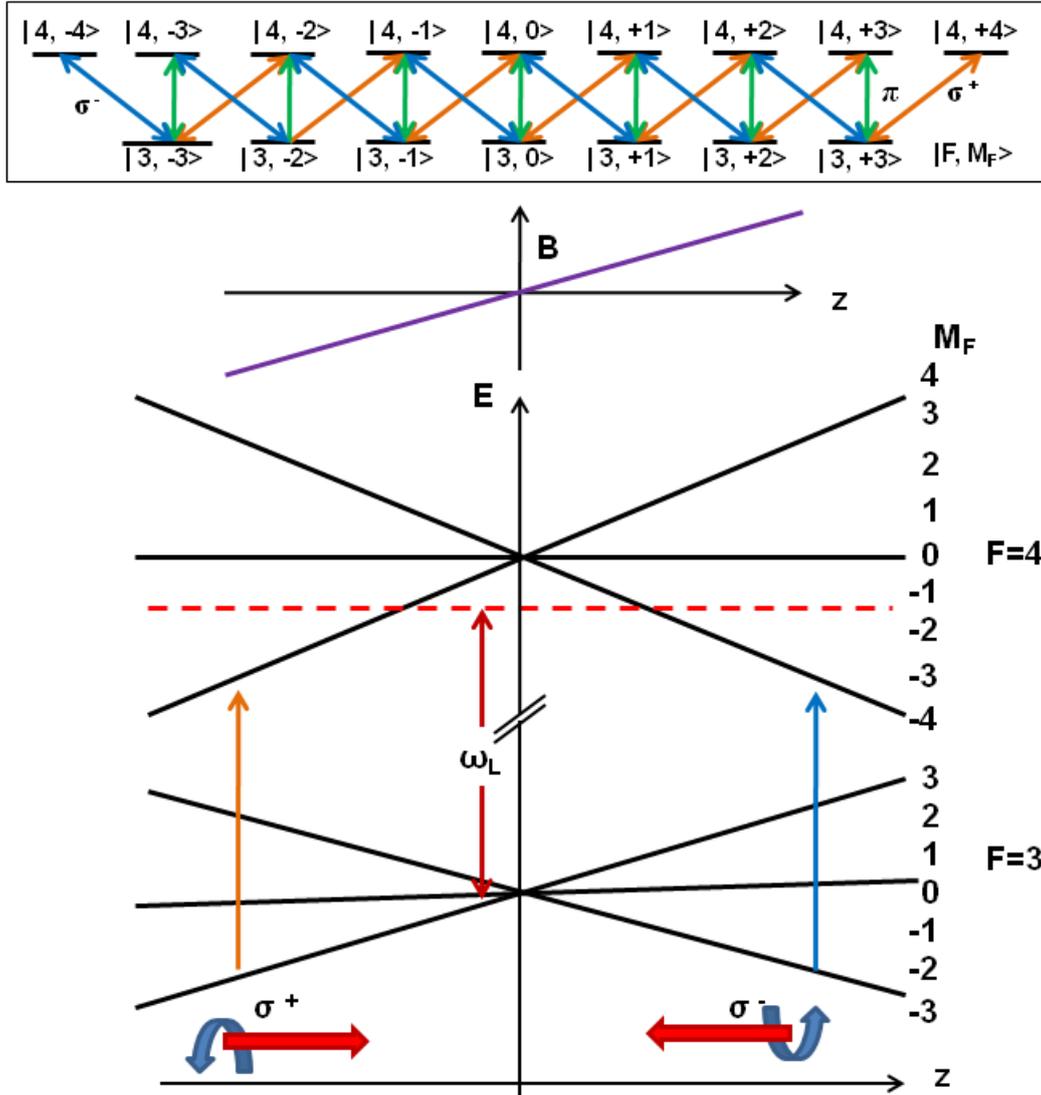
Figure 3.2: Fig. illustrates 1 D magnetic field (**B**) for MOT and simplified MOT scheme for $|F = 3\rangle \rightarrow |F = 4\rangle$ transition. Inset shows the selective absorption of the circularly polarized light and magnetic sub levels for $F = 3$ and $F = 4$ (orange line indicates σ^+ transition. Green line is for π transition and blue line is for σ^- transition).
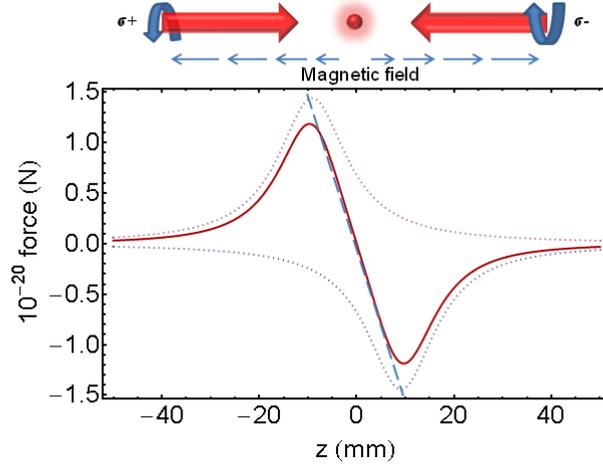
Figure 3.3: Position dependent force for an one-dimensional magneto-optical trap : Figure illustrates the scattering force as a function of position (solid lines) for a ^{85}Rb atom in optical molasses with quadrupole magnetic field, where $I = 3.5\,\mathrm{mW/cm^2}$ per beam, $\delta = 15\,\mathrm{MHz}$ and $\frac{dB}{dz} = 12\,\mathrm{G/cm}$. The forces produced by each counter propagating laser beams are plotted as dotted lines.

Magneto optical trapping of ^{85}Rb

The addition of a quadrupole magnetic field to counter-propagating σ^+ and σ^- red-detuned cooling light causes a spatial imbalance in the scattering force which defines a centre for the force and thus enables spatial trapping of the atoms. In a MOT, a uniform magnetic field gradient perturbs the atomic energy levels, $M_F = 0, \pm 1, \pm 2, \pm 3$ of the $F = 3$ level and $M_F = 0, \pm 1, \pm 2, \pm 3, \pm 4$ of the $F = 4$ level, varying linearly with position of the atom, as shown in Fig. 3.2. When an atom is displaced from the centre of the trap along the z-axis with $z > 0$ ($z < 0$), the $M_F = -4$ (+4) is closer in energy, towards resonance with the red-detuned laser light. Due to angular momentum conservation, atoms excited from $M_F = -3$ (+3) to $M_F = -4$ (+4) states preferentially absorb σ^- (σ^+) polarized light, shown in inset of Fig. 3.2, which imparts a net force towards zero of the magnetic field, which coincides with the centre of the optical molasses. The scattering force, Eq.(3.1) with the additional magnetic field becomes,

$$\mathbf{F}_{\pm}(v, z) = \pm \hbar \mathbf{k} \left(\frac{\Gamma}{2} \right) \frac{I/I_{sat}}{1 + I/I_{sat} + 4(\delta \mp \mathbf{k} \cdot \mathbf{v} \pm \mu'(dB/dz)z/\hbar)^2/\Gamma^2}, \tag{3.3}$$
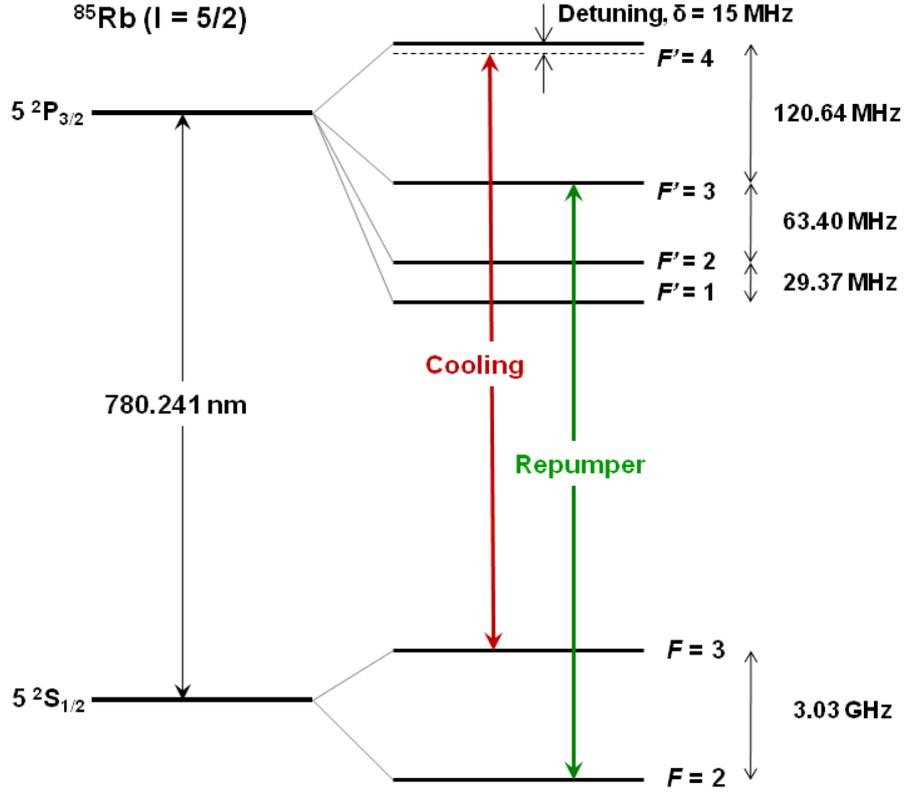
Figure 3.4: Rb D2 line manifold: illustrates hyperfine structure, with frequency splittings between the hyperfine energy levels (not in scale) [45].

where dB/dz is the magnetic field gradient, $\mu' \equiv (g_e M_e - g_g M_g)\mu_B$ is the effective magnetic moment for the transition between ground, g and excited, e states, $M_{g,e}$ is the magnetic quantum number and μ_B is the Bohr magneton [44]. The net scattering force in the quadrupole magnetic field is the sum of two forces and is given by

$$\mathbf{F}_{MOT} = \mathbf{F}_+ + \mathbf{F}_- \approx -\beta\mathbf{v} - \kappa_s\mathbf{r}, \tag{3.4}$$

where κ_s is the spring constant and is given by,

$$\kappa_s = \frac{\mu'(dB/dz)}{\hbar k}\beta. \tag{3.5}$$

In the MOT experiment, this one-dimensional scheme is applied in three orthogonal directions. The cooling transition for ^{85}Rb is

$$\left|5^2S_{\frac{1}{2}}, F = 3, M_F = 3\right\rangle \rightarrow \left|5^2P_{\frac{3}{2}}, F' = 4, M'_F = 4\right\rangle,$$

which is labeled in Fig. 3.4, ^{85}Rb D2 transition hyperfine structure. Fig. 3.3 shows the
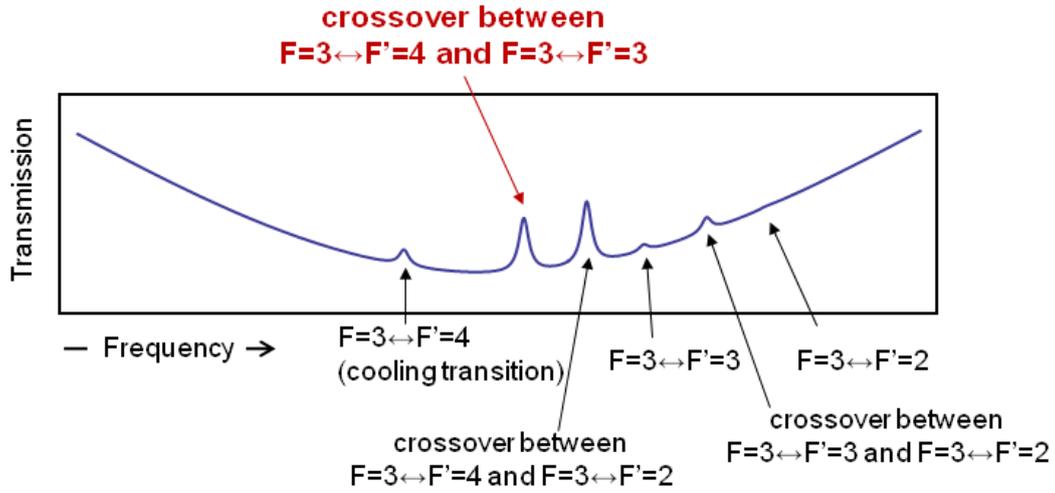
Figure 3.5: Saturation absorption spectroscopy spectrum of ^{85}Rb: The spectrum shows transition lines between $\left|5^2S_{\frac{1}{2}}, F = 3\right\rangle \rightarrow \left|5^2P_{\frac{3}{2}}, F'\right\rangle$. The experimental setup of saturation absorption spectroscopy is shown in Fig. 3.6. The laser frequency is locked to the crossover between $F = 3 \leftrightarrow F' = 4$ and $F = 3 \leftrightarrow F' = 3$.

position dependent scattering force on a ^{85}Rb atom in the MOT under our experimental parameters. The force is negative when $z > 0$ and positive when $z < 0$ so the force decelerates atoms towards the centre of the trap, where the atoms accumulate. These atoms have a well-defined temperature and a Gaussian density profile about the $\mathbf{B} = 0$ and the symmetry point of the intersecting laser beams. The atoms in the MOT do not interact with each other to a very good approximation.

3.1.2 MOT experimental setup

Lasers

The atoms to be cooled in the MOT require cooling and repumping light which are produced from an external cavity diode laser (ECDL) by diffracting grating in a Littrow reflecting configuration. In the lab, we use both home-built ECDL and Toptica DL100 system for cooling and repumping light respectively. Fig. 3.4 illustrates cooling and repuming transitions for a ^{85}Rb atom. Cooling laser is slightly red detuned from $\left|5^2S_{\frac{1}{2}}, F = 3\right\rangle \rightarrow \left|5^2P_{\frac{3}{2}}, F' = 4\right\rangle$. This transition is closed, an atom excited into the *F=*

4 level spontaneously returns back to the $F = 3$, ground state. However, despite significant frequency mismatch there is still a small finite probability that an atom will undergo spontaneous emission of a photon that leaves the atom in an energy state lower than the $F = 3$, ground state. On an average once in every ten thousand closed cycles, the atom falls into the $F = 2$, ground state. After short time, all the atoms will be pumped to the $F = 2$ state, and the cooling halts. A comparatively weak repumping laser, resonant with the $\left|5^2S_{\frac{1}{2}}, F = 2\right\rangle \rightarrow \left|5^2P_{\frac{3}{2}}, F' = 3\right\rangle$ transition helps to return those leaked atoms back to the cooling cycle.

The laser beams are circularly polarized, which means that the direction of the electric field rotates in a circle at a given fixed point in space as the beam propagates in time. Each pair of opposing laser beams consists of a left circularly polarized (σ^-) and a right circularly polarized (σ^+) counter-propagating beams. The three pairs of oppositely polarized beams in three Cartesian directions with a quadrupole magnetic field trap the laser-cooled atoms. Quarter-wave plates produce a retardation of $\lambda/4$ between the extraordinary and ordinary rays of the linear polarized light through a birefringent crystal. We use the quarter-wave plates to set the appropriate circular polarization states of the MOT beams.

Frequency stabilization

The diode lasers are actively temperature-stabilized and current-stabilized. The cooling and repumping lasers are frequency-locked to an atomic hyperfine resonances which are resolved by saturation absorption spectroscopy (SAS) in a vapour cell. Fig. 3.5 illustrates SAS spectrum which has been measured from an experimental setup (in the green dashed box), shown in Fig. 3.6. A Pound-Drever-Hall system (Toptica: PDD110) generates a differentiated signal of the atomic resonance spectrum, which is fed to a proportional-integral-differential (PID) regulator (Toptica: PID110), which is a generic control loop feedback system and attempts to minimize the error by adjusting the input signal. The output of the PID is then fed to the diode current and piezo actuator to keep the laser frequency locked.
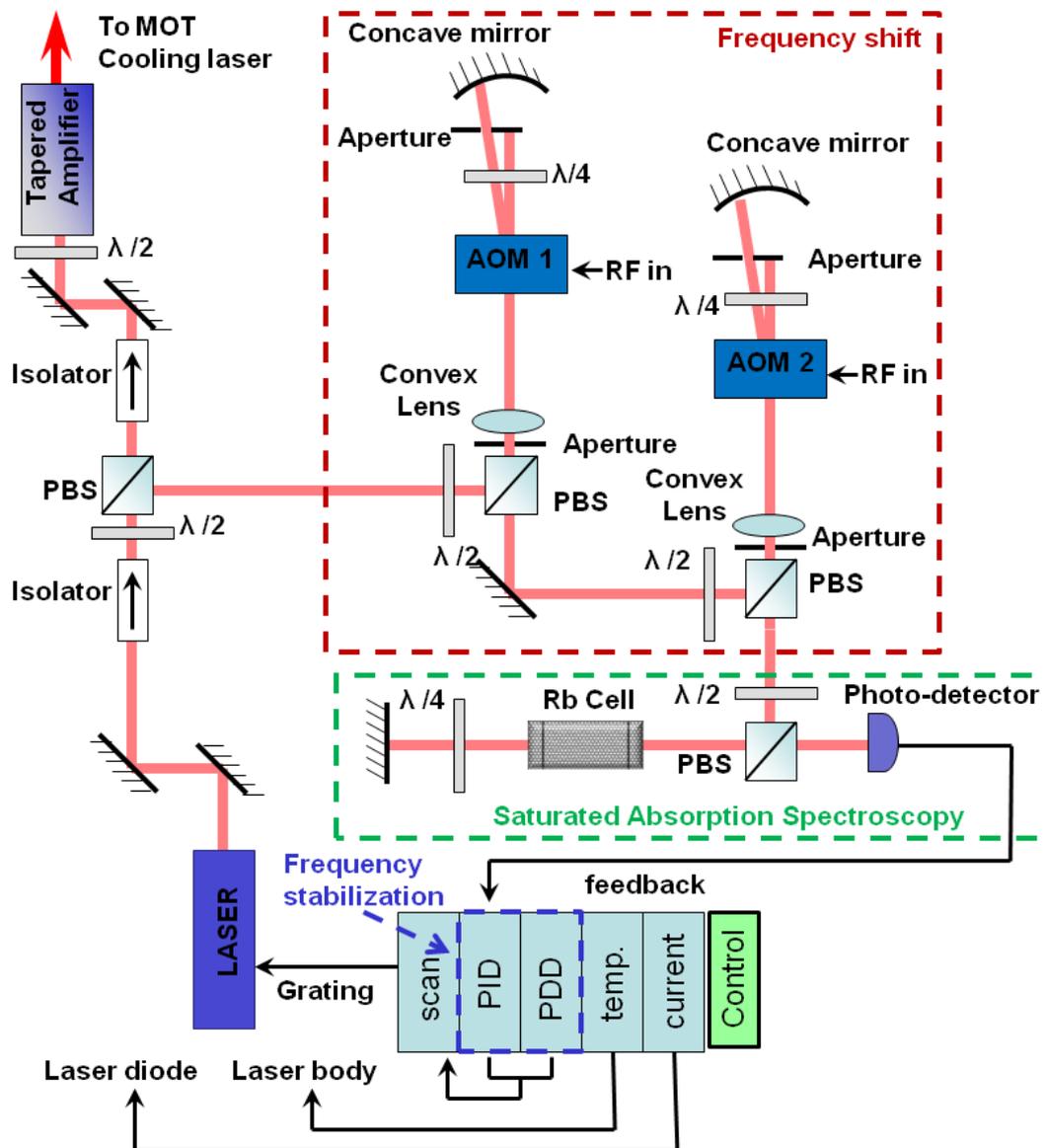
Figure 3.6: Schematic illustrates a set up to prepare the cooling laser with 15 MHz red-detuning to ^{85}Rb D2 transition. The corresponding frequency shift of laser light is made using an acousto-optic modulator (AMO). Then this laser light is intensity-amplified by a tapered amplifier (TA) and sent to a MOT set up. Saturation absorption spectroscopy set up is shown in the green dashed box.

Frequency shift

In the MOT, the cooling laser is 15 MHz red detuned to the ^{85}Rb cooling transition, so in the experiment, we lock at a frequency detuned from the atomic resonance. Acousto-optic modulator (AOM) is employed to achieve a desired frequency shift, as illustrated in Fig. 3.6 (in the red dashed box.) A fraction of laser light is double passed through an AOM with a frequency shift, f_{AOM} calibrated with applied RF voltage. This produces a frequency shift of $f \pm 2f_{AOM}$ in $\pm$1st order of diffracted beam of frequency, f. Commercially available AOMs give a frequency shift of a few hundred MHz. To achieve -15 MHz detuning to the cooling transition, we use two AOMs in double pass. First, laser light is fed to an AOM (Isomet: 1206C), which is operated at $f_{AOM} = 112.5$ MHz. The output of the first AOM in double pass is then fed to the second AOM (Isomet: 1205C), which is operated at $f_{AOM} = -90$ MHz in -1st order. Therefore, the net frequency shift becomes 45 MHz. We perform SAS on the frequency shifted laser light and lock on the crossover line between $F = 3 \leftrightarrow F^{'} = 4$ and $F = 3 \leftrightarrow F^{'} = 3$. This crossover has already a detuning of 60 MHz. That makes the total frequency shift of -15 MHz to the cooling transition.

Magnetic coil

To produce the quadrupole magnetic field, a pair of identical circular copper coils in anti-Helmholtz configuration (with current running through in opposite directions) is used . The field strength increases linearly in all three directions in space. In our set up, the coils of 40 mm in radius have 100 turns and are placed on the top and at the bottom of the vacuum chamber. When a current of 2.6 A is applied to the coils in series, the axial magnetic field gradient is produced to be $dB_z/dz = 12$ Gauss/cm. The separation between each coil centre is 12 cm.

Vacuum system

The vacuum system depicted in Figure 2.7 is constructed from grade 316 stainless steel and is based on the conflat technology, in which a connection between two vacuum
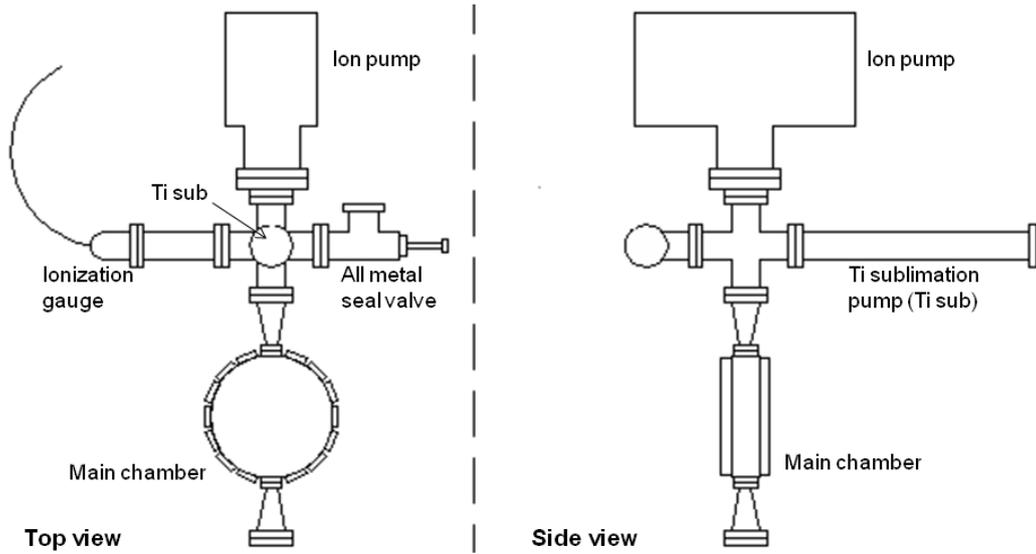
Figure 3.7: UHV system geometry: A simple outline diagram of the vacuum chamber with ion pump (constantly in operation) and titanium sublimation pump. The pressure inside is measured using an ionization gauge.

components is made by tightening flanges. Knife-edges of the flanges bite into copper gaskets placed between the flanges. Ultra high vacuum (UHV) in the system is maintained by a 40 l/s ion pump (Varian: VacIon Plus 919-1210). The ion pump can achieve ultimate pressures of about 10^{-11} mBar. The pressure inside the system is measured primarily with an ionization gauge(Varian: UHV-24) shown in Fig. 3.7. When the vaccum deteriorates due to increase in the vapour pressure of Rb in the chamber, the option of firing titanium-sublimation pump (Varian: TSP) is always available to recover the optimal vacuum. The vacuum chamber is cylindrical in shape with a top-bottom pair of viewports and 16 side viewports, arranged radially outwards as shown in Fig. 3.8.

3.1.3 Loading the MOT

Loading from thermal vapour

The loading rate L [46, 47] depends on the number of background atoms entering the trap region with a velocity smaller than the MOT capture velocity ($v < v_c$) and is
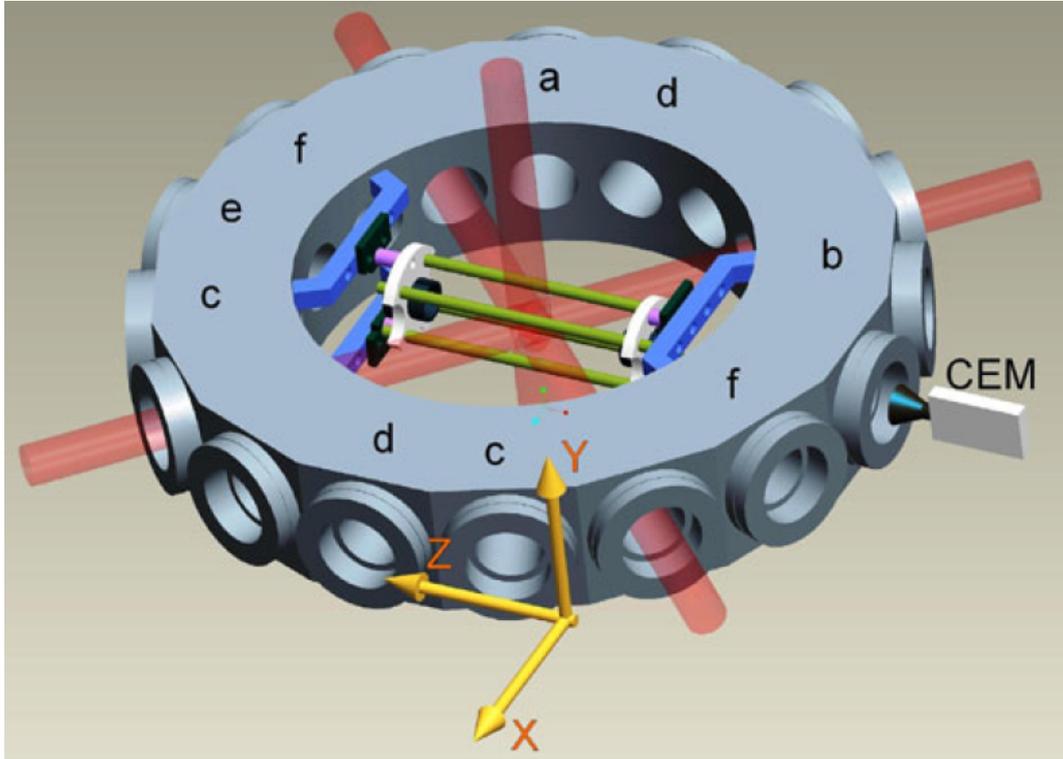
Figure 3.8: Schematic diagram of the experimental chamber (not in scale): The horizontal MOT beams intersect the z axis, at the origin, with 45 and 135 degree angles. The vertical MOT beam intersects this arrangement orthogonally. The magnetic field coils for the MOT (not shown) are external to the vacuum system, mounted symmetrically from the origin coaxial with the y axis. The ports are labeled to illustrate the relative positions of the various components of the experiment as follows; (a) Alkali atom dispensers (connected using a feed-through), (b) the blue-light source, (c) MOT imaging and fluorescence measurement (spatial filtering), (d) femto-watt detector, (e) the vacuum pump connection, and (f) feed-throughs for the ion trap. The ion trap axis is oriented along the z axis. A channel electron multiplier for ion detection is mounted coaxial with respect to the ion trap axis, in the z direction.

31
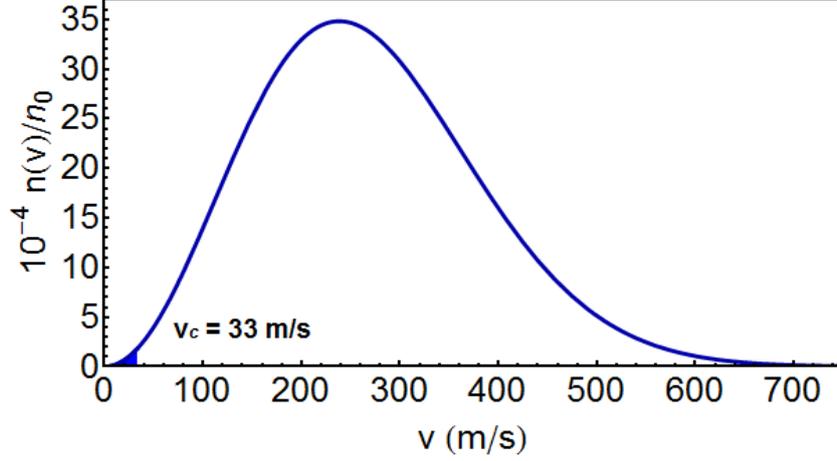
Figure 3.9: Maxwell-Boltzmann distribution of Rb vapour in room temperature of 293 K. Atoms with velocity less than the MOT capture velocity are indicated in the shaded region.

determined by

$$L = \pi r^2 \int_0^{v_c} v n(v) dv, \tag{3.6}$$

where $n(v)$ is the Maxwell-Boltzmann speed distribution of the thermal background Rb vapour of mass, m and temperature, T and it can be expressed as,

$$n(v) = n_0 4\pi v^2 \left(\frac{m}{2\pi k_B T} \right)^{3/2} e^{-\frac{mv^2}{2k_B T}}, \tag{3.7}$$

where n_0 is the atomic density.

The loading rate increases rapidly with the capture velocity v_c, which itself depends on the size of the trap. v_c of an atom can be calculated as the velocity of the atom which is stopped in a distance, r by a force equal to the half the maximum scattering force [48] and is given as

$$v_c = \sqrt{\frac{2}{m} \left(\frac{1}{2} \frac{\hbar k \Gamma}{2} \right) r}, \tag{3.8}$$

where k is the wave number, and Γ is the natural line width of Rb cooling transition. Here, r is taken as twice of rms size of the laser beam. For $r = 5$ mm of ^{85}Rb MOT, v_c is 33 m/s. Assuming a thermal background of Rb vapour at 293 K, the fraction of atoms captured is about 0.2%.
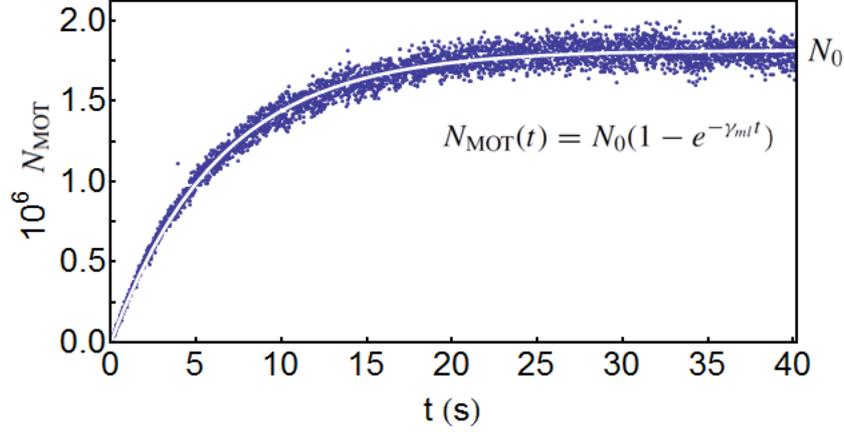
Figure 3.10: Loading of atoms in the MOT: Number of atoms in the MOT is measured by a photo-multiplier tube using spatial filtering technique, discussed in detail in Section 3.1.4. N_0 is measured to be 1.738×10^6 atoms, from which we derive $L = 2.732 \times 10^5$ atoms/s and $\gamma_{ml} = 0.157$ s^{-1}

Loading and loss rates of MOT

The total number of atoms in the MOT (N_{MOT}) at any given time, is $N_{MOT} = N_g + N_e$, where N_g and N_e are the atom numbers in the ground and excited states respectively. The time dependence of N_{MOT} can be written as

$$\frac{dN_{MOT}}{dt} = L - \gamma_{ml} N_{MOT} - \gamma_{intra} \int n^2(r) d^3r, \tag{3.9}$$

with L, the loading rate of the atoms from the background vapour into the MOT and γ_{ml}, the loss rate of the MOT atoms, due to collision with background vapour, the trap loss due to collisions between two trapped atoms, γ_{intra} and $n(r)$ is the density of atoms in the MOT [49]. The density of γ_{ml} and γ_{intra} are determined by fitting the number of trapped atoms as a function of time [50]. For a dilute density of atoms in the MOT, the last term in the Eq. 3.9 can be ignored. The time dependent solution of Eq. (3.9) with initial condition $N_{MOT}(0) = 0$ is

$$N_{MOT}(t) = N_0(1 - e^{-\gamma_{ml}t}), \quad N_0 = \frac{L}{\gamma_{ml}}. \tag{3.10}$$

where N_0 is the steady state atom number in the MOT, in the limit of large time.

The loading curve in Fig 3.10 shows a typical MOT fluorescence measurement when

atoms are loaded. $N_0 = 1.738 \times 10^6$ atoms corresponds to $L = 2.732 \times 10^5$ atoms/s and $\gamma_{ml} = 0.157 \text{ s}^{-1}$.

Sources of atoms

The Rubidium getter (SAES:Rb /NF / 4.8 / 17FT10+10) emits atom vapour in the chamber when a few Ampere of current passes through it. The MOT can be loaded in two ways; i) the background vapour directly emitted by the Rb getter or from the walls of the vacuum chamber by light induced atomic desorption (LIAD) using a blue LED (Thorlabs: MRMLED). Fig 3.10 illustrates the Rb atom loading to the MOT by Rb getter source. Since the central wavelength of blue LED is 456.5 nm and full width at half maximum of its spectrum is about 22 nm, it cannot directly ionize Rb atoms as the photon energy of the blue light is significantly below the ionization threshold and desorbs the atoms from the chamber wall, resulting in an instantaneous increase in Rb vapour pressure at room temperature so that atom loading of the MOT increases. As soon as the LED is switched off the vacuum recovers to the ambient value. So when loading with the LED the ambient vacuum is much better than when firing the dispenser. In both cases, number of atoms loaded into the MOT can be adjusted by intensity of blue light and current passing through the getter respectively. But for the getter loading, the loading rate of the MOT is larger than that of blue light, giving a higher number of atoms loaded into the MOT. Interestingly, if the getter current is too high, then the size of the atom in the MOT reduces because γ_{ml} increases. This also illustrates that the principle loss channel for atoms in the MOT is due to background gas collisions.

3.1.4 MOT Diagnostics

Laser-cooled atoms scatter photons in 4π steradians. We employ the spatial filtering setup to pick light only from the laser-cooled atoms and eliminate random scattered light in the background. In the setup, fluorescence of laser-cooled atoms is continuously monitored by a charge-coupled device (CCD) camera (Thorlabs:DC210) to track
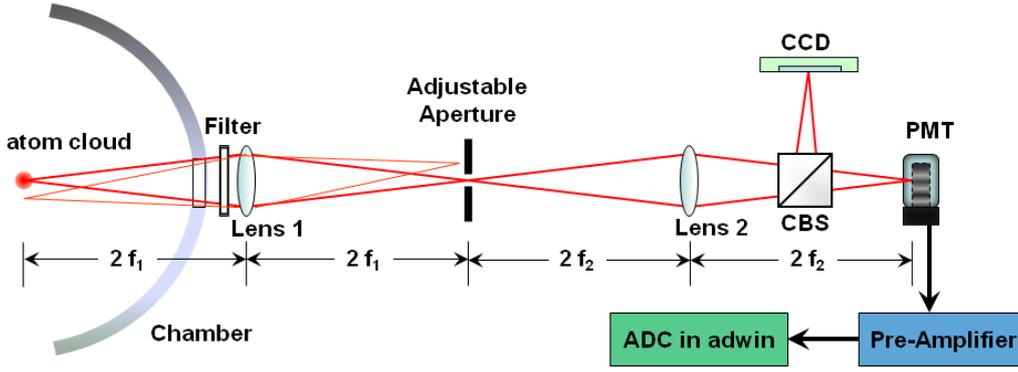
Figure 3.11: Spatial filtering set up: An illustration of the spatial filtering and imaging of the fluorescence from the MOT onto a PMT and CCD.

the position of the atom cloud, and its power is measured using a low-light detector such as a photomultiplier tube (Hamamatsu Photonics: R636−10). Spatial filtering setup in Fig. 3.11 provides an *in situ* measurement of atom number and determines the number of atoms in the MOT and its density distribution from the MOT.

Atom number and density

Considering the effect of radiative damping from Eq. 3.1, the total power scattered, P over a solid angle of 4π by N atoms in counter-propagating $\sigma^+ - \sigma^-$ beams is

$$P = N\left(\frac{\Gamma}{2}\right)\frac{(I/I_{sat})\hbar\omega}{1 + I/I_{sat} + 4(\delta/\Gamma)^2} \tag{3.11}$$

where $I_{sat} = 33.38 W/m^2$ for the ^{85}Rb $\left|5^2S_{\frac{1}{2}}, F = 3\right\rangle \rightarrow \left|5^2P_{\frac{3}{2}}, F' = 4\right\rangle$ cooling transition. Atomic fluorescence from the MOT goes through view port, filter and two lenses before reaching to PMT. Its power measured in PMT is 4.8 nW, corresponding to $\approx 2 \times 10^6$ atoms, when total power of cooling laser is 24 mW and detuning $\delta = 2\pi \times 15$ MHz. The atomic density is obtained from the fluorescence image in Fig 3.12 (a). The data is fitted to the Gaussian distribution of the form,

$$n(x, y, z) = \frac{N}{(\sqrt{2})^3\sigma_x\sigma_y\sigma_z}e^{-\left(\frac{x^2}{2\sigma_x^2} + \frac{y^2}{2\sigma_y^2} + \frac{z^2}{2\sigma_z^2}\right)}, \tag{3.12}$$

where $n_0 = \frac{N}{(\sqrt{2})^3\sigma_x\sigma_y\sigma_z}$ is the peak atomic density of the distribution. From fit of the image data to the 2 D Gaussian distribution, we determine $\sigma_x = \sigma_y \approx 0.35$ mm. Assuming
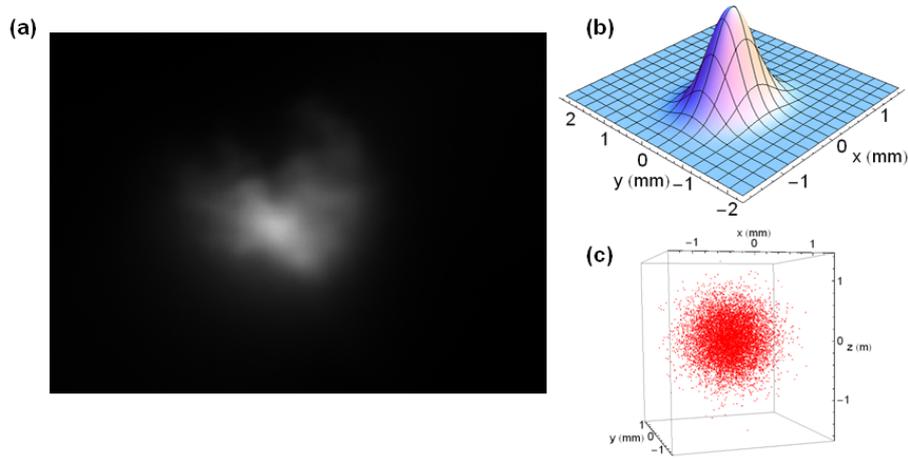
Figure 3.12: Density profile of Rb atoms in the MOT: (a) illustrates an image of the fluorescence from atom cloud in the MOT, captured on a CCD camera in the spatial filtering setup. Data from the captured image in (a) is fitted to a Gaussian distribution. The spatial profile of the atom cloud is shown in (b). The rms size of the atom cloud is found to be ≈ 0.35 mm. (c) shows simulated atom cloud of Gaussian distribution with $\sigma = 0.35$ mm.

a spherically symmetric density profile for the MOT, the peak density is calculated as $n_0 = 16.5 \times 10^9$ cm^{-3}.

Temperature measurement

The temperature of the atoms can be measured by various methods like release and recapture, trap oscillations and time of flight imaging in order of increasing accuracy. We choose the trap oscillations method which involves the oscillation of the trap centre at different frequencies in order to determine the resonant frequency. The principle of this method is described in detail in Ref [51]. We discuss it briefly here. The MOT, like any trap has a characteristic frequency of its own. The atom cloud trapped in the MOT acts like a heavily damped harmonic oscillator. From the virial theorem for an ensemble of non-interacting particles in a harmonic potential, the average kinetic energy in the trap is equal to the average potential energy. This can be written as

$$\kappa_{MOT}\langle x_i^2 \rangle = m_A \langle v_i^2 \rangle \sim k_B T \tag{3.13}$$
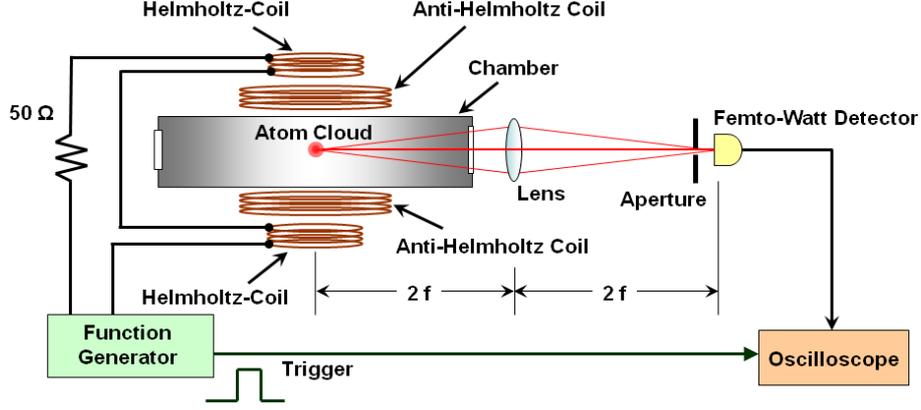
Figure 3.13: Experimental set up for MOT temperature measurement: An illustration of the spatial filtering and imaging of the fluorescence from the MOT onto a femto-watt detector.

where κ_{MOT} is the spring constant of the trap, x_i is the position variable, v_i is the corresponding velocity variable, m_A is the mass of the atom, k_B is the Boltzmann constant and T is the temperature of the atom ensemble. If ω_0 is the natural frequency of the trap, the spring constant is given by $\kappa_{MOT} = m_A\omega_0^2$. So by determining the natural frequency of the trap, we can estimate the temperature of the atom cloud. To measure the mechanical constants of a MOT, we apply an external periodic force to atoms in the MOT. This is basically a damped forced harmonic oscillator of the form,

$$\ddot{x}_i + 2p\dot{x}_i + \omega_0^2 x_i = \frac{F_0}{m_A}cos(\omega t), \tag{3.14}$$

where $p = c/2m_A$, c is a damping constant, F_0 is the amplitude of external periodic force. The external periodic force is introduced by a pair of Helmholtz coils. From solutions of the above equation, we have amplitude $a(\omega)$ and phase $\phi_{ph}(\omega)$ as a function of ω expressed as,

$$a(\omega) = \frac{\omega_0}{\sqrt{(2\omega p)^2 + (\omega_0^2 - \omega^2)^2}}, \tag{3.15}$$

$$\phi_{ph}(\omega) = \frac{2\omega p}{\omega_0^2 - \omega^2}. \tag{3.16}$$

The schematic diagram of the setup to measure the trap frequency is shown in Fig. 3.13. The MOT is loaded till saturation. An additional pair of Helmholtz coils with ten turns each are symmetrically placed about the anti-Helmholtz MOT coils. These produce a
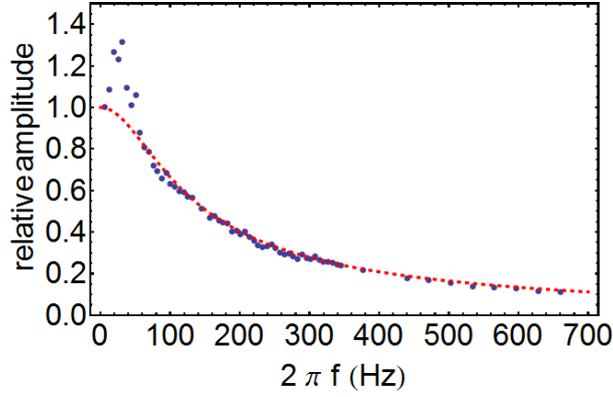
Figure 3.14: The frequency response of the relative amplitude of the atom cloud motion is illustrated when subjected to a sinusoidal perturbation. A red dashed line is a fit using Eq. 3.15 yielding $\kappa_{MOT} = 1.695 \times 10^{-20}$ kg/s^2 and $c = 2m_A p = 2.027 \times 10^{-22}$ kg/s.
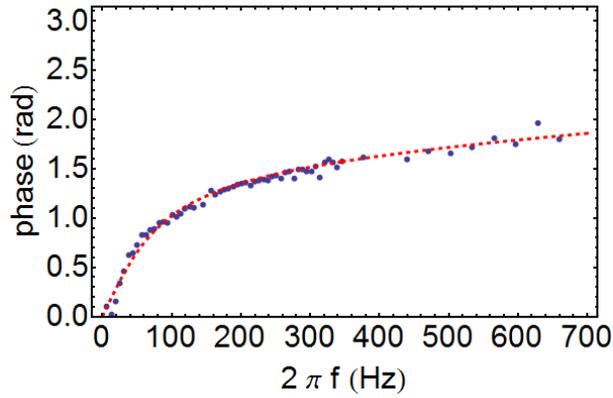
Figure 3.15: Figure illustrates the frequency response of the phase of the atom cloud motion when subjected to a sinusoidal perturbation which is fitted to Eq. 3.16. The fit yields $\kappa_{MOT} = 1.695 \times 10^{-20}$ kg/s^2 and $c = 2m_A p = 2.541 \times 10^{-22}$ kg/s.

small uniform magnetic field which shifts the position of the centre of the quadrupole magnetic field and hence the position of the MOT. Now the Helmholtz coils are fed in series with a sinusoidal current of frequency, f with a small amplitude. A resistor of 50 Ω is connected in series with the Helmholtz coil to avoid the voltage drop due to change in frequency, f. The oscillating atom cloud is imaged by a single lens onto a femto-watt detector (Newport: 2151) mounted on a translation stage. The output of the detector is viewed on an oscilloscope along with the original excitation sinusoid such that their relative phase relation is also recorded. The position of the detector is adjusted to maximize the amplitude, and visibility of the response is sinusoid. The oscilloscope is operated in average mode to cancel out the random noise and amplitude fluctuations. The waveforms are recorded on a hard disk for different excitation frequencies and analyzed after the full experiment. The amplitude and phase response obtained as a function of varying excitation frequency is shown in Fig. 3.14 and Fig 3.15. The resonance is highly broadened because of the high damping in the trap. In Fig. 3.14 and Fig. 3.15, the frequency at which the phase response crosses the value $\pi/2$ is $2\pi \times 55$ Hz. The temperature of the atoms estimated by this method using Eq. 3.13 is $T = 166(\pm 28)\mu$K.

3.2 The ion trap

The ion trap is designed to trap positively charged ions like Rb^+,K^+, Cs^+ and Ca^+ ions and their molecular ions. A detail of the design of the ion trap can be found in the thesis of Ravi Krishnamurthy [43]. Here we briefly describe the essential features which relate to the experiments performed for the present thesis. As mentioned in the previous sections on the MOT, it requires cooling and repumping lasers with the quadrupole magnetic field minima at the centre using a pair of anti-Helmholtz coils. The presence of any other strong magnetic field would shift minima of the MOT, resulting in compromising the operation of the MOT. This fact rules out the use of a Penning trap, which requires a very strong magnetic field. Another significant disadvantage of com-

bining a Penning trap with the MOT is the limited optical access for laser beams. Paul trap configuration is another widely used for ion trapping, employing time−varying and static electric fields. Among various Paul trap designs, a linear Paul trap satisfies our purpose and requirements. We modified this conventional linear Paul trap design to suit our geometric constraints, so that laser beams of 1 cm diameter for the MOT can be accommodated, as illustrated in Fig 3.8. In the following sections, we discuss ion trap potential, implementations and characterization in detail.

3.2.1 Ion trapping potential

A linear Paul trap consists of four parallel quadrupole electrodes with a radio-frequency (RF) applied for radial confinement, and two endcap electrodes with DC voltage for axial confinement. The potentials of a linear Paul trap, which has combination of an oscillating electric potential, ϕ_{radial} and static d.c. potential, ϕ_{axial}, are given below [37],

$$\phi_{radial}(x, y, t) = (U_{dc} + V_{rf} \cos \Omega t) \frac{x^2 - y^2}{2R^2}, \tag{3.17}$$

where R is the radial distance from the centre of the trap to the quadrupolar electrode, V_{RF} is the amplitude of the radio frequency(rf) voltage, $\Omega = 2\pi\nu_{rf}$, RF frequency applied and U_{dc} is a DC offset for the RF voltage in the quadrupole rods, and

$$\phi_{axial}(x, y, z) = \frac{KU_{endcap}}{D^2} \left(z^2 - \frac{x^2 + y^2}{2} \right) \tag{3.18}$$

where D is the distance from the axial trap centre to the endcap electrodes and K is a geometric factor, which accounts phenomenologically for the complicated geometry and can be determined experimentally. The equations of motion of an ion of mass M and charge Q in this potential is expressed as follows,

$$
\begin{aligned}
\frac{d^2 x}{dt^2} &= -\frac{Q}{M} \left(\frac{U_{dc} + V_{rf} \cos \Omega t}{R^2} - \frac{kU_{endcap}}{D^2} \right) x, \\
\frac{d^2 y}{dt^2} &= -\frac{Q}{M} \left(\frac{-U_{dc} - V_{rf} \cos \Omega t}{R^2} - \frac{kU_{endcap}}{D^2} \right) y.
\end{aligned}
$$

$$\tag{3.19}$$
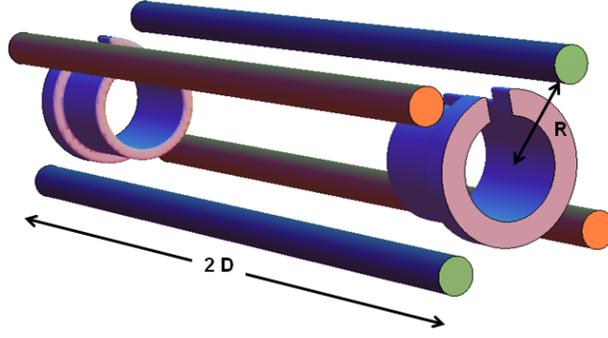
Figure 3.16: The SIMION 7 rendering of the ion trap geometry is shown. Four long parallel rods are arranged in a quadrupole configuration. Endcap ring electrodes are along the axial direction.

The equations of motion can be arranged in the homogeneous Mathieu equation of the form,

$$\frac{d^2u}{d\tau^2} + (a_u - 2q_u \cos 2\tau)u = 0, \tag{3.20}$$

where $u = x, y, z$ and $\tau = \frac{\Omega t}{2}$.

By making the substitutions, we obtain modified stability parameters for a linear Paul trap:

$$
\begin{aligned}
\tilde{a}_x &= \frac{4QU_{dc}}{MR^2\Omega^2} - \frac{4Q\zeta U_{endcap}}{MR^2\Omega^2}, \quad \tilde{a}_y = -\frac{4QU_{dc}}{MR^2\Omega^2} - \frac{4Q\zeta U_{endcap}}{MR^2\Omega^2}, \\
\tilde{a}_z &= \frac{8QKU_{endcap}}{MD^2\Omega^2}, \quad q_x = -q_y = \frac{2QV_{rf}}{M\Omega^2 R^2}, \quad \zeta = \frac{KR^2}{D^2}
\end{aligned}
$$

$$\tag{3.21}$$

The Mathieu equations give the stability and instability of the solutions, depending on the above stability parameters, $\tilde{a}$ and q.

3.2.2 Modified linear Paul trap

We modify the ion trap geometry to accommodate laser beams for the MOT. Given six MOT laser beam of 10 mm along the Cartesian axes, the basic challenge is in the design of the ion trap. That leads to reduction in diameter of the quadrupole electrodes and further separation between the quadrupole rods. Even the endcaps are constructed
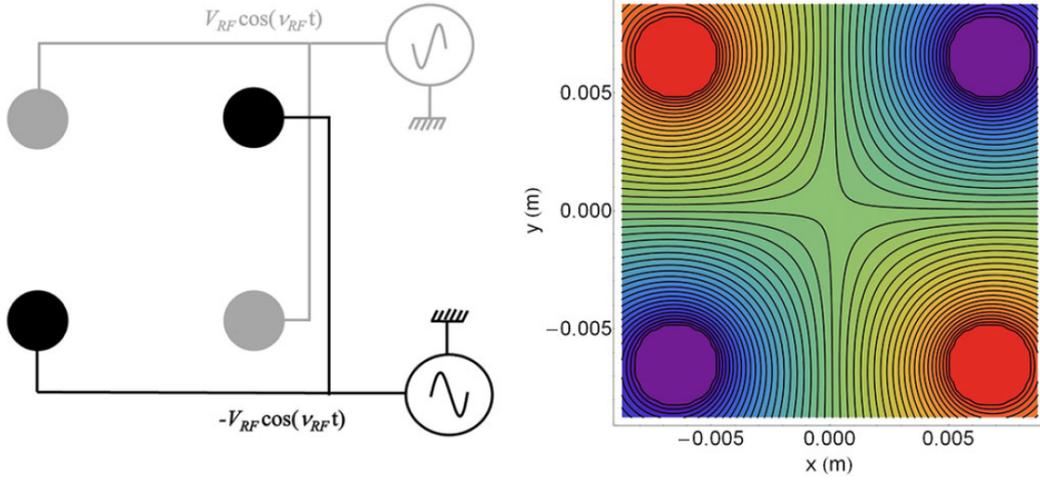
Figure 3.17: The cross section of the ion trap with the biasing diagram is illustrated. For a given instant of time, the resultant potential surface is plotted.

further apart, resulting in non-ideal quadrupole potential, shown in Fig. 3.16. A time-varying radio-frequency (RF) voltage, V_{rf} is applied to one diagonal set and an opposite phase RF voltage is applied to the complementary diagonal set. The transverse cross section of the ion trap, the RF bias diagram, and the potential surface at a given instant of time are illustrated in Fig. 3.17. For such a potential, an approximate analytical form for the field configuration in the central region of the ion trap is given by

$$\phi_{mod}(x,y,z,t) \approx \frac{V_{rf}}{2R^2}(x^2 - y^2)cos(\Omega t) + \frac{KU_{endcap}}{D^2}(z^2 - \frac{x^2 + y^2}{2}).$$ (3.22)

A fit of the above analytical potential to the SIMION generated potential obtains $R = 5$ mm, instead of 7.69 mm, the actual separation from centre to the surface of the quadrupole rods. With $D = 25.5$ mm, the geometric factor is calculated as $K \approx 0.103$.

Since the ions are trapped dynamically, along with the frequency of the micromotion, which is a result of forced oscillation tied to the applied RF field, a slower, orbital macromotion manifests for the trapped ions. This is also called as the secular motion of the ions. According to the solution of the Mathieu equation, secular motion frequencies are related to the stability parameters by,

$$\omega_{u,n} = (n + \frac{\beta_u}{2})\Omega$$ (3.23)

42

where $u = x, y, z$ and $n = 0, 1, 2 \cdots$, and β_u is a function of a_u, q_u. For the adiabatic approximation, *i.e.* for $|a_u, q_u| \ll 1$, β can be approximated by

$$\beta_u^2 \approx a_u + \frac{q_u^2}{2}. \tag{3.24}$$

Therefore, we get the fundamental ($n = 0$) secular motion frequencies:

$$
\begin{aligned}
\tilde{\omega}_x &= \frac{\Omega}{2}\tilde{\beta}_x \approx \frac{\Omega}{2}\sqrt{\frac{q^2}{2} + a_x - \frac{\tilde{a}_z}{2}}, \\
\tilde{\omega}_y &= \frac{\Omega}{2}\tilde{\beta}_y \approx \frac{\Omega}{2}\sqrt{\frac{q^2}{2} + a_y - \frac{\tilde{a}_z}{2}}, \\
\tilde{\omega}_z &= \frac{\Omega}{2}\sqrt{\tilde{a}_z}.
\end{aligned}
\tag{3.25}
$$

For the operating point of $V_{rf} = 91.7$ V, $\Omega = 2\pi\,600$ kHz and $U_{endcap} = 80$ V, we find that the radial macromotion frequency is $\omega_x/2\pi = \omega_y/2\pi = 135$ kHz and the axial frequency is $\omega_z/2\pi = 27$ kHz.

3.2.3 Non linearity of the ion trap

The trapping potential contains higher order anharmonic terms. Deviations of the trap potential from the quadrupolar form can be described by a series expansion in cylindrical coordinates, *i.e.*

$$\phi_{real}(r, \phi, t) = U(t) \sum_{n}^{\infty} c_n \left(\frac{r}{R}\right)^2 cos(n(\phi - \epsilon_n)), \tag{3.26}$$

where c_n is the amplitude of the potential contribution. $n = 2$ corresponds to quadrupole potential. Due to rotational symmetry, the odd coefficients, c_n vanish. Eq. 3.26 is fitted to the central region of the SIMION generated potential for two cases: $V_x = V(x, y = 0, t = 0)$ and $V_y = V(x = 0, y, t = 0)$, illustrated in Fig. 3.18. From the fit, we obtain the following values for the coefficients, c_n, normalized to $c_2 = 1$, $c_4 = 0.00263$ and all other higher terms are negligible. These higher terms in the trapping potential contribute to instabilities in the trapping of the ions as a function of the trap parameters and can be seen in stability diagram as demonstrated in [37].
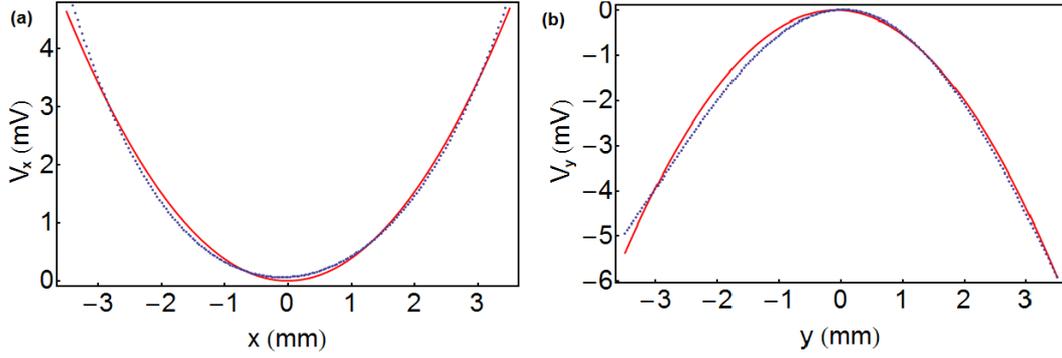
Figure 3.18: A fit of Eq. 3.26 to the central portion of the SIMION generated potential is illustrated. (a) plots $V_x = V(x, y = 0, t = 0)$ and (b) plots $V_y = V(x = 0, y, t = 0)$.
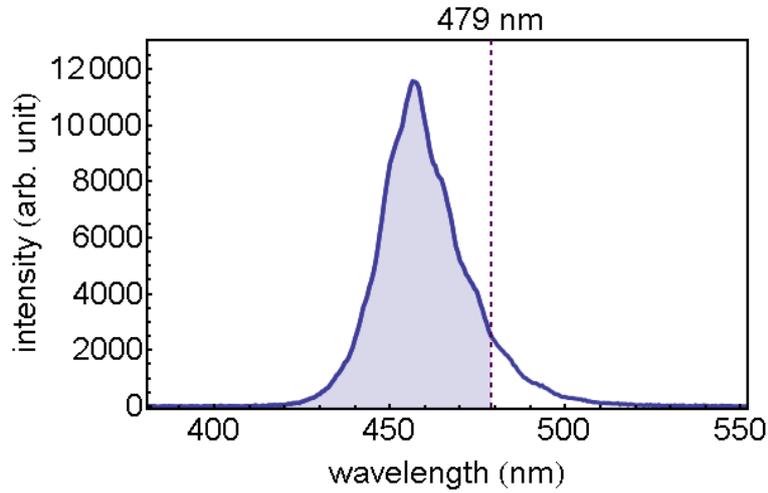
Figure 3.19: Spectral profile of BLS: The central wavelength of the BLS is at 456 nm and its FWHM = 22 nm. Atoms require energy corresponding to 479 nm to get into ionization continuum. More than 90 % of the BLS spectrum participates in photo−ionization

3.2.4 Loading the ion trap

The ionization energy required to eject one electron from a Rb atom is 4.177 eV. We employ two−photon ionization (TPI) to load ^{85}Rb$^+$ ions into the ion trap. There are two different methods; resonant TPI and non-resonant TPI, described below.

Resonant TPI

The two photons for ionization are from the cooling laser of the MOT (1.59 eV, 780 nm) and the blue light source (BLS) LED (peak at 2.72 eV, 456 nm). The sum of the energies
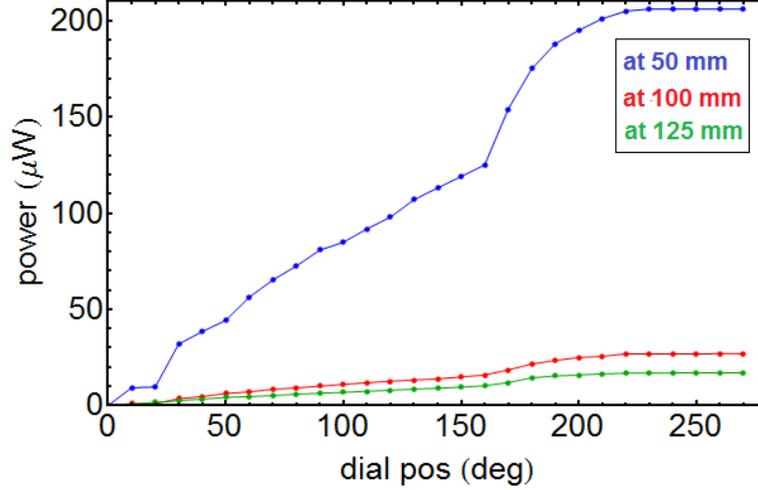
Figure 3.20: Intensity of BLS as a function of dial position: Intensity of BLS is measured at various distances, 50, 100 and 125 mm from the BLS.

carried by the red and the blue light is 4.31 eV, which is higher than the ionization energy for the Rb atom. Spectral profile of BLS is illustrated in Fig. 3.19. As the cooling laser are on resonance with the ^{85}Rb D$_2$ atomic transition, this is termed as resonant TPI. The corresponding ionization process is

$$Rb + h\nu_{780} + h\nu_{456} \rightarrow Rb^+ + e^- + K.E. \tag{3.27}$$
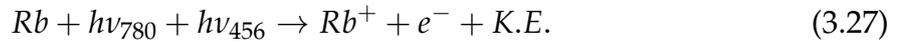
and thus the ion is created with almost zero velocity at the potential minimum of the ion trap. For a given intensity of the BLS, this method gives a steady loading rate of ions in the ion trap from the cold atoms in the MOT. Intensity of BLS as a function of dial position is plotted in Fig. 3.20 for the calibration purpose. The loading rate of ions will be discussed quantitatively in the next chapter.

Non resonant TPI

A frequency-doubled Nd:YAG laser at 532 nm (pulse width ≈10 nm and pulse energy ≈165 mJ/pulse) is focused onto the MOT centre to ionize Rb atoms. The Nd:YAG beam can ionize the residual vapor in the trap volume that overlaps with the pulse. The ionization process is

$$Rb + 2^{(+)} \times h\nu_{532} \rightarrow Rb^+ + e^- + K.E., \tag{3.28}$$
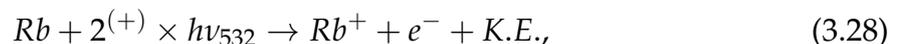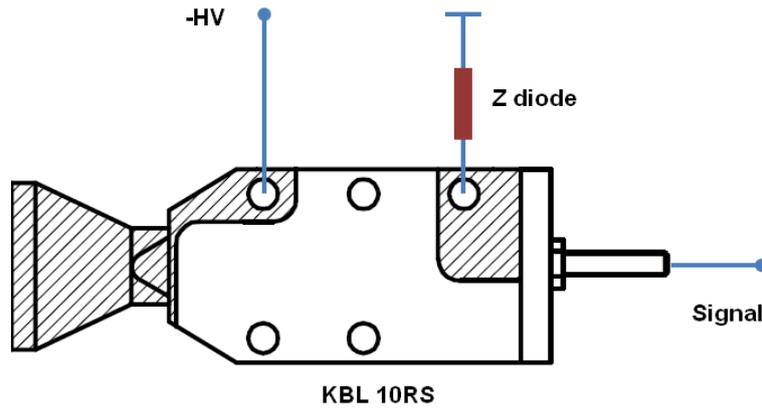
Figure 3.21: CEM connection: Zener diode is used for creating a stable voltage difference about 100 V between the CEM output and the anode. The diagram is taken from sjuts.com.

where '+', the superscript on '2' indicates that more than two photons can participate in the ionization process. 532 nm corresponds to 2.33 eV of energy, so two photons at 532 nm are sufficient to ionize a Rb atom. With the getter ON, this method can ionize directly from the background vapour.

Operation of the ion trap

The time−varying RF signal from a function generator (Agilent: 332204) is fed to a wide−band power amplifier (Krohn-Hite: 7602M), which generates the two 180° out of phase waveforms of equal amplitude, contacted to the respective diagonals of the trap. The function generator is operated in the burst mode once it receives a trigger pulse from a real time operating system module (Keithley: CPUT10) loaded into a control rack (Keithley: ADWin Pro). This allows the RF signal to be switched ON or OFF within a fraction of the RF cycle. For the axial confinement of Rb^+ ions, a positive voltage on the endcap electrodes. The typical operating parameters for the trap are 400 kHz$\leq \nu_{rf} \leq$600 kHz and 0 V$< V_{rf} \leq$ 200 V, limited by the gain−bandwidth product of the RF amplifier, 0 V$< U_{endcap} \leq$ 80 V.

Detection of ions

Due to the high energy photons required to excite closed shell Rb^+ ion, optical detection of the ions is not undertaken. Only the destructive detection of the ions is implemented, using a channel electron multiplier (CEM). The CEM (Dr. Sjuts: KBL 10RS) is installed along the z direction, illustrated in the viewport **b** in Fig. 3.8. The CEM funnel is held at -2400 V for positive ion detection with the tail of the CEM held at ground potential, shown in Fig. 3.21. A Z-diode is used to create a stable voltage difference of 100 V between the CEM output and the anode. The ions are extracted onto the CEM by switching the voltage from 80 V to -5 V on the endcap electrodes near to the CEM, while keeping the opposite endcap at 80 V and the quadrupole rods operational. When extracted, the time of flight for the Rb^+ ions is $\approx 47 \mu s$ and, the ion signal is spread between $40-60 \; \mu s$. The ions are detected by the CEM in two modes of operation, the pulse counting mode (direct) and the analog mode (through a preamplifier).

For pulse counting detection, the trapped ion cloud is extracted on the CEM, resulting an 8 ns negative pulse for every ion detected. From the experiment, we found that $\approx 300 \pm 30$ counts/$10 \; \mu s$ is the limit of ions that can be counted without pile-up of ion signal. The pile-up prevents the proportional detection of ions.

For the analog mode detection, the CEM signal is fed to a low-noise preamplifier (Hamamatsu: C7319) with set amplification, and the output of the preamplifier is recorded on a digital oscilloscope. This gives a positive integrated voltage waveform due to an inverted output of the preamplifier. The pulse counting and analog modes for ion detection are extensively calibrated against one another to determine the proportionality constant in the previous studies by Ravi *et al* in [52]. After extensive characterization of the equivalence of the pulse counting and analog mode, we use the analog mode for the ion detection in the experiment.

Extraction potential

Ions created at the centre are extracted at an electric field magnitude of $|\mathbf{E}_1| \approx 1700$ V/m travel 25.5 mm to the endcap electrode, then to the CEM held at $V_{CEM} = -2400$
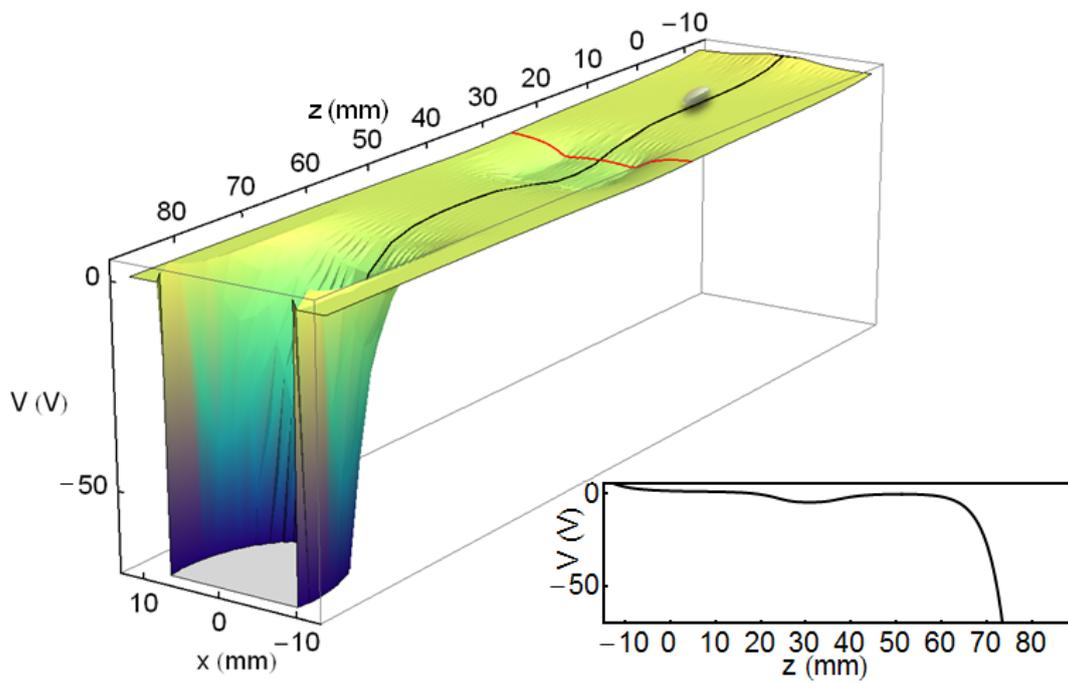
Figure 3.22: Electric potential along z direction: This potential is calculated for the CEM held at $V_{CEM} = -2400$ V, one of the endcap electrodes near to the CEM at -5 V and opposite one at 80 V. A red line indicates the position of the extracting endcap electrode at -5 V. Ion cloud (not in scale) is drawn at the trap potential centre. The CEM is placed (not in the picture) at z = 87 mm. A black line shows the potential along z direction, which is separately plotted in the inset.

V, providing further acceleration due to an electric field magnitude of $|\mathbf{E}_2| \approx 40000$ V/m. The ions feel an acceleration $\mathbf{a}_{ion}$ expressed as,

$$\mathbf{a}_{ion} = \frac{Q\mathbf{E}_1(z)}{M}, 0 < z \leq 25.5mm \ ,$$

$$\mathbf{a}_{ion} = \frac{Q\mathbf{E}_2(z)}{M}, 25.5mm < z \leq 87mm. \qquad (3.29)$$

where Q is the charge on the ion and M is the mass. The ion trap potential is plotted as a function of x and z in Fig. 3.22.

3.3 The experimental sequence

A control rack (Keithley: ADWin Pro) controls the entire experimental sequence. This rack has a real time operating system module (Keithley: CPUT10), a an 8-bit analog to digital converter (ADC) module and an 8-bit Digital to analog converter (DAC) module wired into it. A suitable program written in ADBasic software generates required sequence of triggers and analog signals to instruments used in the experiment. Experimental data can also be saved in a computer using the ADWin module. Labview 7.1. provides a structured programming platform to integrate various instruments used in the experiments and also a convenient graphical user interface (GUI) that identifies each device as a virtual instrument (VI). The ADWin system is treated as a VI on the Labview platform and an ADBasic program is treated as an event. The experimental sequences for each experiment differ, therefore details will be described in the relevant sections. Invariant facts of all the experiments are as follows; the quadrupole magnetic field of the MOT is kept on, the cooling and repumper lasers are locked to the appropriate frequencies, BLS is used for loading ions in the ion trap and Rb dispenser for atoms in the MOT, and the extraction voltage of the ion trap is -5 V.

3.3.1 Motional resonance spectrum

Experimental determination of the secular (macro) motion frequencies is done by adding a weak monochromatic perturbation to the time-varying drive voltage of the trap. An
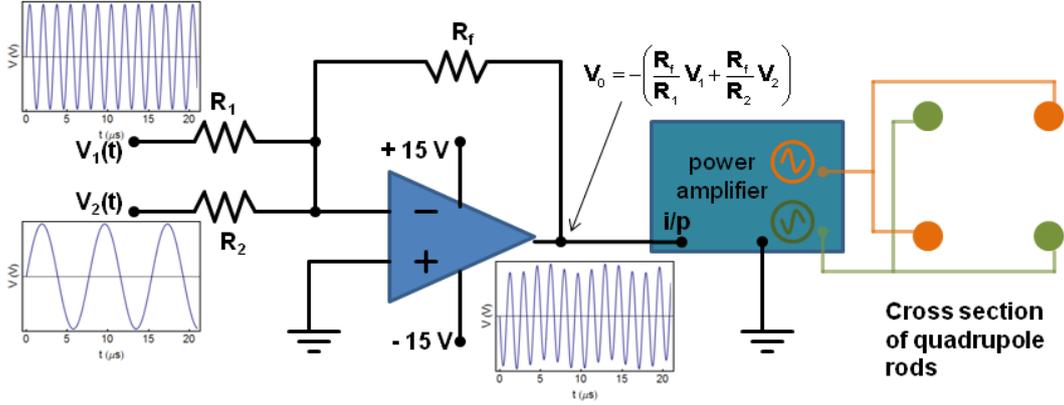
Figure 3.23: Experimental setup to add a weak excitation frequency: An Op-Amp adder circuit is used for adding two signals: RF drive voltage, V_1 and a weak excitation frequency signal, V_2. $R_1 = R_f = 4.7\,k\Omega$ and $R_2 = 47\,k\Omega$. Output signal of the adder, $V_0 = -(V_1 + \frac{1}{10}V_2)$ is fed to the power amplifier, which splits the signal into two signals with opposite phase.

Op-Amp adder circuit (AD711JN) is used for adding RF voltage and weak excitation frequency signal. Fig. 3.23 illustrates the experimental setup where the excitation frequency of $V_2(t)$ is varied while frequency of $V_1(t)$ is kept at 600 kHz. Output of the adder circuit is fed to a wide-band power amplifier with the gain of ≈ 130. Rest of the connection remains the same as described in Operation of ion trap section. When the atoms in the MOT reach its saturation level, BLS is switched on for 0.5 s to load ions in the ion trap and the excitation voltage is applied along with the RF drive voltage. At each value of the excitation frequencies, we measure the number of ions after the excitation is applied for a certain interval of time. This time interval is adjusted such that there is good visibility of the resonances but without too much broadening and saturation. Several resonances are seen at the harmonics, sub-harmonics and the natural frequencies of oscillation in x-y plane. We can infer that a resonance is radial or axial by seeing its dependence on a parameter such as V_{rf} for the radial modes and U_{endcap} for the axial mode. Since our perturbation frequency is applied radially, it is much harder to experimentally couple the excitation to the z motion. We measure the resonance spectrum for different values of U_{endcap} and observe that the prominent resonances do not change as we vary U_{endcap}. This indicates that they are not axial resonances. Due to technical constraints, we have not been able to efficiently excite

the axial resonances in our setup. From our measurement, for the operating point of $V_{rf} = 91.7$ V, $\nu_{rf} = 600$ kHz and $U_{endcap} = 80$ V, we find that the radial macromotion frequencies are $\omega_x/2\pi = 132$ kHz and $\omega_y/2\pi = 140$ kHz. The secular frequency in the x and y directions are in principle degenerate but due to small imperfections and mis-alignments in the trap geometry, they manifest as separated resonances. The nature of the resonances for different values of V_{rf} is shown in Fig. 3.24. The experimental values of the trap frequency agree very well with the analytically computed values in section 3.2.2. These agree also well with the values found by taking the Fourier transform of the numerically calculated ion trajectory for the experimental trap parameters.

3.4   Ion trap Stability regions

The trapping of the Rb^+ ion depends on the interplay of three parameters, the frequency ν_{rf}, time varying voltage amplitude V_{rf}, and the static end cap voltage, U_{endcap}. We characterize the trap by varying the value of V_{rf} for each value ν_{rf} (400, 500, 600, 800 kHz and 1 MHz) and observing the number of ions remaining in the trap after various intervals of time that ions are held in the trap. Once again, ions are created for 0.5 s from atoms in the MOT and loaded into the ion trap operating at combinations of ν_{rf}, V_{rf} and U_{endcap}. Fig. 3.27 shows the experimentally observed stability diagram at $\nu_{RF} = 400$ kHz and $U_{endcap} = 80$ V. Left side y axis shows ions detected in arbitrary units, and right side y axis indicates various intervals of time till 50 s. The ion trap operating at $\nu_{rf} = 600$ kHz and $U_{endcap} = 80$ V yields significantly larger ion numbers detected in the CEM, compared with other values of ν_{rf}, illustrated in Fig. 3.26. Due to the gain-bandwidth limit of the power amplifier, we scan V_{rf} from 0 to 140 V at $\nu_{RF} = 600$ kHz where the waveform of the drive voltage does not contain significant harmonic distortion. After keeping ions in the trap for 50 s, we take the operating parameters for which the maximum number of ions is detected. The operating point for our experiments is found as $\nu_{RF} = 600$ kHz, $V_{RF} = 91.7$ V and $U_{endcap} = 80$ V.
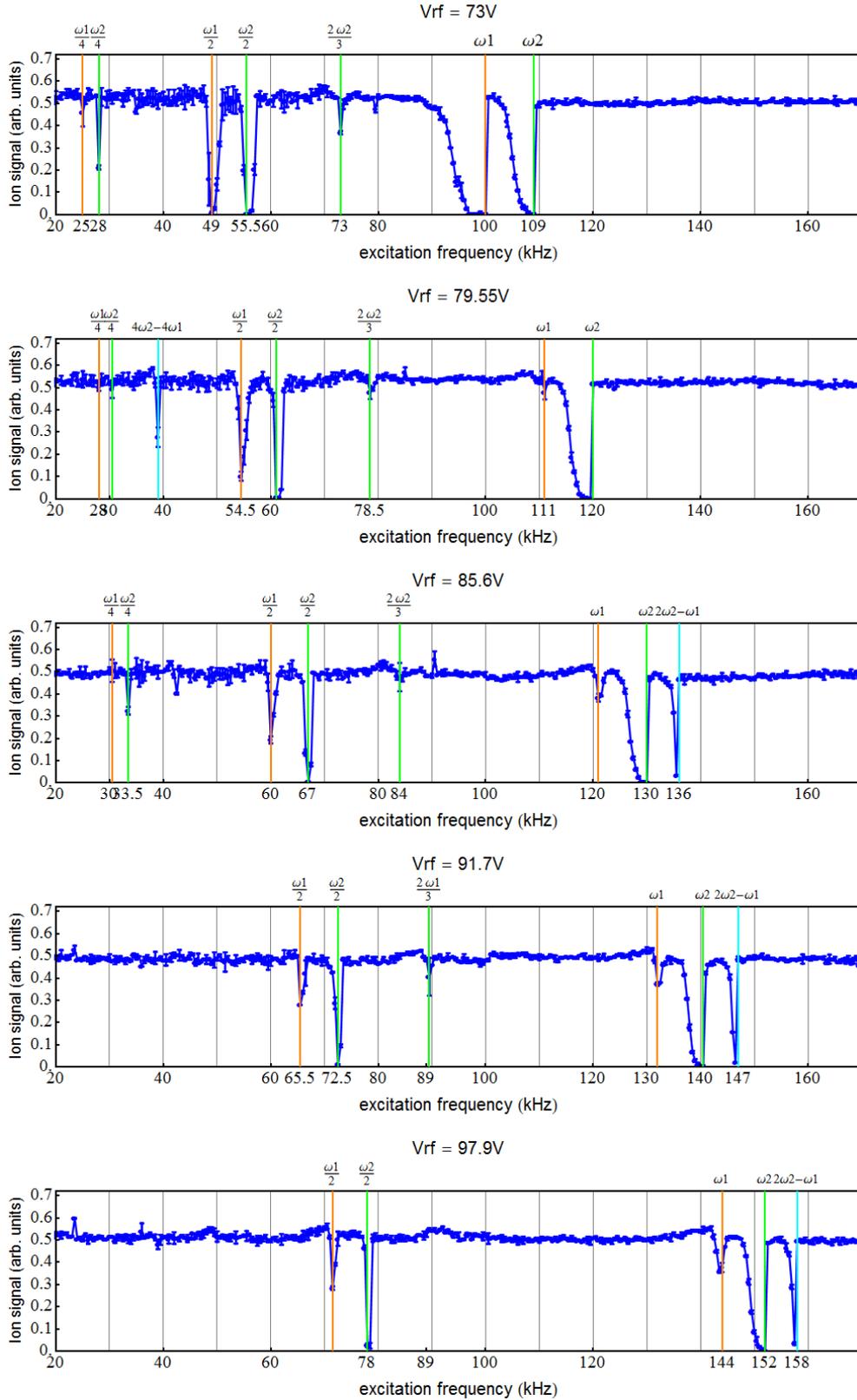
Figure 3.24: The spectra of motional resonances of a Rb$^+$ ion cloud in the trap at $V_{rf} = 73$, 79.55, 85.6, 91.7 and 97.9 V. ω_1 and ω_2 are radial resonance frequencies. Other than ω_1 and ω_2, we also observe higher harmonics of resonance frequencies.
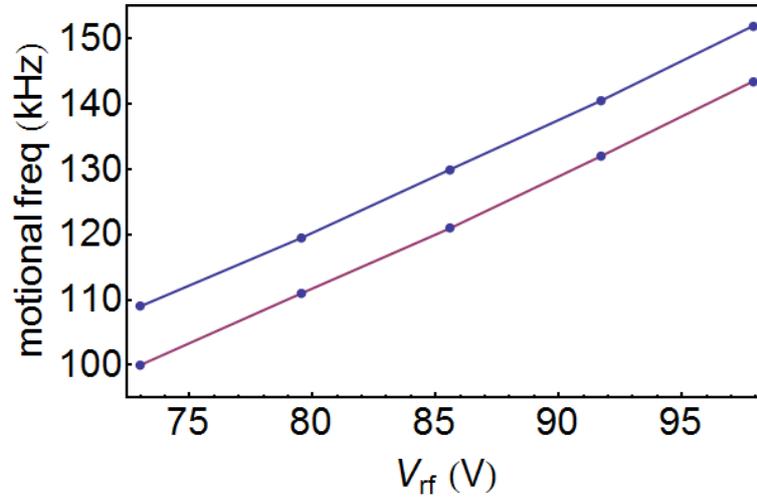
Figure 3.25: ω_1 (in red) and ω_2 (in blue) are plotted at various V_{rf} values. There is a prominent shift in resonances as V_{rf} value changes.
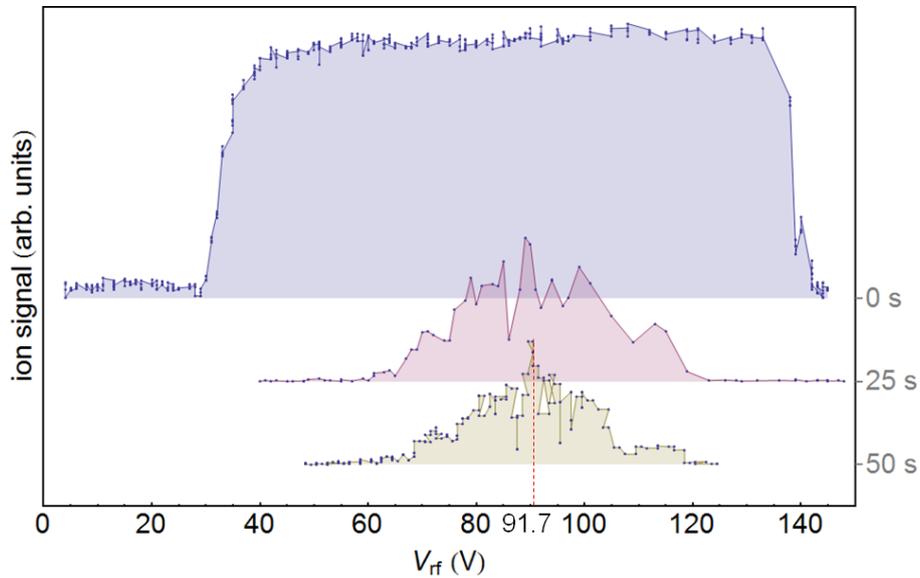
Figure 3.26: Stability region of the ions for 600 kHz scanned V_{rf} from 0 to 140 V for various holding times. Due to the gain-bandwidth limit of our RF amplifier, distortion in the drive voltage waveform starts from $V_{rf} = 95$ V. For 50 s of holding time, the value of V_{rf} for the maximum number of ions detected is 91.7 V.
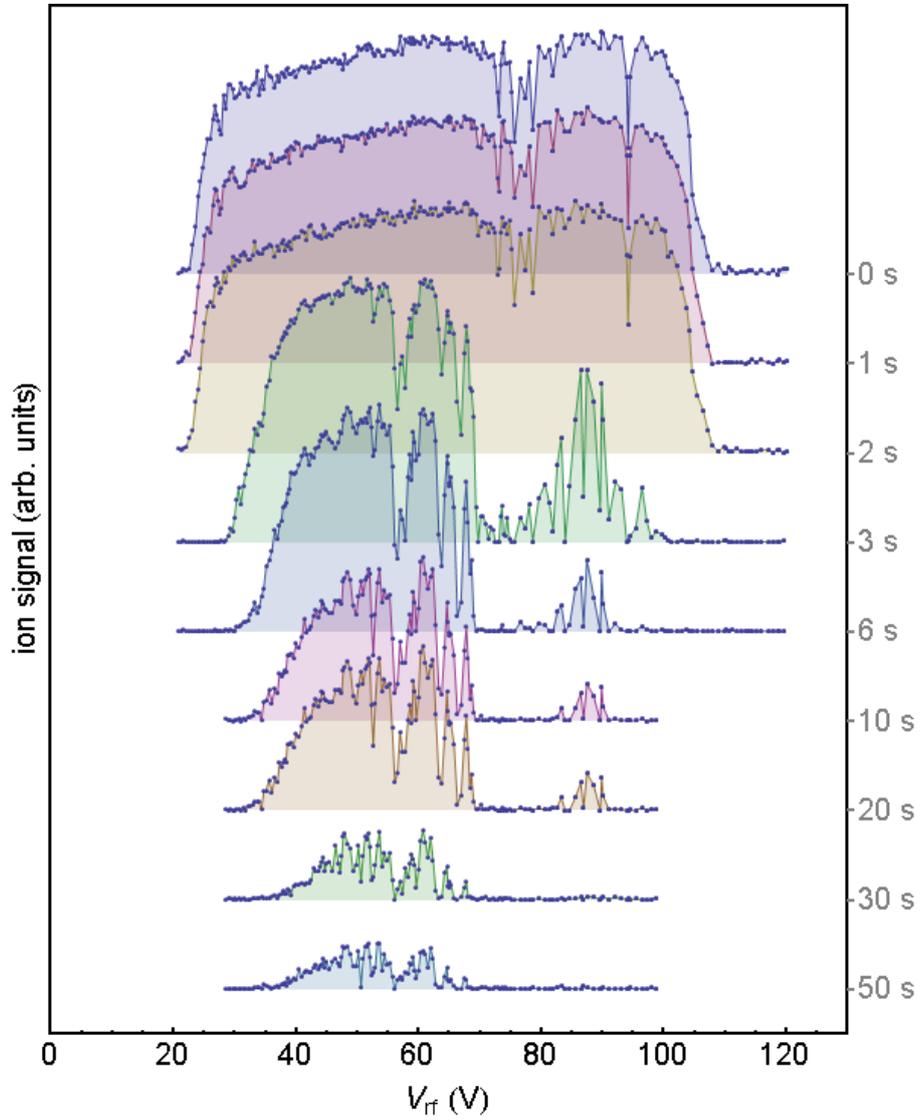
Figure 3.27: The experimentally determined stability region of the ions for 400 kHz scanned V_{rf} from 0 to 120 V for various holding times. The vertical axis is a measure of the number of ions detected after a 0.5s loading and immediate extraction.

3.5 Photoassociation

3.5.1 Background

Schrödinger's equation for a diatomic molecule

The Schrödinger equation for a diatomic molecule consists of nuclear and electronic kinetic energies T_n and T_e, potential terms, such as nuclear-nuclear V_{nn}, nuclear-electronic V_{ne} and electronic-electronic V_{ee} terms and relativistic terms V_{rel} such as spin-orbit coupling. Therefore the approximate Hamiltonian H for the diatomic molecule can be represented as,

$$H = T_n + T_e + V_{ne} + V_{nn} + V_{ee} + V_{rel}. \tag{3.30}$$

According to the Born-Oppenheimer approximation, we can separate nuclear and electronic motions, as they have significantly large difference in their masses which results in different energy and time scales for the two. The electronic wavefunction sees the nucleus in a slow motion. That makes us to neglect $T_n \to 0$ and electronic Schrödinger equation is solved for a range of fixed nuclear coordinates of R. The angular part of the electronic Schrödinger equation is separated from the radial part and expressed in terms of spherical harmonic function $Y_{ml}(\theta, \phi)$. Therefore the radial Schrödinger equation for the nuclear motion of a diatomic molecule is given by

$$\left[-\frac{\hbar^2}{2\mu}\frac{d^2}{dR^2} + V(R) + \frac{\mathbf{N}^2}{2\mu R^2} \right] \Psi = E\Psi, \tag{3.31}$$

where μ is the reduced mass, R is the internuclear separation, $V(R)$ is the radial part of the potential without having any rotation and $\mathbf{L}$ is the nuclear orbit angular momentum operator $(\mathbf{N}^2 = l(l+1)\hbar^2)$.

Angular momentum coupling

Depending upon the relative strength of nuclear rotation, electrostatic and spin-orbit couplings, the most appropriate quantum numbers and the corresponding Hund's case for the molecular states can be chosen. Hund's case c is for interactions at the
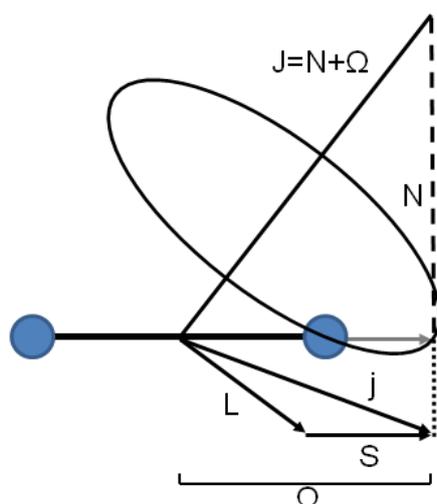
Figure 3.28: Vector coupling and projection for Hund's case c: $\mathbf{j} = \mathbf{L} + \mathbf{S}$ is coupled to the internuclear axis. The projection of $\mathbf{j}$ on the internuclear axis is Ω, which is a good quantum number in Hund's case c.

relatively large internuclear separations where photoassociation transition strength is strong. For those long bond molecules, total angular momentum $\mathbf{L}$ and spin $\mathbf{S}$ do not precess around the internuclear axis, instead coupling between $\mathbf{L}$ and $\mathbf{S}$ are stronger. $\mathbf{L}$ and $\mathbf{S}$ couple to form $\mathbf{j} = \mathbf{L} + \mathbf{S}$, then $\mathbf{j}$ precesses about the internuclear axis with Ω, the projection of $\mathbf{j}$ onto the internuclear axis, illustrated in Fig. 3.28. That makes Ω a good quantum number [53]. The convention for labeling of Hund's case c states is $\Omega_{u/g}^{\pm}$, where gerade g, ungerade u and $\pm$ for reflection symmetries are used. Potential curves for a Rb$_2$ long bond dimer is plotted for Hund case's c, shown in Fig. 3.29.

Selection rules

The selection rules for electronic transition of Hund's case c are as follows [54];

- $\Delta\Omega = 0, \pm 1$ for transitions between multiplet components.

- $+ \leftrightarrow +$ and $- \leftrightarrow -$ for reflection symmetry.

- $g \leftrightarrow u$ for gerade and ungerade.
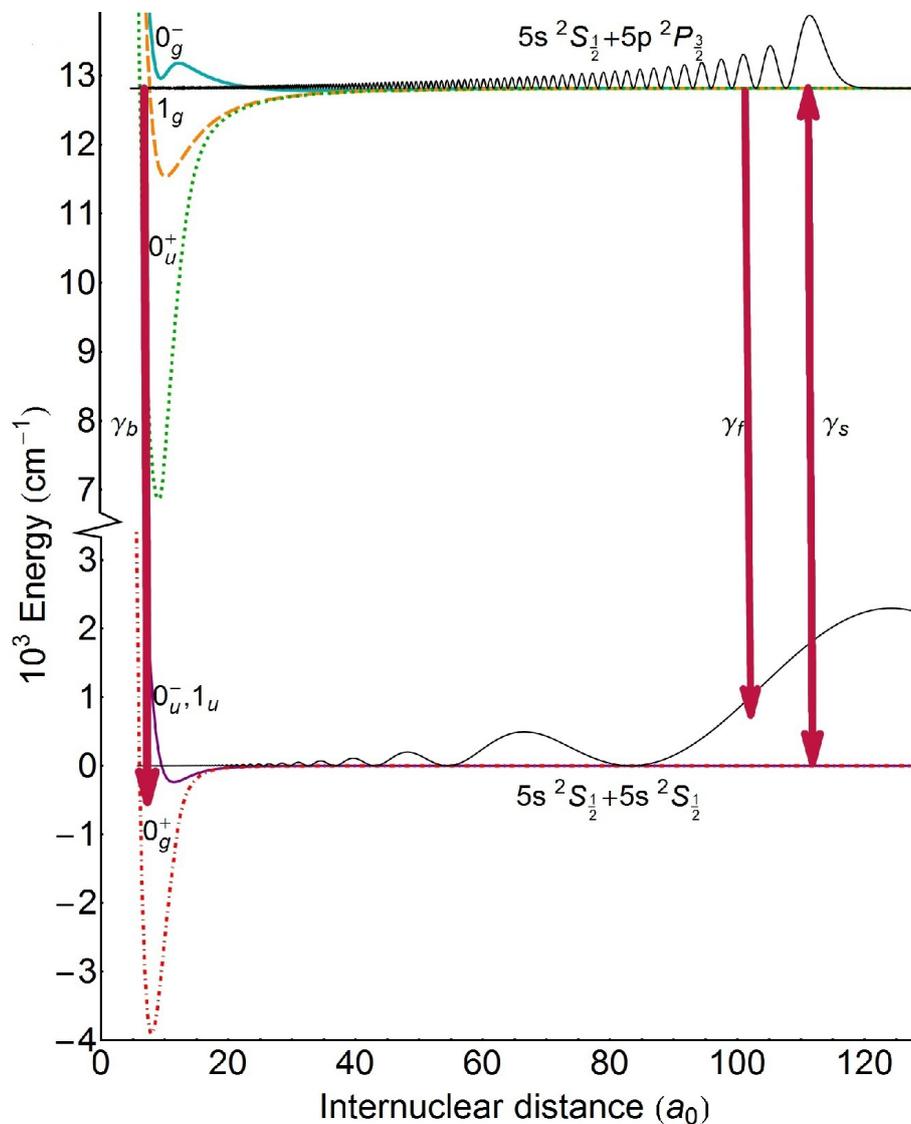
Figure 3.29: Rb_2 molecular potential curves corresponds to the $5S_{\frac{1}{2}} + 5S_{\frac{1}{2}}$ and $5S_{\frac{1}{2}} + 5P_{\frac{3}{2}}$ dissociation limits. ν_b is the decay rate from an excited molecular state to a bound state. ν_f is the decay rate from an excited molecular state to the dissociation continuum in the ground state. ν_L is the laser frequency. The upper state potential has an $1/R^3$ long range form, whereas the ground state potential has an $1/R^6$ dependence.

Photoassociation

Photoassociative collisions create excited state molecules when two colliding atoms in the ground state together absorb a single photon of $\hbar\nu_L$, which is resonant between the energies of ground state at asymptote and of the vibrational level in the excited state.

$$A + B + \hbar\nu_L \rightarrow (AB)^* \tag{3.32}$$

Photoassociation (PA) can produce long range molecules in the excited state efficiently. At the long ranges in the molecular potential, the overlap between the wavefunctions in the ground state continuum and the excited state with high vibrational level is high, giving good Frank-Condon overlap, illustrated in Fig. 3.29. The long range molecule formed in the excited state quickly decays by emitting a photon. Depending on the energy of the decay photon, we can either get two free atoms or bound ground state molecule. With cold atoms, the photoassociation spectroscopy has a high resolution of T = 1 mK $\approx$ 21 MHz. In other words, for narrow spread in initial kinetic energy of colliding atoms, only narrow spread in photon frequency is required to resonantly photoassociate them.

But why photoassociate with such experimental complexities when one can just heat a vapour cell to create molecules? We now answer the question of why we should photoassociate instead of working with thermal molecules.

- PA of atoms produces molecules in high vibrational levels. So-called traditional bound-bound molecular spectroscopy probes molecules in the low vibrational levels in the ground electronic potential. The two methods complement each other.

- Two cold atoms undergoing PA give the natural energy reference. Therefore, PA spectroscopy directly measures the energy difference between the asymptotic atomic ground state and vibrational level in the excited state of the molecular potential.

- For ultracold gases, due to the low temperature, collisions are limited to $l = 0,1$ or 2 (s, p and d waves). PA of the cold atoms creates slowly rotating molecules and gives direct measurements of low rotational levels.

- PA of cold atoms inherently produces a translationally cold molecule which can be trapped and/or manipulated for further study.

- Since PA occurs at long ranges of the potential, resonant dipole and van der Waals interaction terms, C_3 and C_6 can be characterized.

Narrating only few salient features of PA spectroscopy already makes photoassociated cold molecules very interesting species to study various interactions.

The photoassociation rate coefficient [55] yielding a molecule from two colliding ground state atoms is given by

$$k_{pa}(T, \omega_L) = \frac{k_B T}{h Q_T} \sum_{0}^{\infty} (2l + 1) \int_0^{\infty} \left| S_p(\epsilon, l, \omega) \right|^2 e^{-\epsilon/k_B T} \frac{d\epsilon}{k_B T}, \qquad (3.33)$$

where $\epsilon = \hbar k^2/2\mu$ is the asymptotic kinetic energy of the atoms in the MOT, l is the relative angular momentum quantum number, $Q_T = (2\pi \mu k_B T/h^2)^{3/2}$ is the translational partition function, and $S_p(\epsilon, l, \omega)$ is the S-matrix for the PA from the initial ground state to one of the vibrational level in the excited molecular state, expressed as

$$\left| S_p(\epsilon, l, \omega) \right|^2 = \frac{\gamma_p \gamma_s(\epsilon, l)}{(\epsilon - \Delta_b)^2 + (\gamma/2)^2}, \qquad (3.34)$$

where $\Delta_b(\omega_L) = E_b - \hbar \omega_L$ is the detuning from E_b of the bound state, and $\gamma = \gamma_p + \gamma_s(\epsilon, l)$ where $\gamma_p/\hbar$ and $\gamma_s/\hbar$ are spontaneous and stimulated emission rates respectively.

3.5.2 Experimental setup

Lasers

Unlike the conventional PA experiments, we use an amplified diode laser system for PA. It consists of an external cavity diode laser (ECDL) system, which has a mode
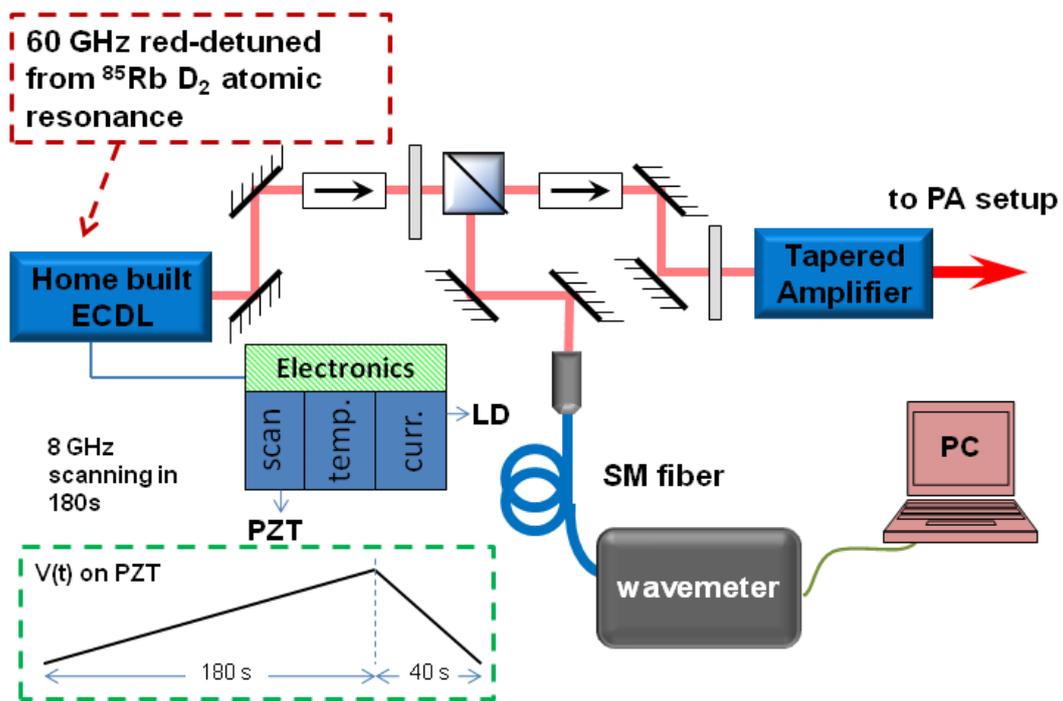
Figure 3.30: For PA, a home-built ECDL is adjusted to give 60 GHz red-detuned from ^{85}Rb D$_2$ transition. Using a scan-controller from toptica, we can scan over 8 GHz at 44 MHz/s speed. A small part of the laser light is fed to the wavemeter to monitor the scanning frequency. Rest of all the light is then fed to a tapered amplifier for intensity amplification.
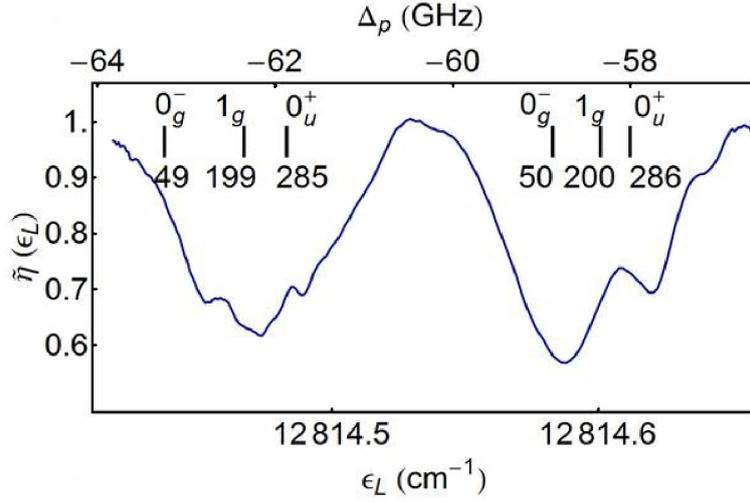
Figure 3.31: The change in MOT fluorescence $\tilde{\eta}(\epsilon_L)$ is shown as a function of the photon energy of the PA laser ϵ_L, scanned over these energies. The molecular states accessed in the present experiment are marked. When $\tilde{\eta}(\epsilon_L) \approx 1$, there is no molecule production. Dips in fluorescence correspond to the excitation of the molecular resonances.

hop free tuning range of $\approx$ 8 GHz at 44 MHz/s and sufficient power to enslave a commercial tapered amplifier (TA) system (toptica:BoosTA), illustrated in Fig. 3.30. The ECDL is adjusted such that it is $\approx$ 60 GHz red detuned from the excited molecular state continuum. An asymmetric triangular waveform of a high voltage signal is fed to a piezo-actuator, which moves the grating to give frequency scanning, shown in a green dashed box in Fig. 3.30. The radius of the PA beam is $\approx$ 0.5 mm and its overlap fraction with the MOT is w $\approx$ 0.77. About 160 mW of power is used for PA, which is more than sufficient to saturate molecule production in the experiment.The frequency of the PA laser is continuously monitored by a wavemeter (HighFinesse: WS/6), which allows the experimental determination of the position of the molecular resonances. There can be a drift in wavelength calibration in the wavemeter. That is corrected by feeding the locked cooling laser beam to the wavemeter.

3.5.3 Sequence and measurements

In saturation the MOT contains $N_a = 2.87 \pm (0.08) \times 10^6$, ^{85}Rb atoms, within a volume $V_a = 1.44 \pm (0.05) \times 10^{-9}$ m^3 at $T_a \approx 150$ μK temperature. The creation of
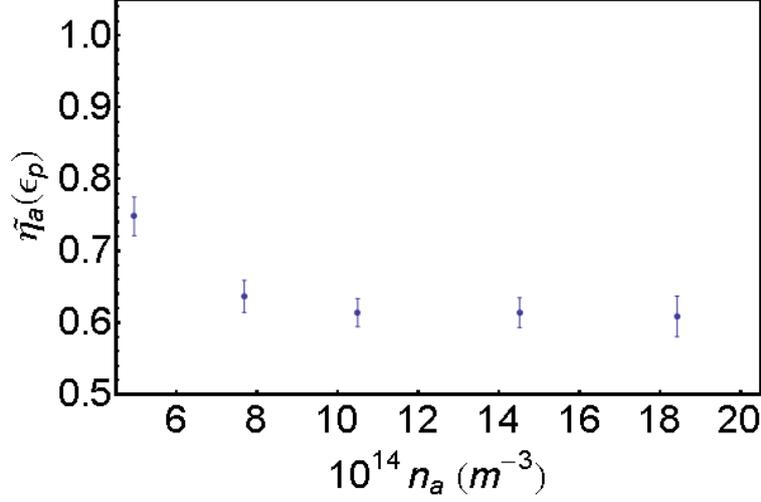
Figure 3.32: The change in MOT fluorescence $\tilde{\eta}(\epsilon_p)$ is shown as a function of MOT density, n_a. $\tilde{\eta}(\epsilon_p)$ remains constant $n_a > 10 \times 10^{14}$ m^{-3}.

bound molecules from the atoms results in energy (ϵ_L) specific loss of MOT atoms, as the PA laser is scanned, corresponding to excitation of specific molecular vibrational levels. The energy dependent depletion of fluorescence due to PA is given by $\tilde{\eta}(\epsilon_L) = \tilde{N}_a(\epsilon_L)/N_a$, where $\tilde{N}_a(\epsilon_L)$ is the remaining number of MOT atoms during PA. The plot of $\tilde{\eta}(\epsilon_L)$ vs ϵ_L is shown in Fig. 3.31 where few vibrational levels of 1_g, 0_u^+ and 0_g^- states are identified and marked.

For the experimental conditions above, we verified that $\tilde{\eta}(\epsilon_L)$ is saturated for all ϵ_L. This is done by measuring $\tilde{\eta}(\epsilon_L)$ as the MOT loading and loss rates are changed, and the only significant dependence at any ϵ_L occurs with changing n_a. The variation of $\tilde{\eta}$ with MOT density n_a, for the strongest molecular resonance in our experiment, corresponding to the closely lying vibrational levels $v = 50$ in 0_g^- and $v = 200$ in 1_g at $\epsilon_p = 12814.59$ cm^{-1} is shown in Fig. 3.32, where above the critical density $n_a^c \approx 1 \times 10^{-15}$ m^{-3}, $\tilde{\eta}$ saturates to $\tilde{\eta}_0$.

3.5.4 Determination of loss rate of atoms in the MOT due to PA

For the saturated MOT with N_a atoms, the loading rate L and the loss rate $\gamma_{ml}N_a$ are equal. When PA at ϵ_p is performed, the atom loss increases due to molecule formation, resulting in a new saturated atom number $\tilde{N}_a$ and a PA loss rate $\tilde{\gamma}_0$ [56]. The rate

equation of the MOT is given in Eq. 3.9 and its solution is in Eq. 3.10. We measure MOT loss rate γ_{ml}, a number of MOT atoms N_a and corresponding density n_a in the steady state without PA laser. Then with PA laser of $\approx$160 mW scanning over 8 GHz at 44 MHz/s, we measure number of MOT atoms $\tilde{N}_a$ as a function of energy of the PA laser. The rate equation for MOT during PA can be written as,

$$\frac{dN}{dt} = L - \gamma_{ml}N - \tilde{\gamma}_0 N \tag{3.35}$$

where L is the loading rate of atoms in the MOT. The solution of the above equation is

$$\tilde{N}_a = \frac{L}{\gamma_{ml} + \tilde{\gamma}_0}. \tag{3.36}$$

Typical trap loss spectrum $\tilde{\eta}(\epsilon_L)$ obtained from the experiment is illustrated in Fig. 3.31 and identified as vibrational levels in 1_g, 0_g^+ and 0_g^- states. We observe significant trap loss about 40 %, which depends on the PA laser intensity and Frank-Condon overlap between initial and final states. Using Eq. 3.10 and 3.36, we get the expression for $\tilde{\gamma}_0$, given as

$$\tilde{\eta}_0 = \frac{\tilde{N}_a}{N_a} = \frac{\gamma_{ml}}{\gamma_{ml} + \tilde{\gamma}_0}, \tag{3.37}$$

therefore, measuring $\gamma_{ml} = 0.148(\pm 0.011)$ s^{-1} [57] and $\tilde{\eta}_0 = 0.619(\pm 0.021)$ from the measurements to give $\tilde{\gamma}_0 = 0.119(\pm 0.010)$ s^{-1}.

Molecular Dynamics simulation for physics with ion trap

Given the experimental goals of our lab and also an optically dark Rb^+ ion, it is essential to develop a numerical tool to understand experimental observations. Generally, two approaches are available; the direct particle-particle calculation taken in the molecular dynamics (MD) simulation and the statistical approach of phase-space calculation using particle-in-cell (PIC) scheme. Here, we choose MD simulation over PIC scheme as it is simple to implement for small systems of few hundred to a few thousand particles and it also gives the dynamics of each charged particle and inter-particle interactions, due to Coulomb interaction ($\propto 1/r$)with reasonable accuracy. PIC scheme is suitable for systems with a large number of particles and gives an evolution of charged particle density as a whole. MD simulation opens the possibilities of incorporating ion-atom interactions ($\propto 1/r^4$). In this chapter, MD simulation method and its numerical implementation are discussed.

4.1 Molecular dynamics simulation for charged particles

4.1.1 Dynamics of point charges

We consider a system of N charged particles of mass, M and charge, Q under the influence of external electric field, $\mathbf{E}_{ext}(\mathbf{r}, t)$ which is the ion trapping field. The equation

of motion of such an N charged particle system is

$$\frac{d}{dt}\mathbf{r}_i = \mathbf{v}_i, \tag{4.1}$$

$$M\frac{d}{dt}\mathbf{v}_i = \mathbf{F}_i^c + Q\mathbf{E}_{ext}(\mathbf{r}_i, t), \tag{4.2}$$

$$\mathbf{F}_i^c = -Q\nabla_i\Phi_c(\mathbf{r}_i, t) = \frac{Q^2}{4\pi\epsilon_0}\sum_{j\neq i}^{N}\frac{\mathbf{r}_i - \mathbf{r}_j}{|\mathbf{r}_i - \mathbf{r}_j|^3}, \tag{4.3}$$

where the force on the *i*th particle in Eq. 4.2 consists of the ion trapping field, $\mathbf{E}_{ext}(\mathbf{r}, t)$ and the Coulomb force, $\mathbf{F}_i^c$ from all other charged particles.

A solution of the equations of motion in Eq. 4.1 and 4.2 can be obtained by a numerical integration of these differential equations where the internal forces $-Q\nabla\Phi_c$ are calculated directly from the actual positions $\mathbf{r}_i$ using Eq. 4.3. Such particle-particle calculations are known as molecular dynamics simulations.

In the case of cooling of ions in the buffer gas of lighter mass (generally He gas), the time-averaged cooling effect of the buffer gas can be simulated in two ways: by viscous damping and collisional damping [18]. Viscous damping is very easy to implement in the equation of motion. The damping force $\mathbf{F}_d$ is proportional to the ion velocity and is expressed as,

$$\mathbf{F}_d = -\gamma_v M\frac{d\mathbf{r}}{dt}. \tag{4.4}$$

The damping coefficient, γ_v is

$$\gamma_v = \frac{M_{bg}}{M + M_{bg}}\frac{p}{k_B T}\frac{Q}{2\epsilon_0}\sqrt{\alpha\frac{M + M_{bg}}{MM_{bg}}}, \tag{4.5}$$

where M_{bg}, T and p are mass, temperature and pressure of the buffer gas, α is the polarizability of the buffer gas.

Although we have not implemented collisional damping of ions with neutral atoms, it is worthwhile to mention it briefly here for future development on the present MD simulation. Collisional cooling mechanism is based on hard sphere scattering process of the interaction between the ion and the buffer gas particles. The long range interaction of the ion with the buffer gas (polarized by the ion) allows the gas as a viscous medium, creating a damping force. The potential, $V(r)$ which describes the interaction

65

between an ion with a neutral atom/molecule at a distance r is

$$V(r) = \frac{B}{r^n} - \frac{C_6}{r^6} - \frac{C_4}{r^4},$$

(4.6)

where C_4 and C_6 are the dipole and quadrupole polarizabilities of the neutral atom / molecule. The short range repulsive part of the interaction is empirically described by B/r^n. The maximum impact parameter, b_{max} is calculated to get a finite time between two collisions by specifying a cut−off angle of a minimum scattering angle, θ_{min}. The impact parameter, b is generated from a probability distribution, which increases linearly with b, limited by b_{max}. The velocity distribution at $t = 0$ is assumed to be Maxwell−Boltzmann distribution. For given initial distribution of position and velocity of N ions, the ions' trajectories are calculated till the next collision takes place. When a collision occurs, the scattering angle, $\Theta(b, E)$ as a function of the impact parameter, b and the energy, E, can be determined from the potential in Eq. 4.6 and is given by

$$\Theta(b, E) = \pi - 2b \int_{r_a}^{\infty} \frac{1}{\sqrt{1 - \frac{b^2}{r^2} - \frac{V(r)}{E}}} \frac{dr}{r^2},$$

(4.7)

where the integration over the distance, r between the ion and the neutral starts from the distance of closest approach, r_a, which is the sum of radii of the ion and the neutral. From the angle of scattering of the ion in Eq. 4.7, we determine the velocity of the ion after the scattering event. Having done such a calculation for N particles, one can obtain a velocity distribution at a temperature of the ion ensemble. Algorithm and related references of the buffer gas cooling of ion are described systematically in 'Simulations for Ion traps − Buffer Gas Cooling' chapter in [18].

4.1.2 Numerical realization

The ordinary differential equations, in our case, Eq. 4.1 and 4.2 can be solved in several ways such as Euler integration, leap frog and Runge-Kutta (4th order) integration methods. In our MD simulation code, we use the leap-frog scheme to calculate the particle propagation. The main feature is a shift of half a time-step between the time-levels of positions and velocities. r_n at time $t_n = n\delta t$ and v at $t_{n-\frac{1}{2}} = \left(n - \frac{1}{2}\right)\delta t$ are

advanced in half a time-step [18], as given below

$$v_{n+\frac{1}{2}} = v_{n-\frac{1}{2}} + \frac{\mathbf{F}_n}{M}\delta t \ ,$$

$$r_{n+\frac{1}{2}} = r_n + v_{n+\frac{1}{2}}\delta t. \tag{4.8}$$

4.2 Implementation of the MD simulation

The MD simulation is divided into several stages:

1. Initialization

2. Main simulation

3. Output analysis

Initialization part sets up the environment for the simulation to start. It reads necessary inputs and SIMION generated potential array files, and generates ion position and velocity distributions. The inputs include temperature, damping coefficient, ion ejection condition and experimental operating parameters such as V_{rf}, U_{endcap} and ν_{rf}. The main simulation contains Coulomb force calculation and time-propagation of ions in the Coulomb and external electric field. Output of the MD simulation can be analyzed in various ways to extract the information required, such as evolution of single ion trajectories, temperature of the ion velocity distribution, secular motion frequency and mass spectrum from time of flight information. Details of these implementations are discussed in following sections and illustrated in a flow chart, given in Fig. 4.1.

4.2.1 Initialization

Geometry of the trapping potential and inputs of experimental parameters are set initially and remains the same throughout the MD simulation. Ion positions and velocities at $t_n = n\delta t$ are calculated from the ion positions and velocities at time $(n-1)\delta t$.
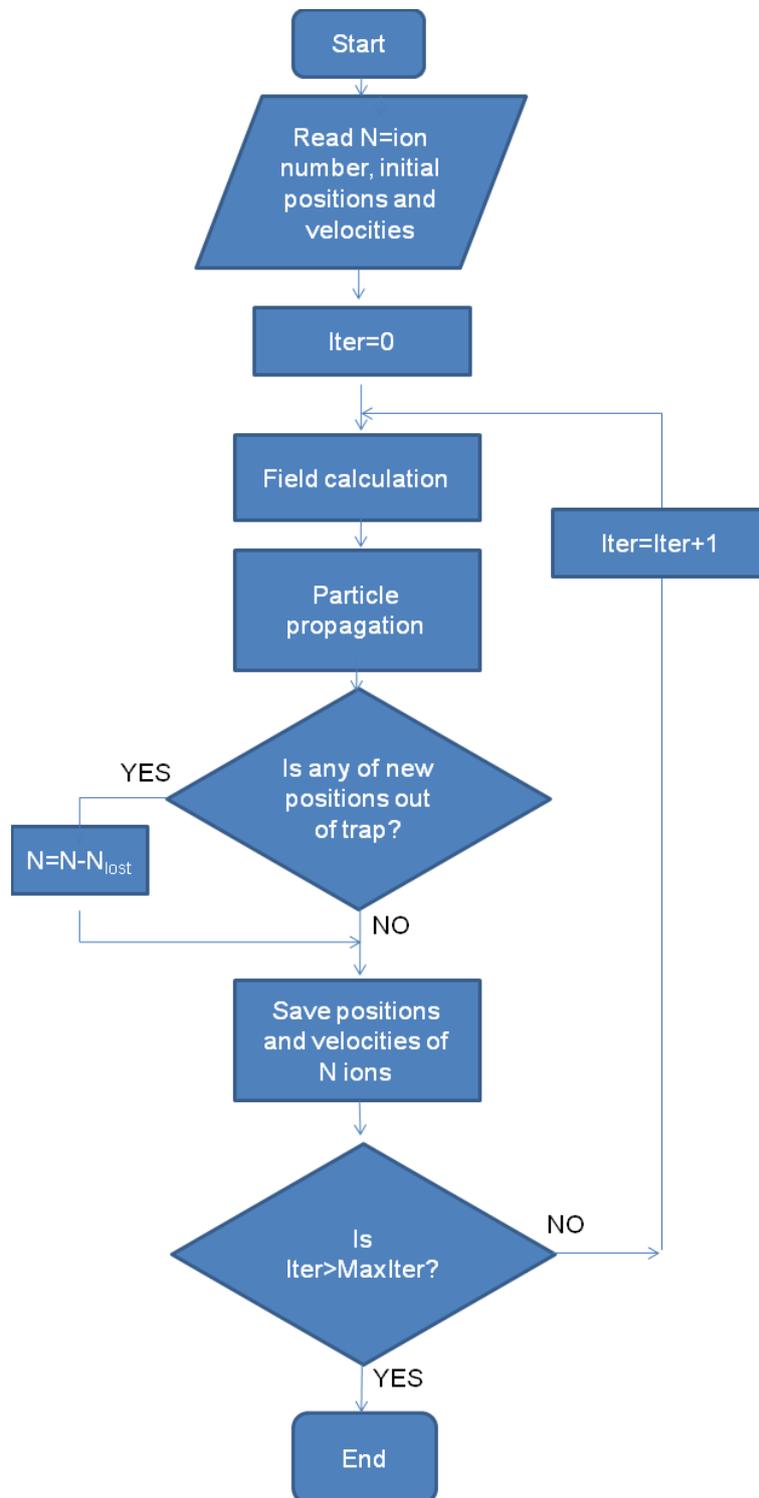
Figure 4.1: A flow chart for ion trajectory integration
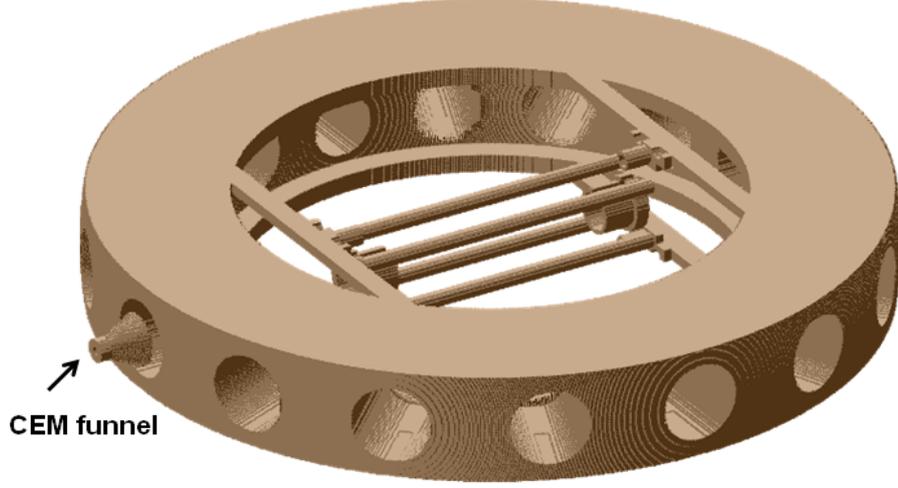
Figure 4.2: The SIMION 7.0 rendering of the ion trap geometry is illustrated.

Geometry

In the chapter, 'A novel Ion trap design', the procedure to obtain a trapping potential from the SIMION 7.0. is described. Here we use the same procedure to calculate the trapping potential using the geometry of modified linear Paul trap. The geometry of the electrodes and their voltages are defined in a geometry file (.GEM file). The three dimensional view of the ion trap geometry is rendered in SIMION 7.0 as shown in Fig. 4.2. A separate geometry file is made for each electrode held at 1 V and all others at ground. SIMION takes each geometry file as an input and generates a corresponding potential array by solving the Laplace equation using a modified Runge−Kutta 4th order method. We use Mathematica to interpolate the potential arrays. These interpolated functions are weighted by their respective time-varying voltages and dc endcap voltage and superposed into a total potential. Let's say $V_{q1}(x,y,z)$ is the potential array calculated for one diagonal set of quadrupole electrodes, $V_{q2}(x,y,z)$ of opposite set, $V_{e1}(x,y,z)$ and $V_{e2}(x,y,z)$ are the potential array for endcap electrodes, and $V_{cem}(x,y,z)$ is for the CEM. Then we can write the total potential as

$$
\begin{aligned}
V_{tot}(x,y,z,t) \;=\;& V_{rf}cos(2\pi\nu_{rf}t)V_{q1}(x,y,z) - V_{rf}cos(2\pi\nu_{rf}t)V_{q2}(x,y,z) \\
& + U_{endcap1}V_{e1}(x,y,z) + U_{endcap2}V_{e2}(x,y,z) + V_{b}V_{cem}(x,y,z)
\end{aligned}
$$

$$(4.9)$$

where $U_{endcap1}$ and $U_{endcap2}$ are endcap voltages for endcap 1 and 2. Endcap 2 is one near to the CEM and switches from 80 V to -5 V at the time of extraction. V_b is the CEM bias voltage at - 2400 V.

Ion position distribution

Position distribution is assumed to be a Gaussian distribution of mean = 0 and σ_x, σ_y and σ_z. Due to the ion trap geometry, $\sigma_x = \sigma_y < \sigma_z$.

Ion velocity distribution

Based on Kinetic theory of gas, the Maxwell−Boltzmann distribution of speed is used for the initial velocities of ions. The probability density function for the Maxwell−Boltzmann distribution is given by three dimensional Gaussian distribution of mean = 0 and $\sigma_{v_x, v_y, v_z} = k_B T / M$ as follows,

$$f_v(v_x, v_y, v_z) = \left(\frac{M}{2\pi k_B T} \right)^{3/2} exp \left(-\frac{m(v_x^2 + v_y^2 + v_z^2)}{2k_B T} \right), \qquad (4.10)$$

where v_x, v_y and v_z are velocity components in x, y and z directions, M is the mass of the ion, k_B is Boltzmann constant and T is temperature.

Damping

In most of our simulations, we keep $\gamma_v = 0$ kg/s. Collisional damping was implemented for single ion calculation, described in Ravi Krishnamurthy's thesis [43].

Boundary ejection

When an ion gets ejected due to heating, its velocity increases and $|r_n - r_{n+1}| >$ trap size. This test condition is applied at the end of every time integration, illustrated in Fig. 4.1.

4.2.2 Main simulation

For given input parameters and, positions and velocities of N ions at time t_n, the main simulation consists of four major steps:

- Calculation of Coulomb force on ith ion due to all other ions,

- The total force (= Coulomb force + ion trapping force) on the ith ion.

- Trajectory integration over δt.

- Extraction

Coulomb calculation

In our MD simulations, even small systems contain a few hundred up to a few thousand particles. Coulomb interaction is conceptually easy to implement, but due to the long-range nature of the interaction, a computational effort for the force calculation scales with N^2. Therefore, we need an approximate treatment of the Coulomb interaction between the charged particles. In plasma physics, Coulomb interaction is divided into short range part and long range part. In the short range, direct Coulomb force calculation takes place, for the collisions with momentum and energy transfer. For the long range contribution and the collective effect, ions can be considered as weakly coupled collision-less plasmas, which are characterized by a plasma parameter, Γ_p.

$$\Gamma_p = \frac{Q^2}{4\pi\epsilon_0 a k_B T} \, , \quad \frac{1}{a} = \left(\frac{4\pi}{3} n_i \right)^{1/3}$$

for plasma with density, n_i and temperature, T.

Γ_p is basically the ratio between the interaction energy, $Q^2/(4\pi\epsilon_0 a)$ and thermal energy, $k_B T$. For $\Gamma_p \ll 1$ (weakly coupled plasmas), the thermal motion dominates the charged particle dynamics and hard collisions are rare. The plasma parameter gives an overall macroscopic electric field for the long range part of Coulomb force calculation, and reduces the computational effort for large N ions. But to use Γ_p in the calculation, one needs the information of n_i and T which are not so trivial to obtain in our system,

because of dilution and rapidly oscillating fields. Therefore, we choose the direct brute force calculation for a few hundred particles.

Coulomb force, $\mathbf{F}_i^c$ of ith charge particle due to all $(N-1)$ other charged particles is

$$\mathbf{F}_i^c = \sum_{j \neq i}^{N} \mathbf{F}_{ij}, \tag{4.11}$$

where $\mathbf{F}_{ij} = \frac{Q^2}{4\pi\epsilon_0} \frac{|\mathbf{r}_i - \mathbf{r}_j|}{|\mathbf{r}_i - \mathbf{r}_j|^3}$. To avoid double counting, we construct an $N \times N$ matrix of the form

$$\mathbf{F} = \begin{pmatrix} 0 & \mathbf{F}_{12} & \mathbf{F}_{13} & \mathbf{F}_{14} & \mathbf{F}_{15} & \cdots \\ 0 & 0 & \mathbf{F}_{23} & \mathbf{F}_{24} & \mathbf{F}_{25} & \cdots \\ 0 & 0 & 0 & \mathbf{F}_{34} & \mathbf{F}_{35} & \cdots \\ 0 & 0 & 0 & 0 & 0 & \cdots \\ \vdots & \vdots & \vdots & \vdots & \vdots & \ddots \\ 0 & 0 & 0 & 0 & 0 & 0 \end{pmatrix}$$

For all $\mathbf{F}_{ii} = 0$ and upper triangular elements in the above matrix are related with the lower triangular elements such as $\mathbf{F}_{ij} = -\mathbf{F}_{ji}$ i.e. $-\mathbf{F}^T$. Therefore the entire Coulomb matrix can be written as,

$$\mathbf{F}^c = \mathbf{F} - \mathbf{F}^T. \tag{4.12}$$

This does not improve much in computational effort, nevertheless computation time for Coulomb interaction part is decreased by half, i.e. $\approx \frac{N^2}{2}$.

Field calculation

Electric field vector, $\mathbf{E}$ value is evaluated at any point in the trap from SIMION generated trapping potential array. The net force on ith particle is $Q\mathbf{E} + \mathbf{F}_i^c$.

Trajectory calculation

Trajectory calculation is a time-integration in which the position and velocity of the ion are known at $t = 0$. Equation of motion of ions with the trap volume is given by

$$\frac{d^2u}{dt^2} = \frac{1}{M}(QE_u + F_u^c + F_u^d), \tag{4.13}$$
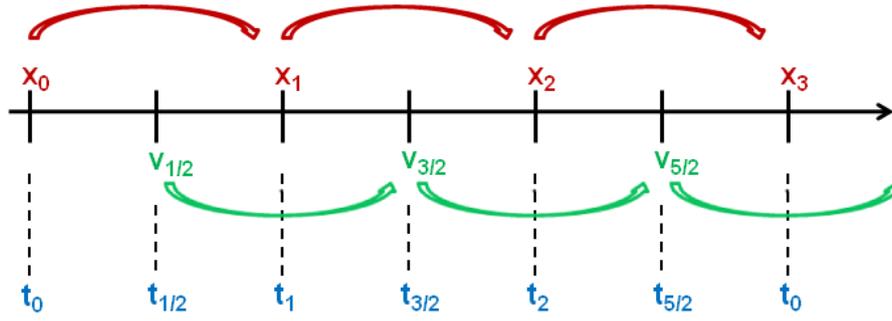
Figure 4.3: This method uses the derivatives at the midpoint of each step. This only requires one additional step to be taken in order to move the velocity a half step ahead of the position. Because of its better accuracy while still keeping the computation time relatively low, the Leapfrog method is employed in the simulation.

where $u = x, y$ and z of the ion, E_u is the magnitude of electric field along u, F_u^c is the component of Coulomb force in u direction and damping force is $\mathbf{F}^d = -\gamma_v \mathbf{v}$. This is numerically integrated to find position and velocity at subsequent time steps. The second order differential equation 4.13 can be converted into two first order equation of the form Eq. 4.1,

$$\frac{du}{dt} = v_u, \tag{4.14}$$

$$\frac{dv_u}{dt} = \frac{1}{M}(QE_u + F_u^c + F_u^d). \tag{4.15}$$

Our most of calculations are done with $F_u^d = 0$.

Leap frog method implementation

For every position and velocity calculation, their components along x, y and z axes are considered separately. Leapfrog scheme for x_n and $v_{x,n}$ along x direction at time $t = n\delta t$ is given as,

$$
\begin{aligned}
v_{x,n-\frac{1}{2}} &= v_{x,n-1} + \frac{\delta t}{2} a_{x,n-1}, \\
v_{x,n+\frac{1}{2}} &= v_{x,n-\frac{1}{2}} + a_{x,n}\delta t, \\
x_{n+1} &= x_n + v_{n+\frac{1}{2}}\delta t,
\end{aligned}
\tag{4.16}
$$

where $a_{x,n}$ is acceleration calculated from Eq. 4.15 using values of x_n and $v_{x,n}$.
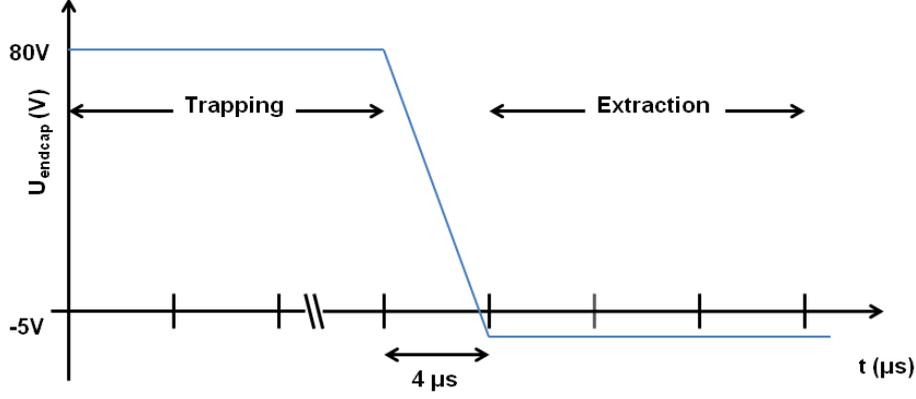
Figure 4.4: Endcap voltage transient time is about $4\mu s$ and is assumed to be linear.

Extraction

After evolving ions in the trap for some finite time (i.e. at $V_{rf} = 91.7$ V, $U_{endcap1} = U_{endcap2} = 80$ V and $V_b = -2400$ V), we apply -5 V to one of the endcap electrodes (endcap 2) near to the CEM for the extraction (now at $V_{rf} = 91.7$ V, $U_{endcap1} = 80$ V, $U_{endcap2} = -5$ V and $V_b = -2400$ V). Switching $U_{endcap2}$ from 80 V to - 5V takes 4 μs transient time, shown in Fig 4.4. This introduces a shift and spread in time of flight signal at the CEM. To match time of flight from the MD simulation and the experimental data, we keep a linear decline rate as $\frac{(-5-80)}{4} = -21.25$ V/μs.

4.2.3 Analysis

This section shows the numerical results obtained from the MD simulation along with validation wherever possible. General sequence of MD simulation is as follows;

1. N ions are loaded in the ion trap and evolved in the trap for some finite time, let's say for 50 μs.

2. At the end of 50 μs, $U_{endcap2}$ is switched from 80 V to -5 V for the extraction in 4 μs of transient time.

3. Ions are allowed to evolve for another 60 μs to complete their extraction till the CEM funnel.

74
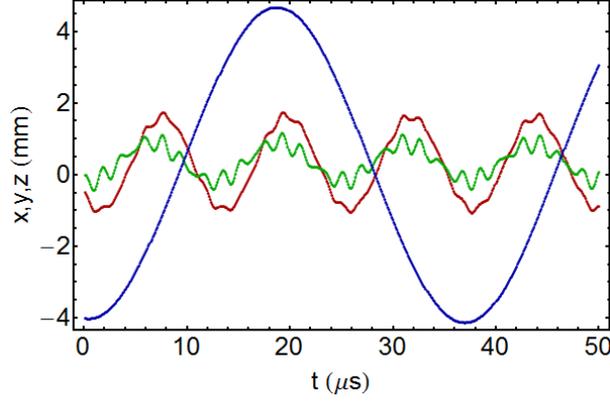
Figure 4.5: Trajectories of an ion in x (red), y (green) and z (blue) directions are calculated by MD simulation. Spatial extent of z trajectory is much larger than that of x and y due to the trap geometry and operation.
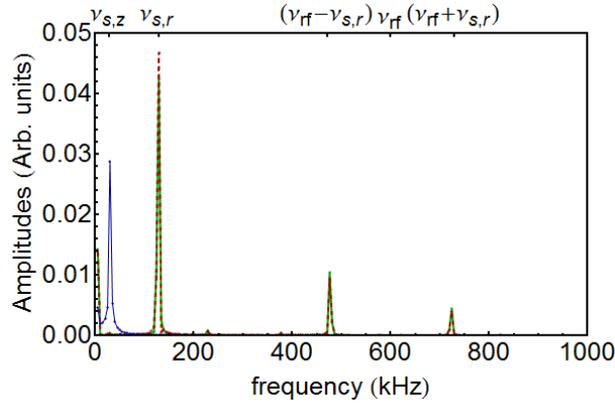
Figure 4.6: Fourier spectra of ion trajectories computed at $\nu_{rf} = 600$ kHz in x (red, dashed), y (green) and z (blue) directions are illustrated. Fourier transform of each trajectory gives secular motion frequency, ν_s of each direction.

Ion trajectories

First, we analyze trajectories of each ion. Fig. 4.5 shows the one of typical ion trajectories in the ion trap. Ion motion in x and y directions is an oscillation of small amplitude at the frequency, ν_{rf} superimposed on a smoothly varying secular motion. Applying Fourier transform on ion trajectories along x, y and z directions, we get micromotion and secular motion frequencies, as shown in Fig. 4.6. Secular motion frequencies of x and y trajectories, ω_x, ω_y are the same due to ion trap geometry and operation and are larger than that of z trajectory, ω_z. $\nu_{s,r} = \omega_x/2\pi = \omega_y/2\pi = 127$
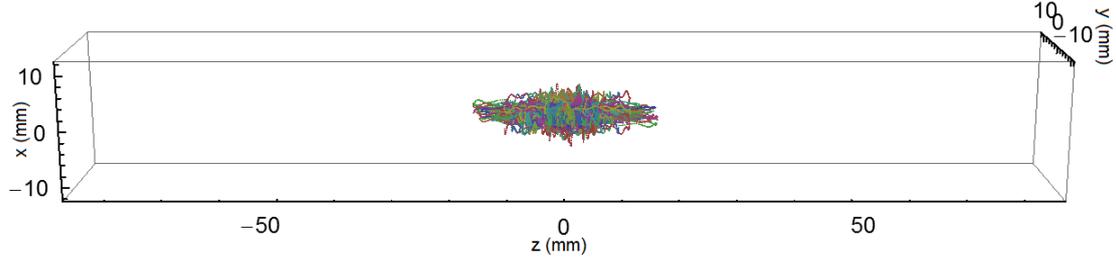
Figure 4.7: About 200 ions are evolved in the ion trap for 50 μs. Ion cloud has an ellipsoidal shape of $r_x = r_y < r_z$.
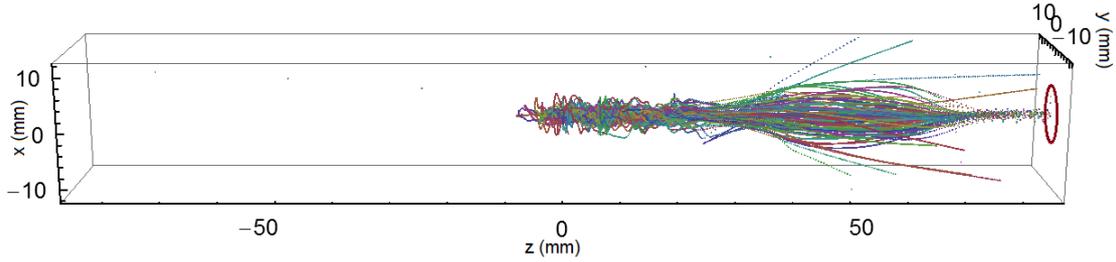
Figure 4.8: Ions are extracted toward the CEM through the endcap ring held at -5 V and placed at z=51 mm. A red ring in x-y plane is a mouth of the CEM.

kHz and $\nu_{s,z} = \omega_z/2\pi = 26$ kHz. Due to small amplitude of the trajectory at the driving frequency, amplitude of the Fourier spectra is also very small. Peaks at $\nu_{rf} \pm \nu_s$ are harmonics.

Extraction

Fig. 4.7 illustrates about 200 ions which are evolving in the ion trap potential over 50 μs. When $U_{endcap2}$ is switched from 80 V to -5 V, ions are fled towards a mouth of the CEM shown in Fig 4.8. The endcap ring near to the CEM acts like an electrostatic lens to focus the ion beam. The MD simulation accounts for the lensing effects in the extraction. Arrival times of ions at the detector's position are analyzed. The response function for the detector circuit is convolved onto the extracted ion distribution to mimic the experiment. Fig. 4.9 shows ToF analysis of the ion arrival times at the CEM's position. The convoluted ToF is plotted with a blue line in arbitrary units.
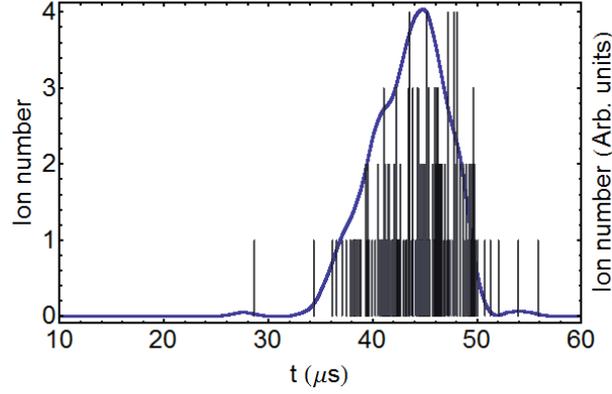
Figure 4.9: Left-side y axis shows ToF analysis of the ion arrival times at the CEM's position and right-side y axis is the convoluted arrival times distribution of ions with the preamplifier response function.

4.3 Result

The MD simulation is performed to estimate temperature of Rb^+ ion cloud from a ToF width signal from the experiment [8] where Ravi *et al.* measure the evaluation of trapped ion number and distribution when ions are held in the trap with and without cold atoms in the MOT for different hold times, τ_{ih}. Experimental results are plotted in Fig 4.10. Fig 4.10 (a) plots the number of Rb^+ as a function of τ_{ih} with MOT atoms (blue circles) and without MOT atoms (red dots). Ions rapidly exit the iontrap without cold atoms, whereas with cold atoms, ions stay much longer and a stable number of ions (187 ± 9) is trapped beyond 120 s. (b) illustrates the width (FWHM) of ToF signal as a function of τ_{ih}. In the absence of cold atoms, the FWHM increases in time as the trap empties out. On the other hand, with cold atoms, the FWHM decreases as τ_{ih} increases.

Given that the constant number of trapped ions for $\tau_{ih} > 2$ min and a systematic decrease in the arrival time widths, the temperature at any hold time is evaluated applying Virial theorem. An ion distribution, consistent with a given temperature value, is evolved within a numerically generated potential for the ion trap system that includes the CEM, using the interacting ion MD simulation described above.
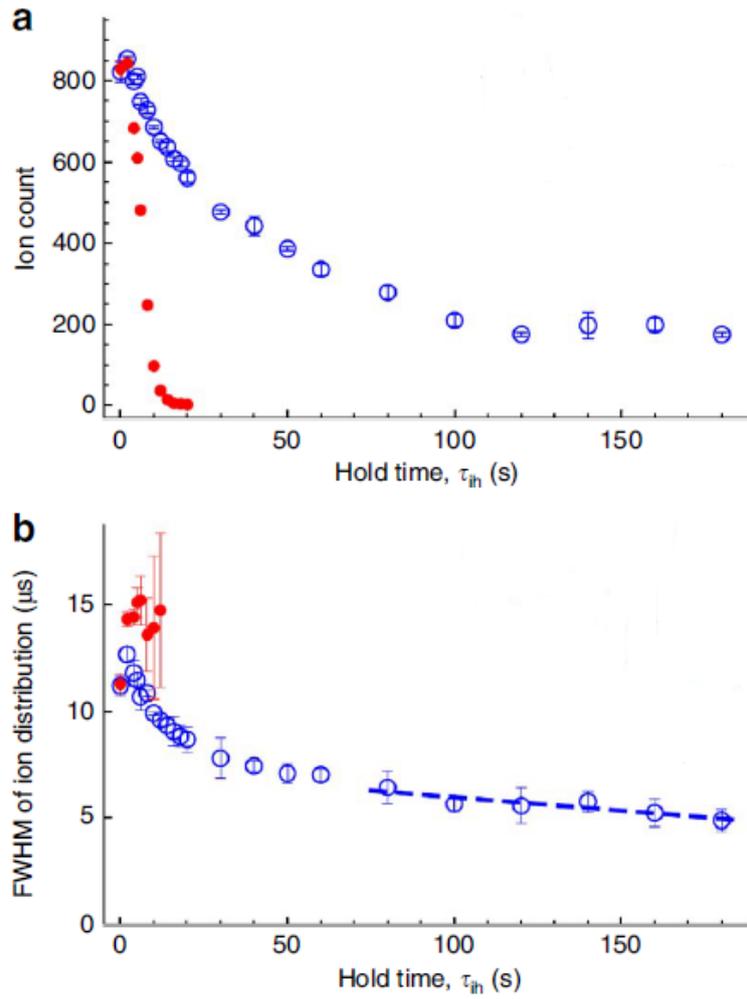
Figure 4.10: Change in the trapped ion population and the FWHM of ToF as a function of τ_{ih} are plotted for ions held with cold atom (blue circles) and without cold atoms (red dots).

4.3.1 Virial theorem

For the MD simulation, the initial distributions of the positions and velocities of trapped ions, consistent with a specific temperature are generated using the Virial theorem. We assume that the ion-ion and ion-atom interactions are negligible. This is reasonable because the ion-ion collisions are occasional and the ion-atom collisions are rare within a single macromotion cycle, which is a natural time to take an average over. The surviving trap potential term after time averaging over the macromotion cycle can be substituted by the corresponding harmonic secular potential (V^{HO}) and the Virial equation for the present problem reduces to $\overline{T_k} \approx \overline{V^{HO}}$, where T_k = kinetic energy of ions. This equation determines the relation between the spatial and velocity distributions of ions at temperature T in the trap. The variances of the position and velocity distributions ($\sigma_i^2, \sigma_{v_i}^2$), consistent with temperature T is now given by $\omega_i^2 \sigma_i^2 = \sigma_{v_i}^2 = k_B T / M$, $i \in (x, y, z)$, where the ω_i are the macromotion frequencies, k_B is the Boltzmann constant and M is the mass of the ion.

4.3.2 Temperature estimation from the width of the ion signal

The initial spatial and velocity distributions for ensembles of 187 ions are generated at different temperatures, using the Virial theorem. Each ensemble consistent with the Virial theorem is evolved for a few macromotion cycles and extracted in the interacting ion MD simulation. The FWHM of arrival time distribution is plotted against the temperature in Fig 4.11. The width increases as temperature increases. We take last four points in Fig. 4.10 (b) to relate the experimentally measured width of the ToF distribution to the temperature of the ion cloud from the MD simulation. From this analysis, we estimate the temperature for the trapped ions as $\approx$ 30 K at $\tau_{ih} = 180$ s. The above temperature value represents an upper bound for the ion system so held. The ion system is capable of lower temperatures; however, our ability to determine the ion temperature significantly below this value, by the method described above, is limited. This is because at lower temperatures, for a fixed ion number, the ion density
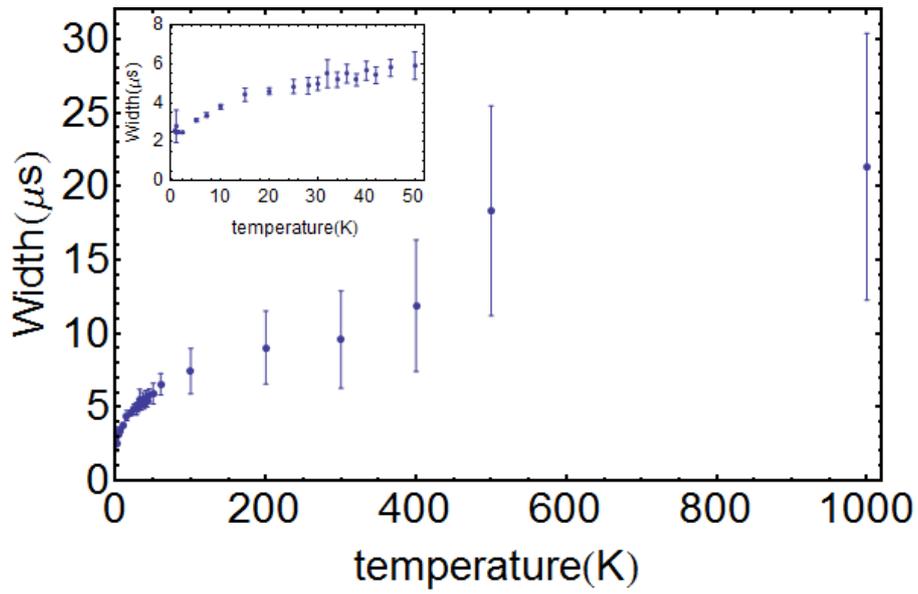
Figure 4.11: The MD simulation result of width of ToF signal as a function of temperature of 187 ion ensemble is illustrated. The Virial theorem is applied to generate the initial spatial and velocity distribution of ion ensembles at temperatures from 0.5 to 1000 K. At each temperature, the ion ensemble is extracted in the interacting MD simulation and its ToF is recorded. The width of ToF increases with the temperature. A zoomed portion at low temperatures is given in the inset, where we characterize the temperature of the ions in our experiment [8].
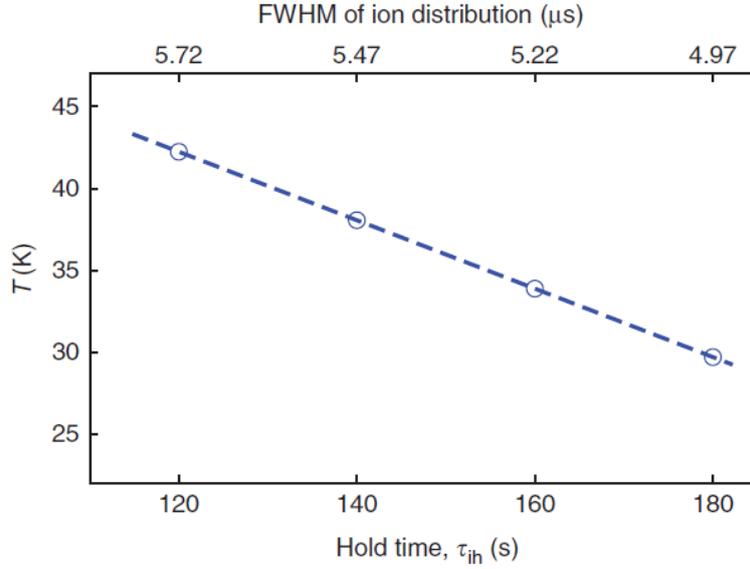
Figure 4.12: The trapped ion ensemble temperature is determined for the duration when the ion number has stabilized, that is for $2 \leq \tau_{ih} \leq 3$ min. For this duration the temperature fit to the trapped ions as obtained from MD simulations (dashed line) is plotted as a function of trap hold time. The corresponding experimental ToF width of the extracted ions is marked on the top axis. The open circles represent the hold times at which the experimental measurements were made.

increases. The resulting increase in the ion-ion interaction then invalidates the approximate form of the Virial theorem described above. For significant ion-ion interaction, we take a potential experienced by ions which consists of ion trapping potential and interaction Coulomb potential and is given by,

$$U = V^C + V^{HO}, \tag{4.17}$$

where V^C and V^{HO} are Coulomb and harmonic oscillator potential energies respectively. Relation between time-average T_k and U is

$$2\overline{T_k} = \overline{-V^C + 2V^{HO}}. \tag{4.18}$$

Detailed derivation is in Appendix B which shows how Virial theorem can be applied in the potential of non-homogeneous functional form. Apart from the temperature estimation, we find another interesting result. The simulation shows that beyond $T = 1000$ K, most of ions are unstable and leave the trap rapidly. The limiting temperature

of the trapped ion cloud is now considered to be $\approx$ 1000 K. This result is applied in Chapter 5.

Measurement of collision rate coefficient in ion-atom system

In the trapped ion collision experiments, ion-neutral collision rate coefficient is measured from the loss of ions from the trap [58, 59]. For optically dark ions, this loss is measured by sweeping the ion resonance frequency or by extracting the trapped ions to charge particle detectors [58]. So *in situ* detection of optically dark ions becomes challenging without disturbing the system. However, in mixed ion-atom trapping experiments in which the ions are optically dark, the cold trapped atoms interacting with ions can be directly measured in situ, by atomic fluorescence, without affecting the trapped ions. In this chapter, we develop a method to measure ion-atom collision rate coefficient in such a hybrid system using atom fluorescence as a probe.

In the experiment, we trap the optically dark Rubidium (^{85}Rb$^+$) ions, derived from the laser cooled ^{85}Rb atoms in a MOT. The ions are created and accumulated at the center of the ion trap, which overlaps with the MOT. Such a system evolves into a mixture with constant numbers of trapped atoms and ions in steady state. The ionization of the MOT atoms and the subsequent trapped ion interaction with the atoms results in a depletion of the atoms from the MOT. The consequent drop in MOT fluorescence is utilized to develop the framework for the measurement of the collision rate coefficient for ion-atom interactions.

5.1 Model for the loss of trapped atoms

A rate equation model is constructed to describe the evolution of ion-atom system. Each loss channel of atoms from the MOT in the experiment is investigated in detail. The rate equation for atoms in the MOT is already discussed in Section 3.1.3. We briefly

mention few important equations to start with. The time dependence of N_{MOT} can be written as

$$\frac{dN_{MOT}}{dt} = L - \gamma_{ml}N_{MOT}, \tag{5.1}$$

with L, the loading rate of the atoms from the background vapor into the MOT and γ_{ml}, the loss rate of the MOT atoms, due to collision with background vapour, the trap loss due to collisions between two trapped atoms. The time dependent solution of the above equation with initial condition $N_{MOT}(0) = 0$ is

$$N_{MOT}(t) = N_0(1 - e^{-\gamma_{ml}t}), \quad N_0 = \frac{L}{\gamma_{ml}}. \tag{5.2}$$

where N_0 is the steady state atom number in the MOT, in the limit of large time.

5.1.1 Photo ionization of atoms

The blue light source (BLS) excites atoms in the $5P_{3/2}$ state to the ionization continuum. The fraction of atoms in the excited state f_e is determined from the photon scattering rate from an atom and can be written as [45]

$$f_e = \frac{N_e}{N_g + N_e} = \frac{(\Omega/\Gamma)^2}{1 + 4(\delta_c/\Gamma)^2 + 2(\Omega/\Gamma)^2}, \tag{5.3}$$

where, $\Omega = 2\pi \times 16.7$ MHz is the Rabi frequency and $\Gamma = 2\pi \times 6$ MHz is the decay rate of the excited atomic state. A Rb atom in this excited state requires the photon energy ≥ 479 nm to get ionized [60]. The central wavelength of the BLS is at $\lambda_{pi} = 456$ nm, which is sufficient to ionize the excited Rb atoms. The intensity of the BLS light incident on the MOT is denoted by I_{pi}. For photo ionization energy $E_{pi} = hc/\lambda_{pi}$, the ionization cross-section is denoted by σ_{pi}. The photon energy which is in excess of the ionization energy is carried away by the ejected electron, with the resulting ion suffering the recoil.

The loading rate of the MOT remains unchanged when the BLS is switched on for photo ionization, as the population of the background atoms remains unchanged. The maximum intensity of the BLS used is 1.33 mW/cm^2. The rate equation for the MOT, when the BLS is ON is modified to

$$\frac{dN_{MOT}}{dt} = L - \gamma_{ml}N_{MOT} - \gamma_{pi}N_{MOT}, \tag{5.4}$$

where a new loss rate due to photo-ionization, γ_{pi} adds to the losses inherent to the operation of the isolated MOT to give a new loss rate of $\gamma_t = \gamma_{ml} + \gamma_{pi}$ [47, 61]. Here we assume that since the ion trap is switched off during photo ionization, the ions and electrons created from the MOT atoms immediately leave the system and play no further role in determining the number of trapped atoms. The ionization rate of the excited Rb atoms by radiation from the BLS can be written as [47, 61]

$$\gamma_{pi} = \frac{\sigma_{pi} I_{pi} f_e}{E_{pi}} = \zeta I_{pi}, \tag{5.5}$$

where $\zeta = \left(\frac{\sigma_{pi} \lambda_{pi} f_e}{hc} \right)$. The corresponding time dependence of N_{MOT} with initial condition $N_{MOT}(0) = 0$ and the inclusion of the ionizing process can then be written as

$$N_{MOT}(t) = \frac{L}{\gamma_t} (1 - e^{-\gamma_t t}). \tag{5.6}$$

5.1.2   Ion-Atom interaction loss

Once the ion trap is switched ON, then a fraction of the created ions is loaded into the ion trap which overlaps the MOT. Since the ion and atom traps are optimally overlapped, the ions created from the MOT have negligible velocity upon creation and get loaded into the minimum of the trap. These ions gain in kinetic energy as they evolve in the field of the ion trap. As the number of ions loaded in the ion trap grows, the spatial distribution of the trapped ions increases outward from the trap centers. Since the MOT volume is much smaller than the volume of the trapped-ion spatial distribution, then long before the total number of trapped ions equilibrates, the number of ions at any instant overlapped with the MOT stabilizes. Therefore the collision rate between the trapped ions and the MOT atoms also stabilizes rapidly, allowing the definition of a time-independent binary ion-atom interaction rate, γ_{ia} for the constituents of the ion-atom mixture. Since atoms are weakly trapped with respect to ions, they can gain sufficient energy in collision with trapped ions to exit the MOT. This is a new loss channel for the atoms trapped in a MOT, which can be written as

$$\frac{dN_{MOT}}{dt} = L - (\gamma_{ml} + \gamma_{pi} + \gamma_{ia}) N_{MOT}, \tag{5.7}$$

where γ_{ia} is a new loss channel for the atoms trapped in the MOT due to binary ion-atom interaction. The resulting time evolution for N_{MOT} with initial condition $N_{MOT}(0) = 0$ therefore becomes,

$$N_{MOT}(t) = \frac{L}{\gamma_{tot}}(1 - e^{-\gamma_{tot}t}), \tag{5.8}$$

where $\gamma_{tot} = \gamma_t + \gamma_{ia}$ is the total loss rate of MOT atoms, when the ion and atom traps are operated simultaneously. We note that, while the ion density overlapping with the MOT volume stabilizes rapidly, the number and the velocity distribution of the trapped ions evolve continuously until the ion trap is filled to its limit. Thus the rate of ion loss from the ion trap and the evolution of N_{MOT} are linked.

5.1.3   Number of trapped ions

The ion trap is loaded from the minimum of the secular trap potential, by photo-ionization of the overlapping MOT atoms. The time dependence of number of trapped ions, N_I for a given photo-ionizing intensity I_{pi} can be written as,

$$\frac{dN_I}{dt} = L_I - \gamma N_I, \tag{5.9}$$

where γ is the ion trap loss rate and L_I, loading rate of ions in the iontrap which can be expressed as $L_I = N_{MOT}\, \zeta\, I_{pi}$. Therefore, the number of trapped ions can be described as

$$N_I(t) = N_{MOT}\, \zeta\, \frac{I_{pi}}{\gamma}(1 - e^{-\gamma t}), \tag{5.10}$$

A similar form of equation is used in trapped H_2^+ loading by electro-ionization from background gas as a function of the electron pulse length [20]. Since ions have much higher velocities than the MOT capture velocity for the atoms, ion-atom collisions will lead to loss of atoms from the MOT. This allows the number of MOT atoms lost due to trapped ions N_{MOT}^{loss}, to be written as

$$N_{MOT}^{loss}(t) = N'(1 - e^{-\gamma_{ia}t}), \tag{5.11}$$

where N' is saturation number of atom loss due to ion-atom interaction, and γ_{ia} is the loss rate of the MOT atoms due to ion-atom interactions. The above form of the atom

loss will be validated later, when the experiment and results are presented. The atom loss rate from the MOT is proportional to the number of trapped ions ($N_{MOT}^{loss}(t) \propto N_I(t)$), and so from Eq. (5.10) and (5.11), we conclude that $\gamma \equiv \gamma_{ia}$. Therefore, number of trapped ion as a function of t is expressed as,

$$N_I(t) = N_{MOT} \, \zeta \, \frac{I_{pi}}{\gamma_{ia}}(1 - e^{-\gamma_{ia}t}).$$ (5.12)

The number of trapped ions also depends on I_{pi} but cannot increase indefinitely with I_{pi} due to finite trap depth and volume. Therefore an intensity loss coefficient of trapped ions must be introduced. In the same spirit as the above discussion, to construct a general form of N_I, we write

$$\frac{dN_I(t, I_{pi})}{dI_{pi}} = N_{MOT} \, \zeta \, \frac{1}{\gamma_{ia}}(1 - e^{-\gamma_{ia}t}) - \kappa N_I(t, I_{pi}),$$ (5.13)

where κ is the intensity loss coefficient and has the unit of inverse intensity. The solution of the above equation is, then

$$N_I(t, I_{pi}) = N_{MOT} \, \zeta \, \frac{1}{\gamma_{ia}\kappa}(1 - e^{-\gamma_{ia}t})(1 - e^{-\kappa I_{pi}})$$ (5.14)

The equation can be fully converted into a time dependent function of trapped ions when $I_{pi} \to \infty$ and also fully converted into an I_{pi} dependent function of trapped ions when $t \to \infty$, giving the most general form that describes the dynamics of trapped ions. The number of ions trapped as a function of I_{pi} for $t \to \infty$ is written as

$$N_I(I_{pi}) = N_I^0(1 - e^{-\kappa I_{pi}}).$$ (5.15)

The maximum trapped ion number, N_I^0 when $t \to \infty$ and $I_{pi} \to \infty$ is expressed as,

$$N_I^0 = N_{MOT} \, \zeta \, \frac{1}{\gamma_{ia}\kappa}.$$ (5.16)

Since eqns. (5.15) and (5.16) apply to the ions system in the limit $t \to \infty$, giving a stable number of trapped ions, it is therefore reasonable to expect an average motional energy $\langle E_I \rangle$, for each ion.

5.1.4 Ion-atom collision rate

The ions trapped as described above are assumed to have a speed distribution $f(v)$, consistent with $\langle E_I \rangle$. The laser cooled atoms on the other hand are expected to exhibit a temperature $T_A \approx 100~\mu K$. In this situation $\langle E_I \rangle \gg k_B T_A$ and therefore all of the velocity of the ion-atom collision can be assumed to be possessed by the ion, in the lab frame of reference (LFoR). Similarly, as is shown later, $N_{MOT} \gg N_I^0$ as the ion density ρ_I, is far less that the atom density ρ_A in such mixtures despite the ion trap volume, $V_{IT} \gg V_{MOT}$, the MOT volume in our experiment.

The total ion-atom collision cross-section, σ_{tot} is energy ($E \propto v^2$) dependent and is the sum of the elastic, σ_{el}, and resonant charge exchange, σ_{cx}. $\sigma_{el} \propto 1/E^{1/3}$ over all the energies and $\sigma_{cx} \propto 1/E^{1/2}$ in the low energy regime and $\sigma_{cx} \propto (a \ln E - b)^2$ at high collision energies (a and b are constants) [62]. Given $f(v)$ for the ions, the determination of σ_{tot} rests on assumptions made for $f(v)$. In this case the experimentally relevant quantity to consider is the ion-atom rate coefficient,

$$k_{ia} = \int_v \sigma_{tot}~v~f(v)dv \equiv \langle \sigma_{tot}~v \rangle, \tag{5.17}$$

which represents the velocity averaged product of $\sigma_{tot}v$. A single ion with velocity v_0 and a corresponding ion-atom cross-section σ_{tot}^0 will collide with MOT atoms of density ρ_A at a rate given by

$$z_0 = \sigma_{tot}^0~v_0~\rho_A. \tag{5.18}$$

For the $N_{I;M}$ ions that overlap the MOT at any given time, with a speed distribution $f(v)$, the total ion-atom collision rate then becomes,

$$zN_{I;M} = \langle \sigma_{tot}~v \rangle \rho_A N_{I;M} \equiv k_{ia}~\rho_A~N_{I;M}. \tag{5.19}$$

For a given value of I_{pi}, the number of ions in the ion trap volume V_{IT}, overlapping the MOT volume V_{MOT}, is given by,

$$N_{I;M} = N_I^0(1 - e^{-\kappa I_{pi}})\frac{V_{MOT}}{V_{IT}}. \tag{5.20}$$

Since ion velocities are large, and the MOT capture velocity for the atoms much smaller, ion-atom collisions cause the MOT atoms to eject, allowing us to equate the

total ion-atom collision rate in Eq. (5.19) to $\gamma_{ia}N_{MOT}$, the atom loss rate due to ion-atom collisions. After substituting Eq. (5.20) into Eq. (5.19), the resulting expression for γ_{ia} then becomes,

$$\gamma_{ia} = \frac{N_I^0 k_{ia}}{V_{IT}}(1 - e^{-\kappa I_{pi}}),$$ (5.21)

which defines the relation between the experimentally measurable γ_{ia} and the rate coefficient for ion-atom collisions. In the experimental results that follow, we demonstrate that the above rate equation formulation describes adequately the dependence of the various loss rates with I_{pi}, the BLS intensity.

5.2 Experiments

5.2.1 Experimental Sequence

We now describe the experiment which allows us to validate the above rate equation analysis for ion-atom interaction. The basic time sequence instrumental for results below is shown in Fig. 5.1. The experimental arrangement, techniques, and characterization have been described in detail in the Experimental setup chapter. Rb-atom vapor is created from a dispenser and ^{85}Rb atoms are laser cooled and trapped in a six-beam MOT. The cooling laser is red detuned by $\delta_c = 2\pi \times$ 15 MHz with respect to the $5S_{1/2}(F = 3) \leftrightarrow 5P_{3/2}(F' = 4)$ transition, and the laser power is 3.5 mW per beam. A magnetic gradient field of 12 Gauss/cm is utilized for the MOT. Then we can obtain an atom cloud of rms size 0.35 mm and temperature 166 ($\pm$28)μK.

Here a MOT containing $\approx 1.8(\pm0.06) \times 10^6$ atoms is loaded to saturation in 40 s (T_1 to T_2), and the change in the number of atoms in the MOT is measured under two conditions from T_2 to T_3. In Fig. 5.1(a), we switch ON the ionizing light (BLS) at different intensities. When the BLS ionizes the laser-cooled ^{85}Rb atoms from the MOT and these ions and electrons leave the MOT volume immediately as there is no confinement for them. This results in a depletion of the steady state atom number in the MOT and therefore allows the determination of the ionization rate for the excited atoms. Using Eq. (5.2), data from T_1 to T_2 are fitted to determined γ_{ml}. Solution for
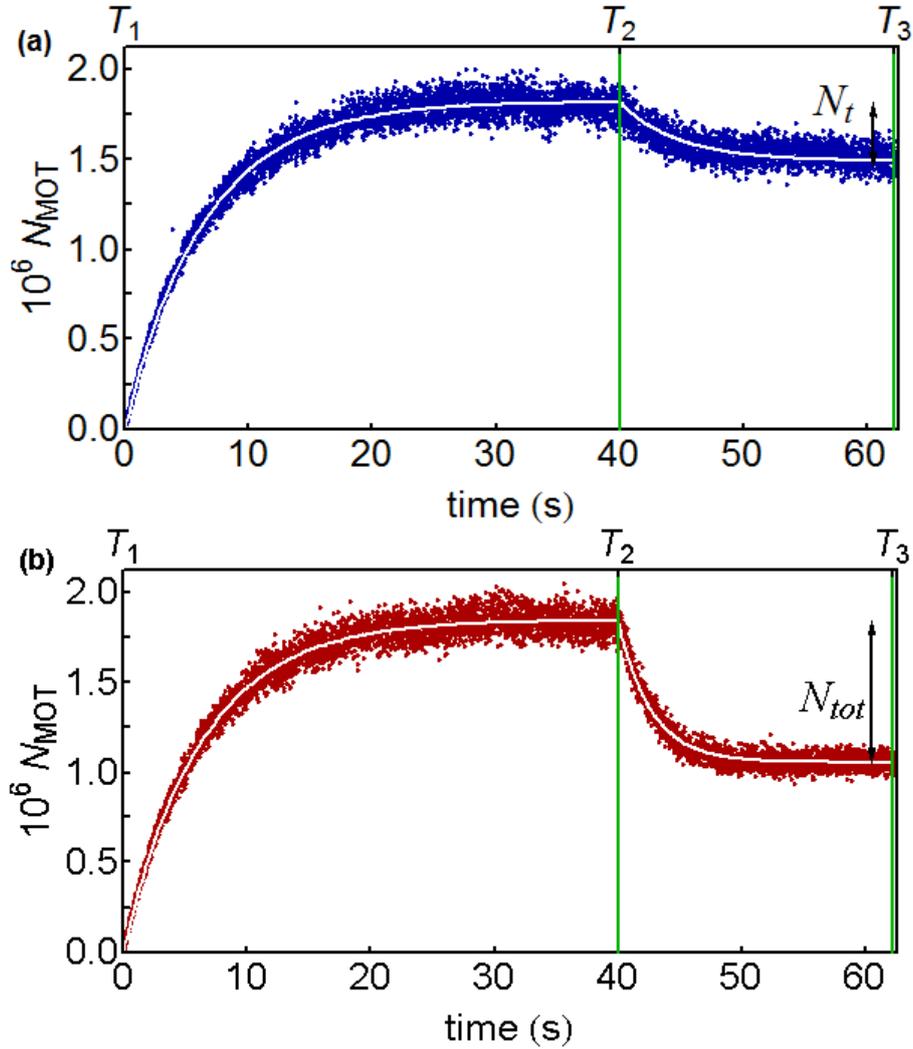
Figure 5.1: The temporal sequence for the experiment: In both panels, first the MOT is loaded for 40 s (from T_1 and T_2) to saturation, where it contains $\approx 1.80 \times 10^6$ atoms. Beyond T_2, the photo ionization light is switched on. Panels (a) and (b) illustrate the evolution of the trapped atoms when the ion trap is OFF and with ion trap ON, respectively. The number of trapped atoms reduces in both cases. However, when the ions and the atoms are simultaneously trapped, the atom loss is much more significant. The plots in (a) and (b) correspond to BLS intensity $I_{pi} = 1.33 \text{ mW/cm}^2$. The various loss rates discussed in the text are determined from such data as a function of photo-ionizing intensity. N_t and N_{tot} are the atom losses due to γ_t and γ_{tot}. The lines show the fits to the data.

Eq. (5.4) with appropriate initial conditions, $N(t = 0) = N_0$ and $N(t \to \infty) = N_0 - N_t$ is

$$N_{MOT}(t) = N_0 - N_t(1 - e^{-\gamma_t t}),\tag{5.22}$$

where N_t is the atom loss due to γ_t during photo ionization. γ_t is determined by fitting data from T_2 to T_3 in Fig. 5.1 (a) with Eq. (5.22). In Fig. 5.1 (b) we switch ON both the ionizing light (BLS) and the ion trap simultaneously. In this case the ionization process is unaffected, but some fraction of the ions created resides within the ion trap, which is well overlapped with the atom trap. Here we observe that the number of trapped atoms reduces significantly over the ionization loss, in the limit of long times of operation of both traps. This loss is attributed to ion-atom interactions. Solution for Eq. (5.7) is obtained in a similar way as photo ionization case and given below.

$$N_{MOT} = N_0 - N_{tot}(1 - e^{-\gamma_{tot} t})\tag{5.23}$$

where N_{tot} is the atom loss due to γ_{tot} when both atoms and ions are simultaneously trapped.

5.2.2 Ionization without trapping

When the BLS is switched ON at T_2, and the ion trap is not operational, the loss rate of atoms from the MOT increases due to ionization of the atoms, which is shown in Fig. 5.2. The measured loss rate coefficient $\gamma_t = \gamma_{ml} + \gamma_{pi}$ can be written using Eq. (5.5) as,

$$\gamma_t = \gamma_{ml} + \zeta I_{pi}\tag{5.24}$$

From Fig. 5.2 it is clear that γ_t has a linear dependence on the intensity of the BLS, I_{pi}. This is because although the ionization process is a two photon process, the operation of the MOT ensures that a constant fraction of atoms are present in the excited state, making the ionization an effective single photon process. The slope of γ_t, ζ is determined to be $0.00225(\pm 0.00022)$ m^2/J from the data. The value of γ_t for $I_{pi} = 0$ is $\gamma_{ml} = 0.144(\pm 0.011)$ s^{-1}.
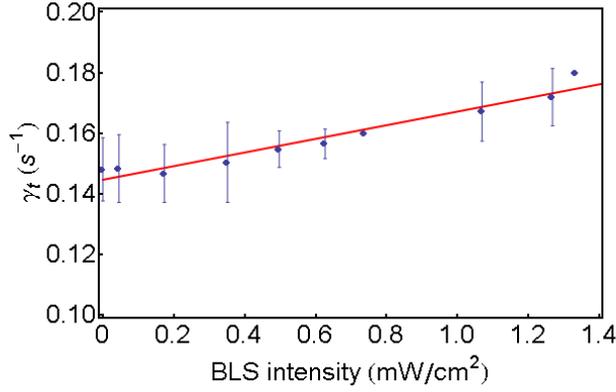
Figure 5.2: The loss rate of atoms from the MOT as a function of photo ionization light intensity, I_{pi}, without the ion trap in Fig. 5.1 (a). As I_{pi} increases, the loss of atoms from the MOT increases as does the rate of loss γ_{pi}. Since this atoms loss is happening on top of the normal loss from the MOT, the experimentally measured quantity here is γ_t. As can be seen from the text, a linear relation is expected between γ_t and I_{pi}, which is measured with a slope of $0.00225(\pm 0.00022)$ m^2/J and the γ_t axis intercept of ≈ 0.14 s^{-1} which is the MOT loss rate without the ionizing light (BLS). Error on the slope from the fit is calculated from confidence level analysis.

5.2.3 Ionization and ion trapping

For the case when ions are held in the ion trap after T$_2$ in Fig. 5.1 (b), loss rate coefficient γ_{tot} varies with a nonlinear behavior as shown in Fig. 5.3. The change in γ_{tot} is fit by a combination of the linear expression in Eq. (5.24) and the exponential form of Eq. (5.21). In order to study the loss rate due to ion-atom interaction, γ_{ia} is plotted separately, as $\gamma_{ia} = \gamma_{tot} - \gamma_t$, in Fig. 5.4. The exponential nature of the γ_{ia} as a function of I_{pi} is evident thus validating the rate equation analysis for the interacting ion-atom system. From the fit to the data Eq. (5.21) becomes, $\gamma_{ia} = 0.218(1 - exp[-0.126\, I_{pi}])$. Identifying $\kappa = 0.126(\pm 0.031)$ in inverse intensity units, i.e. m^2/W and

$$\frac{N_I^0 k_{ia}}{V_{IT}} = 0.218(\pm 0.029) \tag{5.25}$$

with units s^{-1}, we can constrain the product of the trapped ion density and the ion-atom collision rate coefficient.
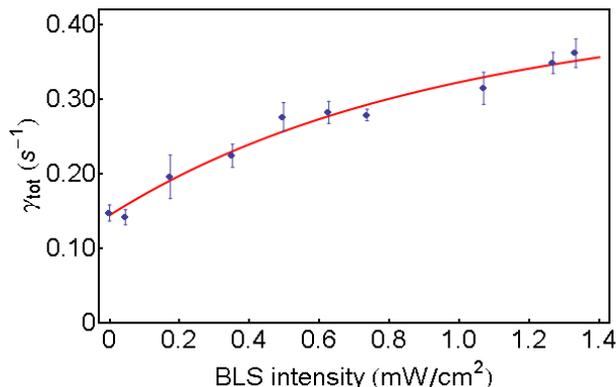
Figure 5.3: The loss rate of atoms from the MOT as a function of ionization light intensity, I_{pi}, with the ion trap in Fig. 5.1 (b). As I_{pi} increases, the loss of atoms occurs on top of the normal loss from the MOT and the ionization loss, and so the experimentally measured quantity here is γ_{tot}. The additional loss of atoms over that in Fig. 5.2 is attributed to the ion-atom interactions for which the loss rate is γ_{ia}. γ_{tot} has exponential and linear components in I_{pi} as is observed.

5.2.4   Direct ion detection

Alongside the measurements on the MOT discussed above, the trapped ions though optically dark in the present experiment, can be measured using a CEM as described in the experimental arrangement. At the end of each ion-atom experiment, the trapped ions are extracted into the CEM, by switching the end cap voltage appropriately. However, since this experiment fills the ion trap to its capacity, severe pile-up results due to overlapping arrival times of the ions onto the detector. For a CEM cone voltage of -2100 V, the extracted ions from the trap as a function of I_{pi} is illustrated in Fig. 5.5. A single exponential dependence of the ion numbers detected with BLS intensity can be expected and a dependence of that nature is seen in the data. However there is detector saturation to contend with and the present measurement of ion numbers is limited by the detection. The direct measurement of the CEM signal is therefore presented for the sake of experimental completeness rather than with the motive of utilizing it to determine the ion-atom interaction rates. For large ion numbers this is likely to remain a significant problem with present day ion detectors. Alternative schemes for ion detections by electrode pickup, Faraday cup detection, etc. [20], may be useful for this
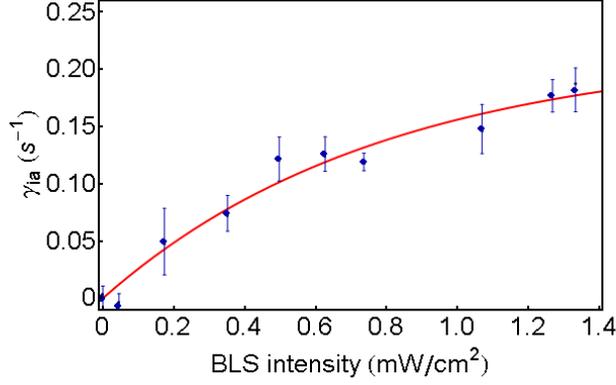
Figure 5.4: (color online) A subtraction of the data in Fig. 5.2 from that in Fig. 5.3 is plotted to isolate the ion-atom interaction term. This loss rate coefficient of the MOT atoms due to ion atom interaction, γ_{ia} is plotted against BLS intensity, I_{pi}. γ_{ia} is fitted with a single exponential function of the form, Eq. (5.21) and the coefficients of the fit are utilized to characterize the interaction term, as discussed in the text.

problem and should be explored.

5.3 Results

5.3.1 Collision rate coefficient determination

We now demonstrate the use of Eq. (5.25), to arrive at the ion-atom collision rate in the present experiment. The values of all the quantities used in the determination of the collision rate, with the standard deviation error in the accompanying parenthesis are provided in the text below. The product of the ion density and k_{ia} is determined from the fit to Eq. (5.21) as $0.218(\pm0.029)$ s^{-1}, so only the determination of the number of trapped ions and the volume of trapping for the ions is required for computation of the collision rate coefficient. Keeping the compromised CEM data in mind, $\kappa = 0.126(\pm0.031)$ m^2/W is determined from the experimental data for atom loss Fig. 5.4, rather than from the data in Fig. 5.5. Using Eq. (5.16), the maximum number of ions which can be accumulated in the ion trap volume is calculated to be $N_I^0 = 1.48(\pm0.43) \times 10^5$.

The volume within which the ions are trapped, V_{IT}, is determined for the present
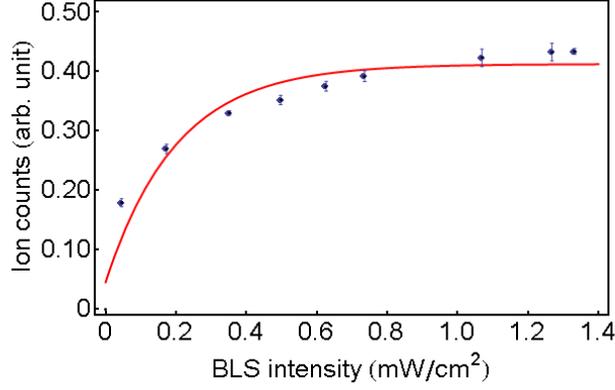
Figure 5.5: (color online) The change in the detected ion counts vs. BLS intensity is shown. Since the number of trapped ions is very large, severe pileup of the ion signal results and the ion signal is seen to saturate faster than measured from the atom signal. The fit is generated using Eq. (5.15).

trap parameters by a combination of trap loss and trap secular frequency measurements. A Monte-Carlo analysis of the time for the loss of ions from the ion trap [8] gives the secular trap depth for trapped ions to be ≈ 0.8 eV. The secular frequencies for the ion trap are $\omega_x = \omega_y = 2\pi \times 135$ kHz, and $\omega_z = 2\pi \times 27$ kHz, which allow us to calculate the trap extent in each direction from the relation $m_I \omega_r^2 r^2 / 2 = 0.8$ eV, where $r \in x_0, y_0, z_0$ is the extremal displacement in each direction and m_I is the mass of the ion. The trapping volume defined by these dimensions for a single ion then is $V_{IT} = 8.33(\pm 0.83) \times 10^{-8}$ m^3.

The collision rate is determined by substituting the mean values of the quantities above in Eq. (5.25), to be

$$k_{ia} = (1.23 \pm 0.42) \times 10^{-13} \ m^3/s. \tag{5.26}$$

The standard deviation error is $\sigma_{k_{ia}} \equiv \sqrt{\sum_i \sigma_i^2} = 0.42 \times 10^{-13}$ m^3/s, where σ_i's are the individual errors for each contributing parameter, shown in Table. 5.1. This demonstrates the technique's ability to arrive at the rate coefficients for ion atom processes, even when the ions are not directly detected. The above rate coefficient is determined when the fraction of atoms in the excited state for $f_e \approx 0.28$, from Eq. 5.3. The measured rate coefficient incorporates the elastic and resonant charge exchange collision

Table 5.1: The key values and errors for the quantities which are used in the determination of k_{ia}

Parameter	Value ($\pm$ error)	Units	Method
ζ	$0.00225(\pm0.00022)$	m²/J	fit from experimental data in Fig. 5.2
N_{MOT}	$1.80(\pm0.06) \times 10^6$	number	fluorescence measurement
V_{IT}	$8.33(\pm0.83) \times 10^{-8}$	m³	derived from secular frequencies and trap depth
N_I^0	$1.48(\pm0.43) \times 10^5$	number	refer Eq. 5.16
$\gamma_{ia}(I_{pi} \to \infty)$	$0.218(\pm0.029)$	s⁻¹	fit from experimental data, in Fig. 5.4
κ	$0.126(\pm0.031)$	m²/W	fit from experimental data, in Fig. 5.4
k_{ia}	$1.23(\pm0.42) \times 10^{-13}$	m³/s	calculated from various quantities given above

from the ground and excited state of the atoms.

5.3.2 Theoretical estimate of the collision rate coefficient

To estimate the collision rate coefficient in Eq. (5.17) we adopt the analytical form of total cross section as a function of collision velocity from [62, 63], using the ground state C_4 value for Rb atoms, 5.26×10^{-39}Cm²/V and 319.5 a.u. [45]. The total cross section comprises of elastic and charge exchange cross section. The semiclassial expression of elastic cross section, σ_{el} in a.u. as a function of the collision energy is

$$\sigma_{el}(E) = \pi(\frac{\mu C_4^2}{\hbar^2})(1 + \frac{\pi^2}{16})E^{-1/3}, \tag{5.27}$$

where μ is the reduced mass of an atom and an ion in a.u. and E is the collision energy. The relation, $\sigma_{el} \propto E^{-1/3}$ is proved in Quantum Mechanics by Landau and Lifshitz [64]. The charge exchange cross section, σ_{cx} in ion-atom collision is a function of energy, E.
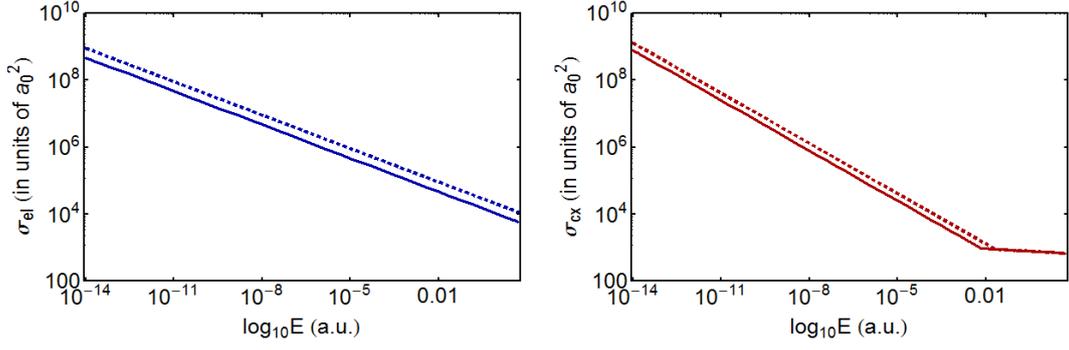
Figure 5.6: Elastic and charge exchange cross sections as a function of collision energy are illustrated in (a) and (b). Solid lines in both figures show the cross section values for the ground state, where $C_4 = 5.26 \times 10^{-39} Cm^2/V$. Dashed lines are for elastic and charge exchange cross section values in the excited state, where static polarizability is $14.15 \times 10^{-39} Cm^2/V$.

At high energies, it has a form of

$$\sigma_{cx} \approx (alnE - b)^2 \tag{5.28}$$

in 10^{-16} cm^2 with $a = 0.377$ and $b = 15.716$, and collision energy is expressed in eV [63]. At low energies below ≈ 0.01 a.u., the charge exchange cross section in a.u. has a form of classical Langevin cross section for a polarization potential and is given below,

$$\sigma_{cx} \approx \pi \sqrt{2C_4} E^{-1/2}. \tag{5.29}$$

In Fig 5.6, we show elastic and charge exchange cross section as a function of collisional energy. The speed distribution of ions in the trap is determined using Monte-Carlo analysis and molecular dynamics simulations [8]. Molecular dynamics simulation realizes ions in the trap interacting in Coulomb potential. It shows that the ion trap can stably trap ions with Maxwell Boltzmann(MB) distribution of temperature $\approx 1000K$, illustrated in Fig. 5.7. In Monte Carlo analysis, a non interacting distribution of ions is evolved with anti-damping factor in the absence of cold atoms in the ion trap potential. Experiment data of ions without contact with MOT as a function of hold time is fitted with a function obtained by the Monte-Carlo analysis [8]. This gives the value of anti-damping factor $\Gamma = 0.57 \times 10^{-25}$ kg s^{-1} and the maximum trappable secular energy ≈ 0.8 eV, corresponding to speed of 1360 m/s. This value matches the tail
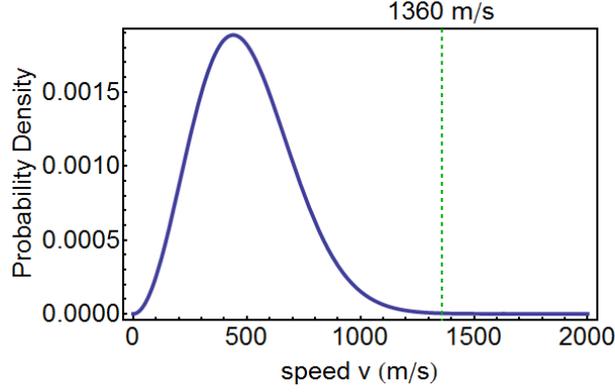
Figure 5.7: Maxwell-Boltzmann speed distribution of temperature $\approx 1000K$ is plotted. The maximum trappable speed corresponding to 0.8 eV matches the tail of the distribution of trapped ions.

of the MB distribution of ions in the trap. Since $V_{IT} \gg V_{MOT}$, and the two traps are well centered, in the overlap region, the micro motion velocity is small. Therefore, in order to estimate the speed distribution of the ions overlapping the MOT, only considering the secular velocity is a good approximation. By performing the integration in Eq. (5.17) with these quantities, we calculate the theoretical value of the rate coefficient as 9.4×10^{-14} m^3/s, when all the Rb atoms are in the ground state. Because atoms in the MOT are constantly pumped to the excited state by the cooling laser, ions invariably collide with the fraction of the MOT atoms, which is are in the excited state atoms. In the experiment, we have 28% of atom population in the excited state ($f_e = 0.28$). The scalar polarizability for a Rb atom in the excited $5P_{3/2}$ state is 14.15×10^{-39} Cm^2/V [45], which is larger than that in the ground state. Incorporating this fraction of atoms in the excited state, f_e, the net collision rate coefficient has the form, $k_{ia} = k_g f_g + k_e f_e$, where k_g and k_e are collision rate coefficient between trapped ions and atoms in ground and excited states respectively, and $f_g = 1 - f_e$ is the atom population in the ground state. We compute the rate coefficient as $k_{ia} = 1.12 \times 10^{-13}$ m^3/s, which agrees well with the experimental value.

5.4   Discussion

The above technique allows the detection of collisional processes between trapped ions and atoms from atomic fluorescence. In the present case, this is successful even for optically dark ions. At its core it relies on the measured changes in the fluorescence of the MOT atoms in the presence of the ions. The present work relies on two important and reasonable premises, which need to be emphasized.

The first is that all ion-atom collisions are two body processes. This is reasonable because of several conditions that exist in the experiment. The atoms in the MOT are non-interacting to a very good approximation. Because the ions are hot, they have large velocities and in this regime the binary ion-atom cross section is small. This is enough to make the presence of another ion in the vicinity of the collision, such that it affects the details of the ion-atom collision, highly improbable. It should be noted though that the experiment and the model are in good agreement, and since the model only incorporates two particle ion-atom collision, it is fair to argue that any more complex process is absorbed within the errors quoted in the present result.

The second premise is that ion-atom collisions knock out a MOT atom. In the experiment here, the only cooling mechanism for the ions is by collision with the cold atoms [8]. The ions are also subject to significant continuous RF heating as their numbers are large and $V_{IT} \gg V_{MOT}$, while the cooling is most effective only at the center of the MOT. Thus the ions are quite hot and therefore possess large velocities. Under such circumstances, even a glancing ion-atom collision, whether elastic or resonant charge exchange, will transfer sufficient energy to the laser cooled atom such that it exceeds the capture velocity of the MOT and gets ejected from the MOT. This then forms the basis for equating the MOT loss rate with the ion-atom collision rate as described above.

Since the majority of ion-atom combination experiments use visible, laser cooled ions, we provide a brief discussion of some major differences. In such cases, since ion temperatures are easily in the mK levels, the ion-atom cross sections are much higher.

The ions then would be crystallized and have a velocity distribution that would be well characterized. How atoms interact with such crystallized ions and what part the long range order of the ions plays in the measurement of the binary ion-atom interaction needs to be carefully understood. A possible problem is that an ion-atom collision at these energies may not result in the ejection of the colliding atom from the MOT and would therefore require Eq. (5.19) to be written with a proportionality constant. However if such an equation can be written, the cross-section could be directly determined because of the well characterized velocity and density distributions of the ions. Obviously, the rate equations constructed above would need to be modified according to the specifics of such a system.

5.5   Conclusion

In a trapped ion and atom mixture, where the atoms are laser cooled and contained in a MOT and the ions are trapped within a Paul trap, we have developed a technique which measures the rate coefficient of ion atom collisions, even when the ions are optically dark. The rate equation formalism has been systematically developed for this experimental system. The experimental results are then fit to the rate equation model, which is seen to provide a consistent and adequate description for the measurements. Analysis of the experimentally measured quantities with the model allows the determination of the trapped Rb^+ ions and Rb atom collision rate coefficient. The value of the rate coefficient compares well with the theoretical estimation and validates the technique.

Collisional dissociation of cold molecules by trapped ions

In the present chapter, we study interaction of photoassociated molecules with trapped ions, in our combined ion and atom trap. The molecules are created by photoassociation (PA) of magneto optically trapped (MOT) atoms, overlap with the trapped Rb ions. We demonstrate that the PA molecules dissociate into free atoms when overlapped with ions. Some of the free atoms are recaptured by the MOT, resulting in enhancement of the MOT fluorescence. Classical harmonic oscillator in the presence of an approaching ion is employed to understand the dissociation mechanism of PA molecules in the presence of trapped ions.

6.1 Photoassociation from the MOT in the presence of trapped ions

In the presence of ionizing light and trapped ions, the loss of atoms from the MOT results from a combination of background gas collision, ionization and ion-atom interaction, γ_{tot}.

$$\frac{dN}{dt} = L - \gamma_{tot} N,$$

The combined loss rate $\gamma_{tot} \equiv \gamma_{ml} N_a / N_a^I$ is measured from fluorescence when ions are photoionized and trapped simultaneously. $N_a^I = L / \gamma_{tot}$ is the saturation number of atoms in the MOT with trapped ions.

The loss rate of MOT atoms due to PA process at excitation energy ϵ_p, when ions are trapped in the ion trap and overlapped with atoms and molecules is denoted by $\tilde{\gamma}_0^I$.
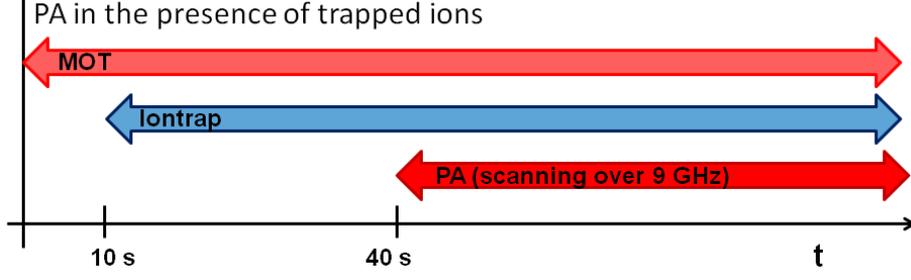
Figure 6.1: Experimental sequence of PA experiment in the presence of trapped ions is illustrated. Once MOT reaches its saturation at t = 10 s, the BLS and iontrap are switched on simultaneously to trap ions. At t = 30 s, MOT and iontrap both reach a steady state. Then PA laser scans over $\approx$ 9 GHz.

The appropriate rate equation then is

$$\frac{dN}{dt} = L - \gamma_{tot}N - \tilde{\gamma}_0^I N, \tag{6.1}$$

where $\tilde{N}_a^I = L/(\gamma_{tot} + \tilde{\gamma}_0^I)$ is the saturated value of the atom number in the presence of PA. Defining $\tilde{\eta}_0^I \equiv \tilde{N}_a^I/N_a^I$, we obtain

$$\tilde{\eta}_0^I = \frac{\tilde{N}_a^I}{N_a^I} = \frac{\gamma_{tot}}{\gamma_{tot} + \tilde{\gamma}_0^I}, \tag{6.2}$$

6.2 Experimental sequence

An experimental setup for photoassociation is described in detail in chapter 3. The setup fulfills the requirements to investigate the interaction of ions with ultra-cold molecules. It has simultaneous and overlapped traps for ions and atoms, and efficient production of molecules from cold atoms in the steady state of each ingredient. We go through it briefly. A six beam MOT of ^{85}Rb is realized within the linear Paul trap. When the MOT is vapor loaded and reaches the saturation, it contains $2.87(\pm0.08) \times 10^6$ atoms within a volume $V_a = 1.44(\pm0.05) \times 10^{-9}$ m^3 at a temperature $T_a \approx 150$ μK and a MOT loss rate of $\gamma_{ml} = 0.148$ s^{-1}. The ion trap quadrupole rods are subjected to a radio-frequency (rf) field of frequency 600 kHz and amplitude $V_{rf} = 91.7$ V, while the end cap electrodes are maintained at $V_{ec} = +80$ V. The ^{85}Rb$^+$ ions are created by photo-ionizing the Rb MOT atoms in the excited state, using a blue light source (BLS). These

ions have negligible kinetic energy and are created at the bottom of the ion trap secular potential,then ion cloud gets expanded due to Coulomb repulsion and heated to the temperature $T_i \approx 1000$ K. $N_i \approx 1.74(\pm 0.52) \times 10^5$ ions are estimated to be present when iontrap is filled to its maximum. Volume of iontrap is $\approx 8.33 \times 10^{-8}$ m^3 [57]. The MOT atom density is much greater than the density of the trapped ions, i.e. $n_a \gg n_i$, ensuring that the MOT is encompassed by the trapped ions. The direct imaging of atomic fluorescence from the MOT atoms allow determination of the spatial distribution of atoms and the atom number is measured from MOT fluorescence, using a carefully calibrated spatial filtering arrangement and photo multiplier tube (PMT) combination. The experimental method is discussed in detail in the earlier chapters 3 and 5. A laser light is prepared for the photoassociation of cold atoms using an external cavity diode laser (ECDL) and a taper amplifier (TA). The ECDL is set to give a frequency of ≈ 60 GHz red-detuned from the Rb atomic resonance, and tunable over ≈ 8 GHz at ≈ 44 MHz/s. This red-detuned light is fed to the TA for high intensity. About 160 mW of power is used for PA. The creation of bound molecules from the atoms results in an PA photon energy ϵ_p specific loss of fluorescence from the MOT, corresponding to specific vibrational level in the molecular state.

6.3   Determination of a loss rate of atoms in the MOT due to PA in the presence of trapped ions

When ions are trapped simultaneously with the MOT, the MOT atom number with the trapped ions $\tilde{N}_a^I$, is less than N_a due to BLS ionization of the excited atoms and ion-atom collisions [57], while V_a remains unchanged. The increased MOT atoms loss rate due to the presence of ions is $\gamma_{tot} = \gamma_{ml} N_a / N_a^I$. In this mixture, the PA measurements are made such that $n_a^I > n_a^c$. As we can see in Fig. 6.2, across all frequencies the fluorescence depletion in the presence of a filled ion trap, $\tilde{\eta}_0^I(\epsilon_L) \leq \tilde{\eta}(\epsilon_L)$, where the equality holds only when there is no molecular resonance. In Fig. 6.3, we see the variation of $\tilde{\eta}_0^I(\epsilon_p)$ as a function of ionizing light intensity, which is at $\approx 60\%$ when
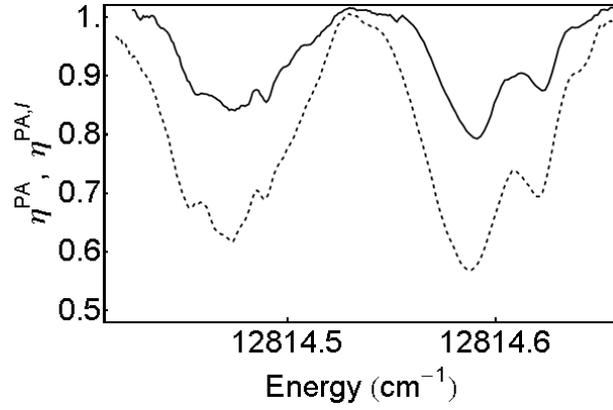
Figure 6.2: Figure illustrates the change in the fraction of MOT atoms lost due to PA as a function of PA laser frequency in the presence and absence of trapped ions, shown in blue (N_{pa}/N_{at}) and dashed (N_{pa}^I/N_{at}^I) lines respectively.
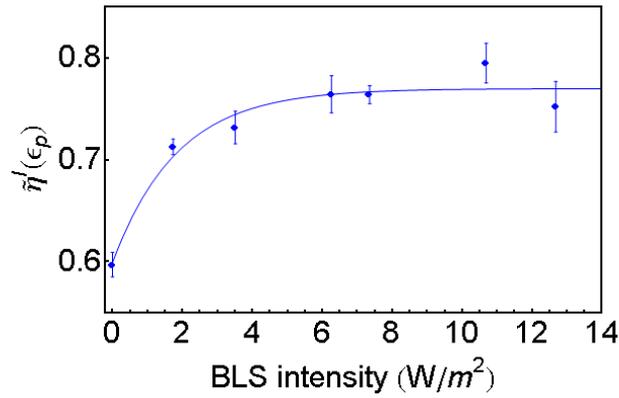
Figure 6.3: Figure shows the fractional increase in MOT fluorescence at ϵ_p as a function of BLS intensity, which is proportional to ion loading rate into the ion trap.

there are no ions and goes to between 75% to 80% as the ionizing light increases. From the Eq. 6.2, we get the PA loss rate of MOT atoms in the presence of ions is given by $\tilde{\gamma}_0^I = 0.081 \pm (0.009)\text{ s}^{-1}$.

6.4   Ion-molecule interaction

The enhancement of the relative MOT fluorescence in PA with trapped ions (Fig. 6.2 and 6.3) is due to a fraction of the dissociated molecules returning to the MOT. Since these are created in ion-molecule collisions, the extra atom signal can be used to obtain the ion molecule collision rate coefficient leading to atom recapture, k_{im}^r, which is written as

$$2k_{im}^r = (\tilde{\gamma}_0 - \tilde{\gamma}_0^I)/n_i, \tag{6.3}$$

where $n_i = 2.09(\pm 0.66) \times 10^{12}\text{ m}^{-3}$. The factor of two accounts for two atoms that are created from each dissociation, which is symmetric. At ϵ_p, for BLS intensitiy = 10.4 W/m^2, substituting the values of $\tilde{\gamma}_0$ and $\tilde{\gamma}_0^I$, we obtain $k_{im}^r = 9.17(\pm 2.90) \times 10^{-15}\text{ m}^3/\text{s}$. Values for k_{im}^r obtained from other points in Fig. 6.3 give similar values. However, k_{im}^r at 10.4 W/m^2 has the best overall quality of data.

Clearly, k_{im}^r is a resonance specific quantity and needs to be determined over the entire spectrum. The crucial importance of the above measurement is that the ion-molecule dissociative process is comparable to the ion-atom collision processes [57], which have been the focus of recent studies. The ion-molecule system is the obvious and significant next step in these systems, as it opens the possibilities for dilute gas chemistry and astrochemistry. In the following discussion we illustrate the basic mechanism for the ion-molecule dissociative collision by constructing a model and comparing its results with our experimentally measured values.

The spectral features of the photoassociated molecules in the presence of ions are identical to that of PA without ions. The excited molecules are $\approx$ 5 nm long and the states are $\approx$ 60 GHz detuned, from the dissociation continuum. These states decay by spontaneous emission to the ground bound molecular states γ_b and free contin-
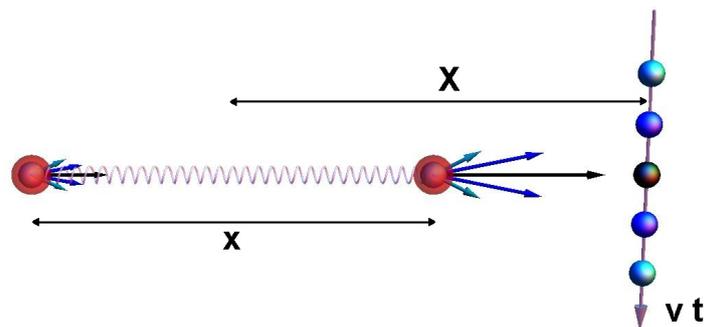
Figure 6.4: Toy model figure shows the effect of the passage of the ion in the vicinity of the molecule. The two atoms experience a different forces as they polarize independently under the influence of the ion. This results in an overall differential force along the molecular bond, which enables vibrational excitation of the molecule.

uum states γ_f and stimulated emission. Details are provide in Fig. 3.29. All these processes originate from the excited states, so the rate determining factor for any observed change in the molecular signal is associated with the population of excited state molecules. For such molecules, inelastic ion-molecule collisions ($\sigma_{im}(v)$), can excite the molecule by vibrational energy transfer, into higher vibrational levels or the dissociation continuum. As the energy transfer required to excite the molecule into the dissociation continuum is very modest compared to the collision energy, the process can be highly probable [65].

6.5   Classical calculation of vibrational energy transfer

Photoassociation of cold atoms creates molecules in very high vibrational states with very slow rotation. In our problem, since the ions are fast, it will see and interact with the completely stretched molecule and the maximum contribution to dissociation will come from around the classical outer turning point. These long range molecules have properties which are closely related to the properties of the constituent atoms in the asymptotic electronic state [64]. This allows us to use classical calculation of vibrational energy transfer to a diatomic molecule as a classical harmonic oscillator.

A Rb_2 in 5s $^2S_{1/2}$ + 5p $^2P_{3/2}$ is considered as an harmonic oscillator, having an
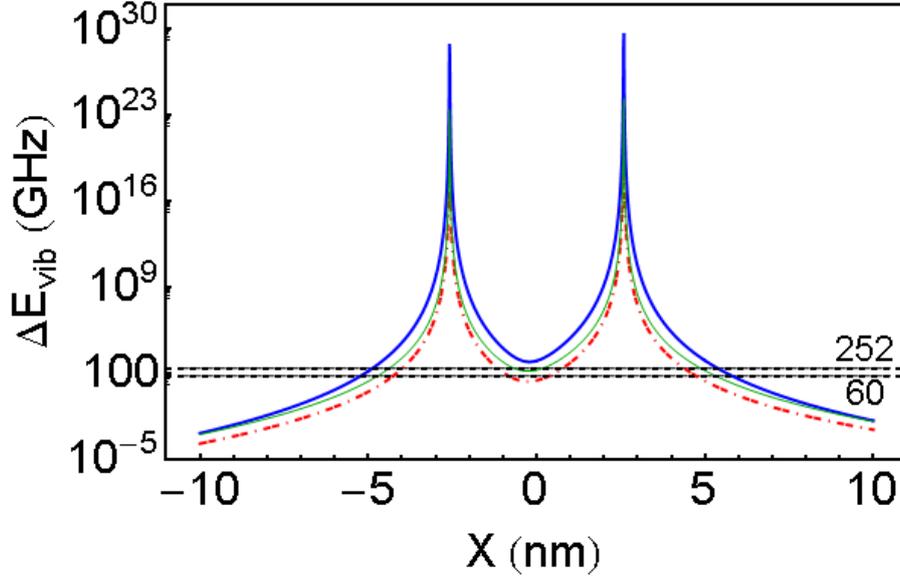
Figure 6.5: In (b) we see the variation of the vibrational energy transferred to the molecule as a function of X, plotted for ion velocities of 1, 500 and 1360 m/s in blue, green and dashed red lines.

equation of motion $\mu d^2 x / dt^2 + k(x - x_0) = F(t)$, where an external force $F(t)$ due to an ion at distance X, moving with velocity vt along y axis is considered, as shown in Fig 6.4. In this case, the vibrational energy transfer to the oscillator due to the collision is

$$\Delta E_{vib} = \frac{1}{2} \mu \omega^2 \left| \frac{1}{\mu \omega} \int_{-\infty}^{\infty} F(t) exp(i\omega t) dt \right|^2 , \tag{6.4}$$

where $\omega = \sqrt{k/\mu}$, angular frequency of the oscillator. We calculate ΔE_{vib} from Eq. 6.4 by inserting $F(t)$ which is derived from the ion-molecule interaction potential $V_c(x,t)$ given by,

$$V_c(x,t) = -\frac{e^2 \alpha_g}{2(4\pi\epsilon_0)^2} \frac{1}{((X + x/2)^2 + (vt)^2)^2} - \frac{e^2 \alpha_e}{2(4\pi\epsilon_0)^2} \frac{1}{((X - x/2)^2 + (vt)^2)^2}, \tag{6.5}$$

where x is internuclear separation of Rb_2 and α_g and α_e are the ground and excited state polarizabilities.

Fig. 6.5 shows ΔE_{vib} as a function of X, distance of an ion from the centre of mass (CM) for ion velocities of 1, 500 and 1360 m/s. When ΔE_{vib} is greater than the vibrational dissociation barrier ≈ 60 GHz, the molecule dissociates into two free atoms. The value of X capable of dissociating the molecule changes with the ion velocity. If the velocity

of the dissociating atoms is smaller than the MOT capture velocity $v_c \approx 30$ m/s (corresponding to an energy for 2 Rb atoms ≈ 252 GHz), then the atoms are recaptured by the MOT and result in increased relative fluorescence, as seen in the experiment. This means molecules having 60 GHz $< \Delta E_{vib} < 252$ GHz are dissociated into free atoms within MOT capture velocity.

The classical ion molecule cross sections at various ion velocities for inelastic excitation between $60 < \Delta E_{vib} < 252$ GHz are calculated, and the range of values for X's that satisfy the excitation is determined. The ion-molecule collision induced atom recapture rate coefficient, k_{im}^T is given by,

$$k_{im}^T = \int_0^\infty \sigma_{im}^T(v) v f(v) dv, \tag{6.6}$$

where $\sigma_{im}^T(v)$ is the geometric cross section derived from the X values and $f(v)$ is the Maxwell-Boltzmann velocity distribution consistent with 1000 K for Rb$^+$ ions. Estimating the inelastic cross section for molecular vibrational excitation from the range derived above, we compute the theoretical inelastic ion-molecule collision rate coefficient in the atom recapture window, as $k_{im}^T = 5.69 \times 10^{-15}$ m^3/s. Table with key experimental values and errors is given in Table. 6.1.

6.6 Conclusion

We have investigated the interaction of relatively fast moving ions with translationally very cold, but vibrationally very hot molecules. Enhanced atomic fluorescence, attributed to the dissociation of molecules in collision with ions is observed. A model, which has previously been successful in calculating vibrational energy changes for colliding molecules has been adapted for the present work and provides an intutive understanding of molecular dissociation. Inelastic collision rates from the experiment and the model agree fairly well. These experiments create conditions similar to those prevalent in upper atmosphere and outer space, with the advantage that these can be prepared specifically to tune into the phenomenon of interest. The study of sequential but infrequent processes are possible because of the very long hold and interrogation

Table 6.1: The key values and errors for the quantities which are used in the determination of k_{im}^r for BLS intensity 10.7 W/m^2. Errors in γ_{ml} and w are not incorporated for the * error values

.

Parameter	Value ($\pm$ error)	Units	Method and Description
γ_{ml}	$0.148(\pm0.011)$	s^{-1}	measurement: MOT loss rate
γ_{tot}	$0.240(\pm0.007^*)$	s^{-1}	measurement: MOT loss rate
N_a	$2.871(\pm0.076) \times 10^6$	number	measurement: fluorescence
V_a	$1.437(\pm0.048) \times 10^{-9}$	m^3	measurement: direct imaging of MOT atoms
n_a	$1.998(\pm0.085) \times 10^{15}$	m^{-3}	calculated from N_a and V_a
N_i	$1.740(\pm0.518) \times 10^5$	number	refer [57]
n_i	$2.089(\pm0.655) \times 10^{12}$	m^{-3}	calculation from N_i, refer [57]
w	$0.765(\pm0.012)$	-	measured: fractional overlap of PA laser beam to the MOT volume
$\tilde{\eta}(\epsilon_p)$	$0.619(\pm0.021)$	-	measured: MOT fluorescence
$\tilde{\eta}^I(\epsilon_p)$	$0.795(\pm0.020)$	-	measured: MOT fluorescence
$\tilde{\gamma}_0$	$0.119(\pm0.010^*)$	s^{-1}	calculated from Eq. 3.37
$\tilde{\gamma}_0^I$	$0.081(\pm0.009^*)$	s^{-1}	calculated from Eq. 6.2
k_{im}^r	$9.171(\pm2.903^*) \times 10^{-15}$	m^3/s	calculated from Eq. 6.3

times. Densities here are high enough for processes to be frequent and can be controlled to prevent unwanted processes.

Conclusions

7.1   Summary of the major results

This thesis comprises extensive numerical and experimental studies, with occasional theoretical development. The basic focus is the understanding of ion-atom and ion-molecule systems in combined traps. To achieve this, the following results have been obtained.

We have proposed and designed a novel ion trap configuration that, by symmetry, three-dimensionally frequency degenerate. The basic trap configuration can be extended to an array of ion traps by stacking it together. That gives a structure of a lattice of ion traps (LIT). We have characterized the basic and the LIT, and compared them to illustrate the robustness of the LIT. Practical implementations such as loading and optical detection schemes of ions in the trap are described. Possible application of this in precision spectroscopy, quantum information processing and the study of few-particle interacting systems are discussed.

In the MOT, atom loading and loss rates due to collisions with background gases are measured from the MOT flurescence to study the dynamics of trapped atoms. We performed a trap oscillation method to estimate the temperature of the atom cloud. Independently, an extensive characterization of the ion trap in the combined trap is carried out. In this characterization, Rb^+ ions are destructively detected as they are inaccessbile for optical detection. The motional resonance of Rb^+ ions and stability of ions under various ν_{rf} and V_{rf} for the ion trap are found. We have developed a molecular dynamics simulation for interacting charged particles, in which the equations of motion are numerically integrated using leap frog method. It helped in understanding of the dynamics of optically dark ions in the trapping potential and in the extraction potential. Using this simulation, the temperature of the trapped ions and the time of

flight are estimated.

Having finished with the characterizations of both MOT and ion trap, we have moved to the next step, i.e. investigation of ion-atom interaction. Loss rates due to photoionization (PI) of excited atoms and ion-atom interaction have been measured by tracking the MOT fluorescence. An analytical form of loss rate due to ion-atom interactions has been formulated in terms of trapped ion density and ion-atom collision rate coefficient. From this loss rate, we have estimated experimentally measured ion-atom collision rate coefficient and compared with the theoretically estimated value.

We have constructed an experimental arrangement for photoassociation, in which an external cavity diode laser and a tapered amplifier are combined to give 8 GHz scanning with 60 GHz red-detuned from the atomic resonance at 160 mW of power. Using this setup, we have obtained the photon energy dependent depletion of fluorescence due to PA, and identified each dip to corresponding vibrational levels in the excited molecular state. The loss rate of atoms due to PA is measured at the photon energy $\epsilon_p = 12814.59 \, \text{cm}^{-1}$.

To investigate ion-cold molecule, we have measured loss rates of MOT atoms due to PA in the presence and absence of trapped ions at ϵ_p. From these loss rates, dissociation rate coefficient of a Rb_2 molecule due to a trapped ion is estimated in the atom recapture window. This process is modelled using a semi-classical approach with the dissociation dynamics. The experimental measurement obtained is in reasonable agreement with the model.

7.2   Perspectives and future challenges

This study can be extended to manufacture Rb_2^+ molecular ion by photoassociating Rb atom and Rb^+ ion, giving a possiblility to create various species of molecules and molecular ions. To achieve this, we need suitable ion trap operating parameters. The stability diagram can be plotted for maximum trappable initial velocity of Rb_2^+ ions as a function of V_{rf} at a particular ν_{rf}. This numerical studies give a trap depth ex-

perience by a Rb$_2^+$ in the trapping potential. Multi-species collision experiments can give a comparison between the resonant and non resonant charge-exchange collisions. An interesting combination of such an experiment can be ^{85}Rb$^+$ ions and ^{87}Rb atoms, in which non-resonant charge exchange collisions occurs while having almost equal masses. This can show the effect of resonant charge exchange collision in collisional cooling of ions in contact with cold atoms. Classical calculation of the vibrational energy transfer from an ion to a molecule can be improved by incorporating the anharmonicity of the molecular potential, basically taking a semi-classical approach. This would be numerically simple to implement and give a reasonably good understanding in ion-molecule collisions.

Constants and units

Atomic units form a system of natural units which is convenient for atomic physics calculations. In atomic units, the numerical values of four fundamental physical constants (m_e, e, $\hbar$ and $1/4\pi\epsilon_0$) are all unity by definition. Tables of fundamental atomic units, related physical constants and energy conversion are given below.

Table A.1: Fundamental constants defining atomic units (a.u.)

Quantity	Value in SI	Value in a.u.
Electron mass m_e	9.109×10^{31} kg	1
Planck constant h	6.626×10^{-34} J/s	2π
Electron charge e	1.602×10^{-19} C	1
Coulomb's constant $1/4\pi\epsilon_0$	8.988×10^9 m/F	1

Table A.2: A list of the physical constants in a.u.

Quantity	Value in SI	Value in a.u.
Bohr radius a_0	0.529×10^{-10} m	$\hbar^2 m_e^{-2}$
Hartree E_h	4.360×10^{-18} J	$\hbar^2 a_0^{-2} m_e^{-1}$
Neutron mass m_n	1.675×10^{-27} kg	$1838.685\ m_e$
Polarizability α	1 C^{2}m^2/J	$6.065 \times 10^{40} e^2 a_0^4 m_e \hbar^{-2}$
Frequency f	1 Hz	$2.419 \times 10^{-17} \hbar a_0^{-2} m_e^{-1}$
Speed of light $c = v_B/\alpha$	2.998×10^8 m/s	137.036
Velocity v_B	2.419×10^{-17} m/s	$e^2 (4\pi\epsilon_0)^{-1} \hbar^{-1}$

Table A.3: Energy conversion table

	E_h	eV	cm^{-1}	Hz	K	J
E_h	1	2.721×10^1	2.195×10^5	6.580×10^{15}	3.158×10^5	4.360×10^{-18}
eV	3.675×10^{-2}	1	8.066×10^3	2.418×10^{14}	1.160×10^4	1.602×10^{-19}
cm^{-1}	4.556×10^{-6}	1.240×10^{-4}	1	3.000×10^{10}	1.439	1.986×10^{-23}
Hz	1.520×10^{-16}	4.136×10^{-15}	3.336×10^{-11}	1	4.799×10^{-11}	6.626×10^{-34}
K	3.167×10^{-6}	8.617×10^{-5}	6.950×10^{-1}	2.084×10^{10}	1	1.381×10^{-23}
J	2.294×10^{17}	6.242×10^{18}	5.034×10^{22}	1.509×10^{33}	7.243×10^{22}	1

Adaptation of Virial theorem for potential of inhomogeneous function

We discuss a possible way of applying Virial theorem for potentials of inhomogeneous function. Consider a system in which ions are interacting via Coulomb potential in an iontrap of harmonic oscillator potential form. The total potential energy, U in this case is

$$U = V^C + V^{HO}, \tag{B.1}$$

where V^C and V^{HO} are Coulomb and harmonic oscillator potential energies respectively. According to the Virial theorem, if the potential energy is a homogeneous function, $\bar{U}_h$ of degree k in the coordinate and the motion takes place in a finite region, then there is a simple relation between the time average values of the kinetic and potential energies, $\bar{T}_k$ and $\bar{U}_h$, given as

$$2\bar{T}_k = k\bar{U}_h \tag{B.2}$$

In our case, the potential energy is not a homogenous function. We cannot simply apply the relation for the homogeneous equation. Let us find a relation between the kinetic energy, T_k and the potential energy, U of a non-homogeneous functional form. The kinetic energy T_k is a quadratic function of the velocities [66]. By Euler's theorem, we have

$$
\begin{aligned}
2T_k &= \sum \mathbf{v}_a \cdot \partial T/\partial \mathbf{v}_a = \sum_a \mathbf{p}_a \cdot \mathbf{v}_a, \\
&= \frac{d}{dt}\left(\sum_a \mathbf{p}_a \cdot \mathbf{r}_a\right) - \sum_a \mathbf{r} \cdot \dot{\mathbf{p}}_a,
\end{aligned} \tag{B.3}
$$

where $\partial T/\partial \mathbf{v}_a = \mathbf{p}_a$, the momentum.

The time average value of a function, $f(t)$ is

$$\bar{f} = \lim_{\tau \to \infty} \frac{1}{\tau} \int_0^\tau f(t)dt. \tag{B.4}$$

Time average of $f(t)$ is zero if $f(t)$ is the time derivative $\mathrm{d}F(t)/\mathrm{d}t$ of a bounded function $F(t)$. For the system that executes a motion in a finite space and with finite velocities, $\sum \mathbf{p}_a \cdot \mathbf{r}_a$ is bound. Therefore $\overline{\sum \mathbf{p}_a \cdot \mathbf{r}_a} = 0$. $\dot{\mathbf{p}}_a$ in the second term in the last line of Eq. B.3 is the force, which is $\partial U/\partial \mathbf{r}_a$ [66]. Then we get,

$$2\overline{T_k} = \overline{\sum_a \mathbf{r}_a \cdot \frac{\partial U}{\partial \mathbf{r}_a}}. \tag{B.5}$$

First, $\sum_a \mathbf{r}_a \frac{\partial U}{\partial \mathbf{r}_a}$ is simplified putting Eq. B.1.

$$\sum_a \mathbf{r}_a \cdot \frac{\partial U}{\partial \mathbf{r}_a} = \sum_{a,b,a>b} \mathbf{r}_a \cdot \frac{\partial V_{ab}^C}{\partial \mathbf{r}_a} + \sum_{a,b,a<b} \mathbf{r}_a \cdot \frac{\partial V_{ab}^C}{\partial \mathbf{r}_a} + \sum_a \mathbf{r}_a \cdot \frac{\partial V_a^{HO}}{\partial \mathbf{r}_a}$$

$$= \sum_{a,b;a>b} \mathbf{r}_a \cdot \frac{\partial}{\partial \mathbf{r}_a} \left(k_c \frac{Q_a Q_b}{|\mathbf{r}_a - \mathbf{r}_b|} \right) + \sum_{a,b;a<b} \mathbf{r}_a \cdot \frac{\partial}{\partial \mathbf{r}_a} \left(k_c \frac{Q_a Q_b}{|\mathbf{r}_a - \mathbf{r}_b|} \right) + \sum_a \mathbf{r}_a \cdot \frac{\partial}{\partial \mathbf{r}_a} \left(\frac{1}{2} M\omega^2 \mathbf{r}_a^2 \right)$$

$$= \sum_{a,b;a>b} \mathbf{r}_a \cdot \frac{\partial}{\partial \mathbf{r}_a} \left(k_c \frac{Q_a Q_b}{|\mathbf{r}_a - \mathbf{r}_b|} \right) + \sum_{a,b;a>b} \mathbf{r}_b \cdot \frac{\partial}{\partial \mathbf{r}_b} \left(k_c \frac{Q_a Q_b}{|\mathbf{r}_a - \mathbf{r}_b|} \right) + \sum_a \mathbf{r}_a \cdot M\omega^2 \mathbf{r}_a, \tag{B.6}$$

where $k_c = \frac{1}{4\pi\epsilon_0} = 9 \times 10^9$ m/F and Q_a is the charge on ath particle. Index of the second term is changed from a to b to make the range of the summation same as that in the first term and

$$\sum_{a,b;a>b} \mathbf{r}_a \cdot \frac{\partial}{\partial \mathbf{r}_a} \left(k_c \frac{Q_a Q_b}{|\mathbf{r}_a - \mathbf{r}_b|} \right) = - \sum_{a,b;a>b} \mathbf{r}_b \cdot \frac{\partial}{\partial \mathbf{r}_b} \left(k_c \frac{Q_a Q_b}{|\mathbf{r}_a - \mathbf{r}_b|} \right).$$

Therefore, Eq. B.6 becomes,

$$= \sum_{a,b;a>b} (\mathbf{r}_a - \mathbf{r}_b) \cdot \frac{\partial}{\partial \mathbf{r}_a} \left(k_c \frac{Q_a Q_b}{|\mathbf{r}_a - \mathbf{r}_b|} \right) + \sum_a M\omega^2 |\mathbf{r}_a|^2$$

$$= \sum_{a,b;a>b} (\mathbf{r}_a - \mathbf{r}_b) \cdot \left\{ -k_c \frac{Q_a Q_b}{|\mathbf{r}_a - \mathbf{r}_b|^3} (\mathbf{r}_a - \mathbf{r}_b) \right\} + \sum_a M\omega^2 |\mathbf{r}_a|^2$$

$$= - \sum_{a,b;a>b} k_c \frac{Q_a Q_b}{|\mathbf{r}_a - \mathbf{r}_b|} + \sum_a M\omega^2 |\mathbf{r}_a|^2$$

$$= - \sum_{a,b;a>b} V_{ab}^C + 2 \sum_a V_a^{HO}$$

$$= -V^C + 2V^{HO}. \tag{B.7}$$

Applying the time average integration on the Eq. B.7 and equating with Eq. B.5, we get

$$2\overline{T_k} = \overline{-V^C + 2V^{HO}}. \tag{B.8}$$

For dilute gases, $\overline{V^C} \approx 0$ then we have

$$\overline{T_k} = \overline{V^{HO}}. \tag{B.9}$$

where the mean values of the kinetic and potential energies are equal.

Classical calculation of scattering angle and cross section in the polarization potential

The polarizability, α of an atom or molecule describes the dynamical response of the electron cloud to an external electric field. For ion-atom/molecule scattering/reaction, the nature of the interaction has the inverse-fourth-power potential of the form,

$$V_p(r) = -\frac{\alpha Q^2}{2(4\pi\epsilon_0)^2 r^4},\tag{C.1}$$

where Q is the ionic charge. The scattering angle Θ in the centre of mass frame for the polarization potential (see Fig. C.1) is expressed as

$$\Theta = \pi - 2\Phi = \pi - 2\int_0^{\rho_0} \frac{d\rho}{\sqrt{1 - \rho^2 + \frac{Q^2 \alpha \rho^4}{M_r v_0^2 b^4}}},\tag{C.2}$$

where Φ is the angle corresponding to the distance of closest approach, b is the impact parameter, M_r and v_0 are the mass and the initial velocity of the ion, $\rho = b/r$, and $\rho_0 = b/D_{12}$. D_{12} is the sum of the radii of the ion and molecule (considered to be spherical). The orbit of a particle moving in polarization potential can be classified as spiraling or deflecting. For b less than b_c, the particles spiral into a circular orbit. b_c is known as a critical impact parameter and is given as,

$$b_c = \left(\frac{4Q^2\alpha}{(4\pi\epsilon_0)^2 M_r v_0^2}\right)^{1/4},\tag{C.3}$$

i.e. when the denominator of Φ equals zero. But $b_c < D_{12}$, which means the ion can approach the atom/molecule beyond b_c. Calculation of Φ for $b \leq b_c$ is not trivial as the integrand has a singularity at $b = b_c$ and turns imaginary for values of $b < b_c$. We have
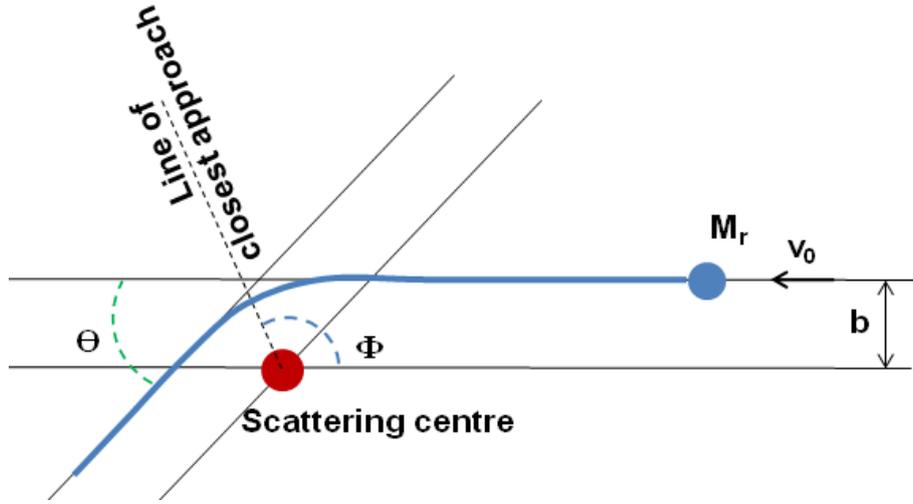
Figure C.1: The one body scattering, dynamically equivalent to the two body scattering is illustrated. M_r is scattered through an angle, Θ whose value is calculated in Eq. C.2.

two different methods to calculate Φ for $b > b_c$ and $b \leq b_c$. The first case follows the usual integration with ρ_0, being the lower of the two positive roots of the polynomial in the denominator, if roots exits. If this polynomial does not have any real root, the integration falls into the second case. Before moving to the second case, let's define few variables for further calculation.

$$z^2 = \frac{M_r v_0^2}{2k_B T} \tag{C.4}$$

$$\mu = \sqrt{\frac{\alpha}{2(4\pi\epsilon_0)^2 k_B T}} \frac{Q}{D_{12}^2} \tag{C.5}$$

$$\beta = \frac{b\sqrt{z}}{2} \left[\frac{\alpha Q^2}{2(4\pi\epsilon_0)^2 k_B T} \right]^{-1/4}, \tag{C.6}$$

where T, temperature is defined as $\frac{1}{2} M_r \bar{v}_0^2 = \frac{3k_B T}{2}$ and $\bar{v}_0^2$ is the mean square value of v_0. In the second case, we need to transform the integration by putting,

$$\rho = y\sqrt{2\beta^2}, \tag{C.7}$$

then we get

$$\Phi = \sqrt{2\beta^2} \int_0^{y^*} \frac{dy}{\sqrt{1 - 2\beta^2 y^2 + y^4}}, \tag{C.8}$$

where $y^* = \sqrt{\mu/z}$. Applying few tricks for solving above integration where value of the polynomial in the denominator is less than one, we get the following table to

119

calculations:

- If $\beta < 1$ and $\mu < 1$,

$$2\Phi = \sqrt{2\beta^2} \int_0^{\sqrt{\mu/z}} \frac{dy}{\sqrt{1 - 2\beta^2 y^2 + y^4}} \tag{C.9}$$

- If $\beta < 1$ and $\mu > 1$,

$$2\Phi = \sqrt{2\beta^2} \left(2 \int_0^1 \frac{dy}{\sqrt{1 - 2\beta^2 y^2 + y^4}} + \int_0^{\sqrt{z/\mu}} \frac{dy}{\sqrt{1 - 2\beta^2 y^2 + y^4}} \right) \tag{C.10}$$

To calculate the cross section, σ for each velocity, we have

$$\sigma(v_0) = \int \cos^2 \Phi b \, db = \frac{\mu D_{12}^2}{2} \int \cos^2 \Phi d\beta^2 \tag{C.11}$$

Bibliography

[1] W. W. Smith, O. P. Makarov, and J. Lin. Cold ion neutral collisions in a hybrid trap. *Journal of Modern Optics*, 52:2253, 2005.

[2] C. Zipkes, S. Palzer, C. Sias, and M. Köhl. A trapped single ion inside a bose-einstein condensate. *Nature*, 464:388, 2010.

[3] S. Schmid, A. Härter, and J. H. Denschlag. Dynamics of a cold trapped ion in a bose-einstein condensate. *Physical Review Letters*, 105:133202, 2010.

[4] A. T. Grier, M. Cetina, F. Oručević, and V. Vuletić. Observation of cold collisions between trapped ions and trapped atoms. *Physical Review Letters*, 102:223201, 2009.

[5] F. H. J. Hall, M. Aymar, N. Bouloufa-Maafa, O. Dulieu, and S. Willitsch. Light-assisted ion-neutral reactive processes in the cold regime: Radiative molecule formation versus charge exchange. *Physical Review Letters*, 107:243202, 2011.

[6] W. G. Rellergert, S. T. Sullivan, S. Kotochigova, A. Petrov, K. Chen, S. J. Schowalter, and E. R. Hudson. Measurement of a large chemical reaction rate between ultra-cold closed-shell ^{40}Ca atoms and open-shell ^{174}Yb$^+$ ions held in a hybrid atom-ion trap. *Physical Review Letters*, 107:243201, 2011.

[7] S. Haze, S. Hata, M. Fujinaga, and T. Mukaiyama. Observation of elastic collisions between lithium atoms and calcium ions. *Phys. Rev. A*, 87:052715, May 2013.

[8] K. Ravi, S. Lee, A. Sharma, G. Werth, and S. A. Rangwala. Cooling and stabilization by collisions in a mixed ion-atom system. *Nature comminication*, 3:1126, 2012.

[9] S. T. Sullivan, W. G. Rellergert, S. Kotochigova, K. Chen, S. J. Schowaltera, and E. R. Hudson. Trapping molecular ions formed via photo-associative ionization of ultracold atoms. *Physical Chemistry Chemical Physics*, 13:18859, 2011.

[10] A. Härter, A. Krükow, A. Brunner, W. Schnitzler, S. Schmid, and J. H. Denschlag. Single ion as a three-body reaction center in an ultracold atomic gas. *Phys. Rev. Lett.*, 109:123201, Sep 2012.

[11] F. H. J. Hall and S. Willitsch. Millikelvin reactive collisions between sympathetically cooled molecular ions and laser-cooled atoms in an ion-atom hybrid trap. *Physical Review Letters*, 109:233202, 2012.

[12] J. Mur-Petit and J. J. Garcìa-Ripoll. Collective modes of a trapped ion-dipole system. *Appl. Phys. B*, 114:283–294, November 2013.

[13] H. Delmelt. Experiments with an isolated subatomic particle at rest. *Reviews of Modern Physics*, 62:522, 1990.

[14] W. Paul. Electromagnetic traps for charged and neutral particles. *Reviews of Modern Physics*, 62:531, 1990.

[15] K. Blaum. High-accuracy mass spectrometry with stored ions. *Physics Reports*, 425:1, 2006.

[16] R. E. March and J. J. F. Todd. *Quadrupole Ion Trap Mass Spectroscopy*. Wiley, New York, 2005.

[17] T. Rosenband, D. B. Hume, P. O. Schmidt, C. W. Chou, A. Brusch, L. Lorini, W. H. Oskay, R. E. Drullinger, T. M. Fortier, J. E. Stalnaker, S. A. Diddams, W. C. Swann, N. R. Newbury, W. M. Itano, and J. C. Bergquist. Frequency ratio of Al^+ and Hg^+ single-ion optical clocks; metrology at the 17th decimal place. *Science*, 319:1808, 2008.

[18] K. Blaum and F. Herfurth. *Trapped charged particles and fundamental interactions*. Lecture notes in Physics 749, Springer, Heidelberg, 2008.

[19] R. Blatt and D. Wineland. Review article entangled states of trapped atomic ions. *Nature*, 453:1008, 2008.

[20] F. G. Major, V. N. Gheorghe, and G. Werth. *Charged particle traps*. Springer-Verlag, Heidelberg, 2005.

[21] F. Diedrich, E. Peik, J. M. Chen, W. Quint, and H. Walter. Observation of a phase transition of stored laser-cooled ions. *Physical Review Letters*, 59:2931, 1987.

[22] D. J. Wineland, J. C. Bergquist, W. M. Itano, J. J. Bollinger, and C. H. Manney. Atomic-ion coulomb clusters in an ion trap. *Physical Review Letters*, 59:2935, 1987.

[23] K. Mølhave and M. Drewsen. Formation of translationally cold MgH^+ and MgD^+ molecules in an ion trap. *Physical Review A*, 62:011401, 2000.

[24] M. D. Barrett, J. Chiaverini, T. Schaetz, J. Britton, W. M. Itano, J. D. Jost, E. Knill, C. Langer, D. Leibfried, R. Ozeri, and D. J. Wineland. Deterministic quantum teleportation of atomic qubits. *Nature*, 429:737, 2004.

[25] G. Gabrielse and F. C. MacKintosh. Cylindrical penning traps with orthogonalized anharmonicity compensation. *International Journal of Mass Spectroscopy and Ion Processes*, 57:1, 1984.

[26] M. Drewsen and A. Brøner. Harmonic linear paul trap:stability diagram and effective potentials. *Physical Review A*, 62:045401, 2000.

[27] W. K. Hesinger, S. Olmschenk1, D. Stick, D. Hucul, M. Yeo, M. Acton, L. Deslauriers, C. Monroe, and J. Rabchuk. T-junction ion trap array for two-dimensional ion shuttling, storage, and manipulation. *Applied Physics Letters*, 88:034101, 2006.

[28] D. Kielpinski, C. Monroe, and D. J. Wineland. Architecture for a large-scale ion-trap quantum computer. *Nature*, 417:709, 2002.

[29] S. Seidelin, J. Chiaverini, R. Reichle, J. J. Bollinger, D. Leibfried, J. Britton, J. H. Wesenberg, R. B Blakestad, R. J. Epstein, D. B. Hume, W. M. Itano, J. D. Jost, C. Langer, R. Ozeri, N. Shiga, and D. J. Wineland. Microfabricated surface-electrode ion trap for scalable quantum information processing. *Physical Review Letters*, 96:253003, 2006.

[30] S. Stahl, F. Galve, J. Alonso, S. Djekic, W. Quint, T. Valenzuela, J. Verd, M. Vogel, and G. Werth. A planar penning trap. *European Physical Journal D*, 32:139, 2005.

[31] F. G. Major. Rseau trois dimensions de quadruples lectriques lmentaires pour le confinement d'ions. *Journal de Physique Lettres*, 38:221, 1977.

[32] Y. Onoda. *Master's thesis*. Kochi University of Technology, Japan, 2006.

[33] D. Hucul, M. Yeo, W. K. Hensinger, J. Rabchuk, S. Olmschenk, and Monroe C. On the transport of atomic ions in linear and multidimensinal ion trap arrays. *Quantum Information and Computation*, 8:0501, 2008.

[34] R. F. Wuerker, H. M. Goldenberg, and R. V. Langmuir. Electrodynamic containment of charged particles. *Journal of Applied Physics*, 30:342, 1959.

[35] K. Ravi, S. Lee, A. Sharma, G. Werth, and S. A. Rangwala. Three-dimensional lattice of ion traps. *Physical Review A*, 81:031401(R), 2010.

[36] D. A. Dahl. *Simion 3D Version 7.0 User Manual*. Bechtel BWXT, Idaho, 2000.

[37] A. Drakoudis, M. Söllener, and G. Werth. Instabilities of ion motion in a linear paul trap. *International Journal of Mass Spectrometry*, 252:61, 2006.

[38] J. I. Cirac and P. Zoller. Quantum computations with cold trapped ions. *Physical Review Letters*, 74:4091, 1995.

[39] W. Alt, M. Block, P. Seibert, and G. Werth. Spatial separation of atomic states in a laser-cooled ion crystal. *Physical Review A*, 58:R23, 1998.

[40] M. Block, A. Drakoudis, H Leuthner, P. Seibert, and G. Werth. Crystalline ion structures in a paul trap. *Journal of Physics B*, 33:L375, 2000.

[41] J. P. Schiffer, M. Drewsen, J. S. Hangst, and L. Hornekaer. Temperature, ordering, and equilibrium with time-dependent confining forces. *Processings of the National Academy of Sciences of the United States of America*, 97:10697, 2000.

[42] X.-L. Deng, D. Porras, and J. I. Cirac. Effective spin quantum phases in systems of trapped ions. *Physical Review A*, 72:063407, 2005.

[43] Krishnamurthy Ravi. *Trapping and Cooling of Ions and the Study of Ion Atom Interactions*. unpublished, 2012.

[44] H. J. Metcalf and P. van der Straten. *Laser Cooling and Trapping*. Springer-Verlag, New York, 1999.

[45] D. A. Steck. *Rubidium 85 D Line Data, Revision (2.1.5)*. unpublished, available online at http://steck.us/alkalidata, 2012.

[46] C. Monroe, W. Swann, and C. Wieman. Very cold trapped atoms in a vapor cell. *Physical Review Letters*, 65:1571, 1990.

[47] F. Fuso, D. Ciampini, E. Arimondo, and C. Gabbanini. Ion processes in the photoionization of laser cooled alkali atoms. *Optics Comminication*, 173:223, 2000.

[48] A. M. Steane, M. Chowdhury, and C. J. Foot. Radiation force in the magneto-optical trap. *Journal of the Optical Society of America b*, 9:2142, 1992.

[49] C. G. Townsend, N. H. Edwards, C. J. Cooper, K. P. Zetie, C. J. Foot, A. M. Steane, P. Szriftgiser, H. Perrin, and J. Dalibard. Phase-space density in the magneto-optical trap. *Physical Review A*, 52:1423, 1995.

[50] M. Weidemüller and C. Zimmermann. *Cold Atoms to Molecules*. WILEY-VCE, Weinheim, 2009.

[51] P. Kohns, P. Bush, W. Süptitz, C. Csambal, and W. Ertmer. On-line measurement of sub-doppler temperature in a rb magneto-optical trap-by-trap centre oscillations. *EUROPHYSICS LETTERS*, 22, 1993.

[52] K. Ravi, S. Lee, A. Sharma, G. Werth, and S. A. Rangwala. Combined ion and atom trap for low temperature ion-atom physics. *Appl. Phys. B: Lasers and Optics*, 107:971, 2011.

[53] J. M. Brown and A. Carrington. *Rotational Spectroscopy of Diatomic Molecules*. University of Cambridge press, Cambridge, first edition, 2003.

[54] J. M. Hollas. *Modern Spectroscopy*. John Wiley and Sons, Ltd, New York, forth edition, 1987.

[55] Reginaldo Napolitano, John Weiner, Carl J. Williams, and Paul S. Julienne. Line shapes of high resolution photoassociation spectra of optically cooled atoms. *Phys. Rev. Lett.*, 73:1352–1355, 1994.

[56] C. Drag, B. L. Tolra, O. Dulieu, C. Daniel, M. Vatasescu, S. Boussen, S. Guibal, A. Crubellier, and P. Pillet. Experimental versus theoretical rates for photoassociation and for formation of ultracold molecules. *IEEE JOURNAL OF QUANTUM ELECTRONICS*, 36:1378, 2000.

[57] S. Lee, K. Ravi, and S. A. Rangwala. Measurement of collisions between rubidium atoms and optically dark rubidium ions in trapped mixtures. *Phys. Rev. A*, 87:052701, May 2013.

[58] D. A. Church. Collision measurements and excited-level lifetime measurements on ions stored in paul, penning and kingdon ion traps. *PHYSICS REPORS*, 228, 1993.

[59] G. W. F. Drake. *Handbook of Atomic, Molecular and Optical Physics*. Springer, New York, 2005.

[60] J. E. Sansonetti and W. C. Martin. *Handbook of Basic Atomic Spectroscopic data*. American Institute of Physics, New York, 2005.

[61] C. Gabbanini, S. Gozzini, and A. Luchesini. Photoionization cross section measurement in a rb vapor cell trap. *Optics Comminications*, 141:25, 1997.

[62] R. Côté and A. Dalgarno. Ultracold atom-ion collisions. *Physical Review A*, 62:012709, 2000.

[63] S. A. Maiorov, O. F. Petrov, and V. E. Fortov. *Calculation of resonant charge exchange cross sections of ions of rubidium, cesium, mercury and noble gases, 34th EPS conf. on Plasma Phys.* European Physical Society, Mulhouse, 2007.

[64] L. D. Landau and E. M. Lifshitz. *Quantum Mechanics*. Pergamon Press, Oxford, second edition, 1965.

[65] N. F. Mott and H. S. W. Massey. *The theory of atomic collisions*. Oxford University Press, Oxford, third edition, 1965.

[66] L. D. Landau and E. M. Lifshitz. *Mechanics*. Elsevier, Oxford, third edition, 1976.